Stability Analysis of Slender Plates Stiffened with Topologically Optimized WAAM Stiffeners: Experimental and Numerical Investigation

Stan Landers

Delft University of Technology

TU Delft

Stability Analysis of Slender Plates Stiffened with Topologically Optimized WAAM Stiffeners: Experimental and Numerical Investigation

by

Stan Landers

to obtain the degree of Master of Science
at the Delft University of Technology.

Student number:	4910222	
Project duration:	February 10, 2025 – September 24, 2025	
Thesis committee:	Prof. Dr. M. Veljkovic,	TU Delft, Chair
	Dr. T. Tankova,	TU Delft, supervisor
	Dr. J. Wu,	TU Delft

Cover: WAAM machine from Valk Welding B.V.

TU Delft

Preface

This thesis is the final step in completing my Master's degree in Civil Engineering at Delft University of Technology, in the Structural Engineering track. I chose to focus on wire arc additive manufacturing because it is an exciting and relatively new field in the industry. It gave me the chance to dive into my own experiments, such as manufacturing test specimens with additive manufacturing equipment and running different lab setups. On top of that, I was able to further develop my interest in finite element modeling, which has been one of the most rewarding parts of this project.

I would like to thank my supervisor, Trayana Tankova, for her guidance, feedback, and encouragement throughout the entire process. I'm also very grateful to the other members of my thesis committee, Milan Veljkovic and Jun Wu, for their valuable input and for pushing me to get the most out of this work.

A big thank you also goes to Valk Welding B.V., where I manufactured the wire arc additive stiffeners. The staff and engineers there were incredibly helpful, sharing their expertise and supporting me during the process. This research wouldn't have been possible without them.

I also want to thank the laboratory staff at TU Delft for their help in setting up and running the experiments. Their support with the equipment and test execution was essential for the success of this work. A special thanks to Derek van Bochove, my lab mentor, who guided me through every experiment and was always there to help.

Finally, I'm grateful to my friends and family for their support throughout this thesis. Their encouragement made a big difference in getting me through the challenges and completing this journey.

Stan Landers
Delft, September 2025

Summary

This thesis explores how slender plates can be reinforced with stiffeners to improve their stability, and how new manufacturing methods can lead to more efficient designs. Traditional stiffeners are often simple in geometry, which limits their structural efficiency. With Wire Arc Additive Manufacturing (WAAM), however, it becomes possible to produce complex shapes that may perform better. The research combines experiments, numerical simulations, and optimization studies. Plates with WAAM stiffeners were manufactured and tested alongside plates with conventional rectangular stiffeners. Numerical models were developed and validated against the experimental results, including the influence of imperfections and residual stresses. Different initial stiffener shape models were then used in a topology optimization process to design further improved stiffener geometries. The results indicate that the numerical models of the WAAM stiffeners can replicate the experimental performance, considering the restricted number of specimens utilized in the tests. However, the models of the plates employing prismatic rectangular stiffeners demonstrated reduced compliance with the experimental results. New initial stiffener geometries underwent topological optimization and showed performance comparable to that of conventional prismatic stiffeners of equivalent volume, thus lacking any advantages. The study highlights both the opportunities and challenges of using WAAM in structural applications and provides recommendations for future research.

Contents

Nomenclature

Abbreviations

AM	Additive Manufacturing
BC	Boundary Condition
DED	Directed Energy Deposition
DIC	Digital Image Correlation
FEA	Finite Element Analysis
FEM	Finite Element Method
GMAW	Gas Metal Arc Welding
GMNIA	Geometrically and Materially Nonlinear Analysis with Imperfections
GTAW	Gas Tungsten Arc Welding
LBA	Linear Buckling Analysis
LPF	Load Proportionality Factor
MIMP	Modified Interpolation of Material Properties
MMA	Method of Moving Asymptotes
OC	Optimality Criteria
PAW	Plasma Arc Welding
RAMP	Rational Approximation of Material Properties
RHS	Rectangular Hollow Section
SIMP	Solid Isotropic Material with Penalization
TO	Topology Optimization
WAAM	Wire Arc Additive Manufacturing

Greek symbols

$\bar{\lambda}_p$	Relative slenderness of the plate	[$-$]
$\beta_{A,c}$	Reduction factor for buckling resistance	[$-$]
κ	Curvature	[mm^{-1}]
ν	Poisson's ratio	[$-$]
ρ_e	Relative density	[$-$]
σ_E	Intermediate elastic buckling stress	[N/mm^2]
σ_{cr}	Critical buckling stress of the plate	[N/mm^2]

Roman symbols

E	Young's modulus	[GPa]
E_s	Stiffener efficiency	[$-$]
F	Force	[kN]
I	Amperage (welding current)	[A]
I_{sl}	Second moment of area of stiffened plate	[mm^4]
R	Electrical resistance	[Ohm]
R_r	Buckling resistance ratio	[$-$]
R_b	Buckling resistance	[kN]
S	Welding speed	[m/min]
U	Voltage	[V]
V	Volume	[mm^3]
W	Weight	[kg]
W_r	Weight ratio	[$-$]
f_u	Ultimate tensile strength	[N/mm^2]
f_y	Yield strength	[N/mm^2]
k_σ	Buckling factor	[$-$]
p	Penalty factor	[$-$]

1 Introduction

1.1. Research context and problem

In construction, slender steel plates are frequently used. These plates are susceptible to buckling due to their slenderness. Stiffeners can be incorporated into the thin plates to increase buckling resistance and enhance their stability. Nonetheless, substantial additional material is required to reinforce the thin plates during the standard manufacture of these stiffeners using traditional topologies. Common topologies include prismatic rectangular shapes, for example. This increased production and utilization of more steel materials results in numerous new negative emissions into the environment. Emissions can be reduced by improving the topology of the stiffeners, hence necessitating less steel. Efforts have been undertaken to optimize the topology of stiffeners for steel plates [1]. Nonetheless, fabricating such complex topologies using traditional methods, like cold forming or hot rolling, proves to be difficult. Consequently, those stiffeners can be fabricated using Wire Arc Additive Manufacturing (WAAM). Additive manufacturing requires consideration of numerous other factors. Similar to traditional welding, issues such as heat accumulation and residual stress play a role; however, WAAM provides a greater degree of control over the deposition process and the resulting stiffener geometry. Consequently, to ensure safety, these additively made stiffeners must undergo both appropriate experimental and numerical testing.

1.2. Research objectives

This research project aims to examine the stability performance of slender plates reinforced with stiffeners fabricated by WAAM. The validation of the numerical model is conducted by experimental testing. This essentially covers the comparison of local and global buckling modes of the plate, critical stresses, and plate weights. Upon validation, Finite Element Models (FEM) can be developed to accurately predict the stability behavior of stiffeners with various complex topologies.

This research additionally aims to further examine the optimization of the topology of the stiffener produced by WAAM. The prior efforts in stiffener optimization will be utilized for the experimental and numerical analysis. Figure 1.1 shows that optimized topology. The stiffener topology is shown schematically with sharp corners for clarity; in practice, WAAM deposition naturally results in rounded corners rather than perfectly sharp edges. Nonetheless, additional optimization may be performed to enhance material reduction in stiffeners even more.

Figure 1.1: Topologically optimized stiffener geometry from prior research

1.3. Research questions

The purpose of this research study is shaped by the following primary research question:

- How does the use of topologically optimized WAAM-manufactured stiffeners influence the stability performance of slender plates, and how can their geometry be further optimized for improved performance?

To address the primary research question, several sub-questions have been formulated to simplify and divide the main investigation:

- How do slender plates reinforced with WAAM stiffeners behave under experimental loading conditions in terms of stability?
- How accurately can numerical models predict the stability and buckling performance of WAAM-stiffened slender plates?
- What is the impact of different geometries or topologies of stiffeners on the stability performance of slender plates?

1.4. Scope and limitations

Slender plates can be strengthened for structural applications in a variety of ways. Plates strengthened with a specific topologically optimized stiffener made by WAAM will be the specific focus of this study. Experimental testing to evaluate stability and buckling resistance is used in the research, as well as numerical modeling. The latter will be extensively used to simulate the behavior of the plates under uniaxial loading conditions, validate the experimental findings, and explore the influence of different parameters such as material properties, boundary conditions, and stiffener placement. Data analysis techniques will be utilized to compare experimental and numerical results and gain deeper insights into the structural behavior. Moreover, the focus lies on further investigation of different geometries that can improve the structural behavior even more.

While this study provides insights into the structural behavior of WAAM-produced topologically optimized stiffened plates, several limitations must be recognized. Experimental testing is limited to uniaxial loading conditions and only two WAAM-stiffened plate specimens, excluding other loading scenarios such as biaxial or shear loading. Numerical modeling relies on idealized assumptions regarding boundary conditions, material properties, and geometry, which may introduce deviations from real-world behavior. Furthermore, geometrical and material imperfections were included in the models. Due to time constraints, only one single stiffener geometry is experimentally investigated, restricting the scope of parametric investigation. Finally, the findings are specific to the tested configurations and conditions, and their applicability to other structural scenarios should be considered with caution.

1.5. Report structure

This thesis is structured into five main chapters, followed by references and appendices, to systematically present the research on WAAM-produced topologically optimized stiffened plates. Chapter 2 contains the literature review, which examines the stability challenges of slender plates, discusses WAAM technology and topology optimization, and identifies research gaps addressed in this study. The methodology in Chapter 3 details the experimental setup, numerical simulations, optimization techniques, and data analysis methods used to investigate the structural performance of stiffened plates. The results in Chapter 4 present findings from experimental tests, numerical validation, and the performance of optimized stiffeners. Chapter 5 discusses the conclusions and recommendations. It summarizes the key conclusions, offers practical suggestions for WAAM applications, and outlines potential directions for future research. The discussion in Chapter 6 interprets the key findings, explores their implications for structural design, and acknowledges the study's limitations. The thesis concludes with references and appendices containing supplementary information such as experimental data and numerical modeling details.

2 Theory

2.1. Slender plates and stability

2.1.1. Structural behavior of slender plates

Steel plates can be categorized into slender, moderate, and stocky classifications based on their slenderness parameter, along with its buckling and yielding properties. This research will exclusively focus on slender plates. Slender plates are structural components characterized by one dimension (thickness) that is considerably smaller than the other two dimensions (length and width). The slenderness ratio, usually defined as the ratio of length or width to thickness, distinguishes these plates. Slender plates undergo elastic buckling, followed by yielding in the post-buckling phase. These plate types display low buckling capacity but feature significant post-buckling reserve [2], indicating their capability to carry additional loads effectively after buckling occurs. This phenomenon assists in preventing abrupt plate failure and ensuring safety. Slender steel plates are extensively used worldwide. In civil engineering, they are utilized in girders for bridge construction. However, they are also utilized for constructing building facades, for example. Steel slender plates can be used not only in civil or structural engineering but also in mechanical and marine engineering applications. Consider aerospace components or ship hulls, for instance [3].

2.1.2. Buckling and stability considerations

Stability is a critical aspect of structural engineering, referring to a structure's ability to maintain equilibrium and resist deformation or collapse under applied loads. A stable structure can withstand loads without experiencing excessive displacements or abrupt failure. Stability analysis ensures that structures perform safely and reliably during their intended service life. Consequently, it is imperative to show greater caution about the buckling of these slender plates, as they are particularly susceptible to it. Buckling is a failure mode where a structure suddenly deforms under compressive or shear stress. Consequences of buckling could be the loss of load-carrying capacity, which could result in losing the ability to support additional loads, even if the material has not reached its yield strength (slender plates). If a slender plate is designed with specific dimensions, its buckling capacity may be inadequate. In such instances, stiffeners may be added to enhance buckling capacity.

An important consideration in predicting the buckling behavior of plates is the correct implementation of the analysis procedure in FEM software. To obtain accurate results, a GMNIA (geometrically and materially nonlinear analysis with imperfections) should be performed, in which both plasticity and buckling failure modes are accounted for in the FE model [4]. In this approach, the buckling resistance is determined from the load–displacement response of the plate, which represents the applied load versus the corresponding displacement. According to EN 1993-1-5 [4], the buckling resistance is defined as the lower value obtained from two criteria: (1) the maximum load on the load–displacement curve (limit load), or (2) the load corresponding to the largest tolerable plastic strain of 5%. In the present study, the second criterion was never reached for any case, meaning that the buckling resistance always corresponded to the maximum load observed in the load–displacement curve.

2.1.3. Role of stiffeners in stability

Stiffeners are structural elements that can take many shapes, such as ribs, beams, or frames, added to thin plates to improve their stability. They work by increasing the plate's overall stiffness, increasing its elastic critical plate buckling stress, and delaying the beginning of buckling under compressive or shear loads. Equation 2.1 shows the general formula to calculate the critical stress for both stiffened and unstiffened plates [5].

$$\sigma_{cr} = k_\sigma \, \sigma_E \tag{2.1}$$

It includes two terms, with σ_E representing an intermediate elastic buckling stress which maintains the same value for both stiffened and unstiffened plates. The remaining term k_σ denotes the buckling factor, which indicates the difference in critical stresses between a stiffened and an unstiffened slender plate. In calculating k_σ for the stiffened plate, the second moment of area of the whole stiffened plate (I_{sl}) is considered, opposed to an unstiffened plate where I_{sl} is not taken into the equation. This consequently increases the buckling factor and therefore also the elastic critical plate buckling stress of the stiffened plate, hence reducing the relative slenderness. Equation 2.2 illustrates this inverse relationship between relative slenderness and critical stress.

$$\bar{\lambda}_p = \sqrt{\frac{\beta_{A,c} \, f_y}{\sigma_{cr}}} \tag{2.2}$$

To facilitate a fair comparison between stiffened and unstiffened slender plates, the critical buckling stress ratio is employed. The ratio is determined by dividing the critical stress of a stiffened plate by the critical stress of an unstiffened plate. A critical stress value of 4 indicates that a stiffened plate can potentially experience a fourfold increase in the critical load prior to buckling. This information is relevant for comparing the effects of incorporating stiffeners into a slender plate.

The behavior of stiffened panels includes their structural and mechanical responses to different stress circumstances and environmental influences. Essential elements involve their stability and buckling performance, where stiffeners enhance the buckling load and affect buckling modes. Under in-plane compression loads, the reinforced plate may experience buckling in two modes: local and global. A buckling mode occurs between stiffeners for local buckling. Global buckling, in contrast, refers to the buckling behavior of the entire stiffened plate. Research has extensively examined both buckling cases. It is established that global buckling of stiffened plates correlates with low stiffener rigidity, while local buckling is linked to higher stiffener rigidity. Figure 2.1a illustrates the global buckling behavior of a stiffened plate. In this case, the entire panel deflects in a single, large-scale mode. When the stiffener thickness is increased, and thus its rigidity increased, the buckling response shifts. As shown in Figure 2.1b, the panel then exhibits local buckling, where deformation is concentrated in smaller regions rather than involving the whole plate.

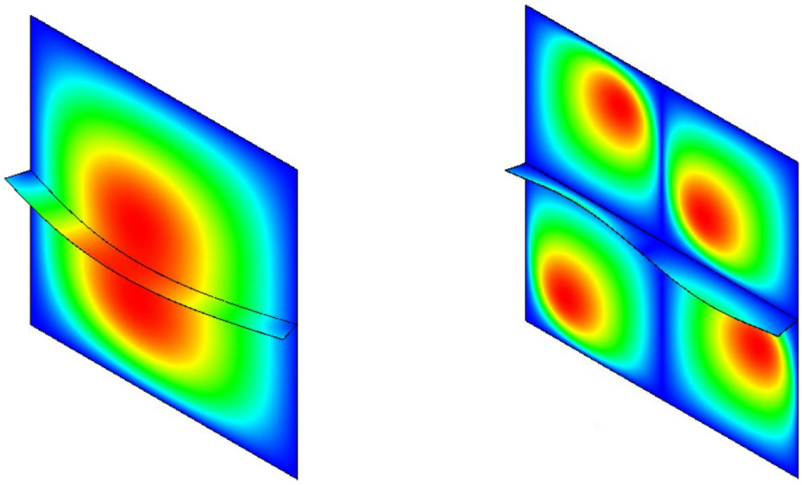

(a) Global buckling of stiffened plate

(b) Local buckling of stiffened plate

Load-carrying capacity is another crucial factor, as stiffeners improve the panel's ability to resist compressive and shear forces before failure. Additionally, the deformation and deflection behavior of stiffened plates is significantly affected by the geometry and material properties of the stiffeners, helping to minimize displacement and improve stiffness.

2.1.4. Methods for stability analysis

Stability analyses of stiffened slender plates can be done in a number of ways. A more practical real world approach is with the help of experimental techniques. Plates are subjected to forces such as axial compression or shear. These forces are measured to investigate the effect it has on the deformations and strains that occur in the plates during the test. In order to measure these strains and deformations, monitoring tools such as Digital Image Correlation (DIC) or Strain Gauges can be used. DIC is a technique that involves comparing digital images of a test object (specifically, a stiffened slender plate) at various stages. It is an innovative non-contact optical method that monitors pixel groups. The system can then quantify surface displacements and generate comprehensive fields of 2D and 3D deformation vectors and strain maps [6]. An alternative way for analyzing stability involves the utilization of strain gauges. The sensors are attached with an appropriate adhesive to measure the strain in the test object. As the test object undergoes deformation, the foil within the strain gauge sensor at the same time deforms. This results in a shift of its electrical resistance, which can then be monitored and transmitted to a computer [7]. The stresses and displacements obtained through these experimental methods can be utilized to assess the stability characteristics of the plate under various loading conditions. Figure 2.2 shows two schematics of both analysis methods. The first schematic (a) shows a 2D representation of a set-up for a DIC system. The second schematic (b) shows a visual representation of a strain gauge, including the measured strain directions.

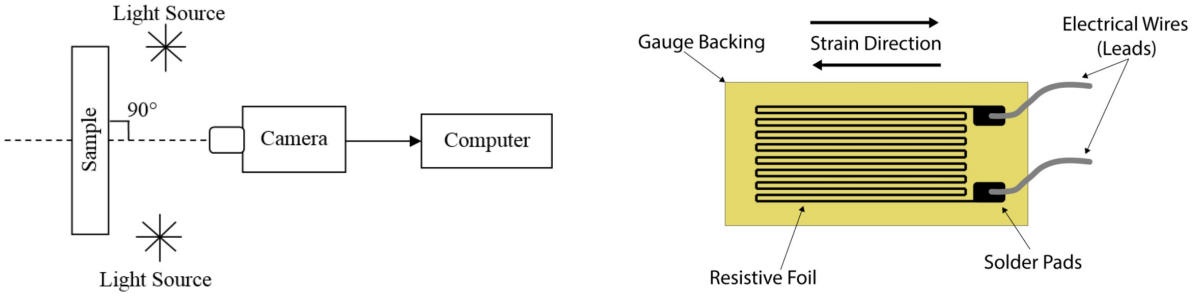

(a) Schematic of 2D DIC set-up [8]

(b) Schematic of strain gauge [9]

Figure 2.2: A schematic diagram of both stability analysis methods

A more accessible approach to assessing stability behavior is through the utilization of numerical approaches. Finite Element Analysis (FEA) software can precisely estimate strains, deformations, and buckling modes, for example. Numerical tools commonly used for such applications include software such as Abaqus or Ansys. This FEA software supports the modeling of complex geometries, including stiffeners with various shapes and topologies. This is very difficult to accomplish by analytical solutions, for instance. These mathematical methods frequently depend on idealized assumptions (e.g., perfect geometry, uniform material properties, linear elasticity) that may not apply to real-world scenarios. Although they are beneficial for fundamental and theoretical applications, their usefulness is limited.

2.2. Wire arc additive manufacturing technology

2.2.1. Principles of wire arc additive manufacturing

Wire Arc Additive Manufacturing (WAAM) is an advanced additive manufacturing technology that employs an electric arc as a heat source and wire feedstock to construct metal components layer by layer. This method is effective for large-scale part production, providing high deposition rates and cost efficiency relative to powder-based techniques, for instance. WAAM demonstrates compatibility with several metals, such as steel, aluminium, titanium, and copper, thereby enhancing its adaptability for

applications in aerospace, construction, and energy sectors [10]. WAAM utilizes extensive welding research to support its knowledge of material behaviors; however, it must address challenges such as heat accumulation, residual stresses, and anisotropic properties.

WAAM is a form of Directed Energy Deposition (DED), a broader category of additive manufacturing processes. DED works by applying a heat source to melt material, which is then deposited onto a surface and solidifies, bonding with the existing structure to form a three-dimensional object. In DED, material can be supplied in the form of either powder or wire. Although powder-based systems are typically more precise, wire-based systems offer better material efficiency, which is particularly advantageous for large-scale manufacturing [11]. In WAAM, the deposition of material occurs layer by layer, using a wire feedstock in combination with an arc welding process. The main techniques used in WAAM include:

- Gas Metal Arc Welding (GMAW),
- Gas Tungsten Arc Welding (GTAW)
- Plasma Arc Welding (PAW)

Each of these methods has distinct characteristics. GMAW uses a welding wire as the melting electrode, creating an arc between the wire and the workpiece, which allows material to be deposited. On the other hand, both GTAW and PAW utilize a tungsten electrode for the welding process. PAW differs from GTAW in that it produces a narrower, higher-temperature arc. This enables PAW to deliver up to three times the arc energy of GTAW, resulting in faster welding speeds and reduced welding distortion [12]. Figure 2.3 shows a schematic diagram of the GMAW, GTAW and PAW methods respectively.

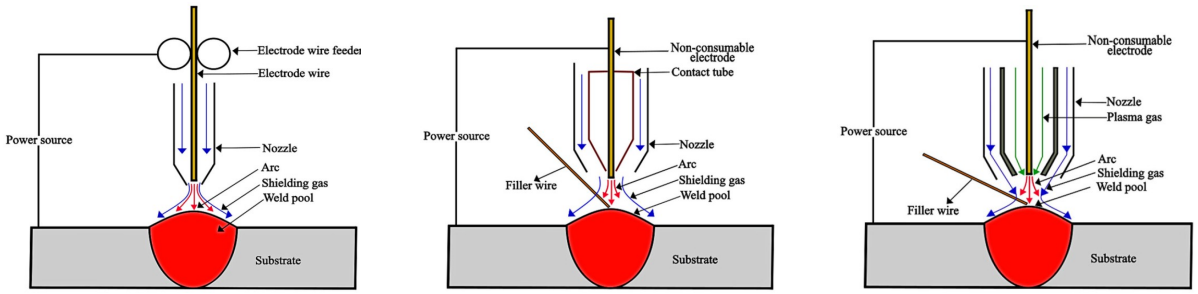

(a) GMAW **(b)** GTAW **(c)** PAW

Figure 2.3: Schematic diagrams of the different WAAM technologies [13]

A WAAM machine consists of several key components that ensure its proper functioning. The power source is fundamental, as it provides the necessary energy for the welding process. Next, the wire feed system continuously supplies the feedstock material. In GMAW, the wire feed acts as the consumable electrode, whereas in GTAW and PAW, a non-consumable tungsten electrode generates the heat, while the filler wire is supplied separately. The robotic system is responsible for controlling the movement and precise deposition of the weld material. Another crucial component is the shielding gas, which protects the molten material from contamination, ensuring weld integrity and preventing oxidation [13]. To regulate the system's temperature and prevent overheating, a cooling system is implemented. This can be as simple as water-cooling mechanisms where cool water circulates through tubes, dissipating excess heat.

Several key parameters must be defined in advance to ensure precise and reliable welding results. One critical factor is the welding speed (S). If the speed is too high, the deposited layers receive insufficient heat, resulting in thinner welds. Additionally, excessive welding speed can cause uneven heat distribution, leading to localized residual stresses that may weaken the structure. Another important parameter is the amperage, which represents the welding current. Amperage directly influences the amount of heat generated in the electrode (welding wire or tungsten). Higher amperage increases heat input, resulting in deeper penetration and a higher deposition rate. Closely related to amperage is voltage. The arc itself is an electric discharge that forms between the electrode and the workpiece.

Higher voltage increases the arc length, which in turn spreads the heat over a wider area, producing a broader but shallower weld [14]. The relationship between amperage and voltage is described by Ohm's Law, as shown in Equation 2.3.

$$U = I \cdot R \tag{2.3}$$

Here, U represents the voltage, I the current, and R the resistance. Since the resistance remains constant over time, an increase in amperage leads to a decrease in voltage, and vice versa. Therefore, an optimal balance must be established when selecting these parameters to ensure stable welding conditions. Once the appropriate amperage and voltage are determined, the power input for the process can be calculated by multiplying the welding current by the voltage.

Several additional parameters also play a significant role in the welding process, such as crater times and weaving patterns. Firstly, during layer deposition, the end of the layer tends to accumulate more heat, which can cause it to sink in, leading to a sloped appearance. To counteract this, craters can be added at the start and/or end of the deposited layer. This involves depositing additional welding material at these locations for a specified duration to compensate for the height difference, ensuring a more even layer. Secondly, a weave pattern can be introduced to enhance the weld's width and quality. A weave involves moving the torch or electrode in a side-to-side motion, rather than a straight line. This not only increases the weld width but also helps to distribute the heat more evenly, preventing concentrated heating in specific areas. Weaving patterns can vary, including motions perpendicular to the welding direction or even spiral patterns for more complex applications. Figure 2.4 illustrates a weaving pattern, where the motion is perpendicular to the welding direction, as indicated by the thick dashed line. The welding direction is shown by the large white arrow, which points to the right in this case. From this viewpoint, the welding tip moves up and down in a repetitive motion while the torch moves horizontally to the right.

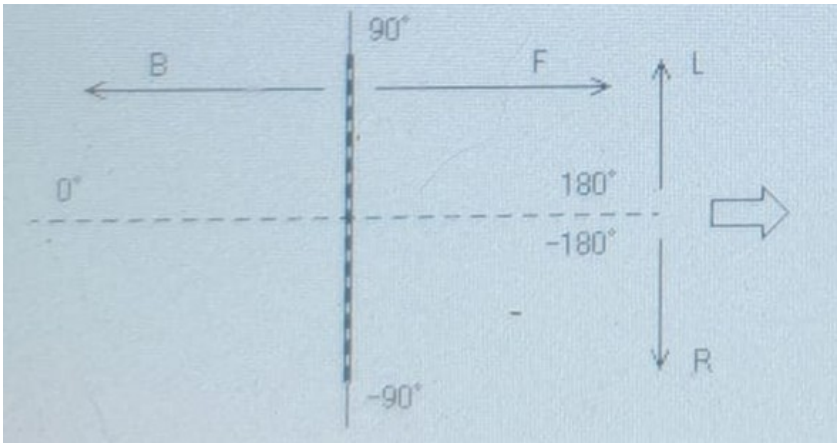

Figure 2.4: Side-to-side weaving pattern, perpendicular to the welding direction

WAAM presents numerous advantages that render it an attractive technique for the manufacturing of metal components. It offers increased deposition speeds and scalability, facilitating the effective fabrication of large components, a task that is difficult for powderbased techniques. WAAM reduces material waste by near-net-shape manufacturing, making it especially economical for costly metals such as titanium. Furthermore, it offers considerable flexibility in material application, allowing multi-material designs and the repair or improvement of existing components. WAAM takes advantage on proven welding methods, providing a solid basis for understanding material characteristics and ensuring reliability. These benefits establish WAAM as a realistic and resource-efficient option for sectors like aerospace, construction, and energy [10].

2.2.2. Structural performance and material properties

Several studies have already been conducted to assess the application of using WAAM produced stiffeners as structural reinforcement. For instance, in a recent experimental study [15], they specifically looked at the reinforcement of I-section steel columns and their potential. The WAAM stiffeners enhanced structural performance through three mechanisms: increasing area and the second moment of area, enhancing local buckling resistance, and improving residual stress patterns. The research also mentioned the contribution to material savings and reduced CO2-equivalent emissions compared to traditional strengthening methods. Some of the limitations it showed were that WAAMinduced thermal effects introduced larger geometric imperfections, which can affect buckling resistance. On top of that, the WAAM steel showed variability in mechanical properties, such as yield and tensile strengths, which emphasizes the need for material standardization.

The material properties of WAAM produced products can differ due to several factors. The first one being the surface roughness after printing. Usually after printing the WAAM parts have a rougher surface due to the layer-by-layer deposition. This can cause visible ridges and irregularities, which can then have influence on the mechanical properties of the product. For that reason, milling the WAAM parts can enhance the part's overall strength as it smoothens out the surface, therefore reducing the occurrence of these irregularities as can be observed in Table 2.1 & 2.2. Another reason for material property deviations can come from residual stresses. The rapid heating and cooling during the WAAM process causes the existence of significant residual stresses in the material. These stresses can cause distortion, defects, or cracking and affect the part's mechanical properties, especially in the as-printed stage [16]. Anisotropy is another reason for varying material properties. Because of how the material is deposited, certain grain directions occur, making it anisotropic. For this reason, properties such as yield strength and ultimate tensile strength can vary depending on the orientation relative to the deposition layers. An experimental and numerical study was conducted that looked into the material properties of WAAM products using ER70s filler wire [17]. For this research, material properties were found for three different cutting orientations of WAAM specimen. The outcome of this experiment showed that the results are dependent on the geometrical irregularities rather than on the direction of cutting. Tables 2.1 & 2.2 display these material properties for both the milled stage as the as-printed stage, including the cutting direction.

Table 2.1: Milled WAAM product material properties using ER70s filler wire

Milled	**Perpendicular (90°)**	**Longitudinal (0°)**	**Intermediate (45°)**
E [GPa]	201	214	193
f_y [MPa]	437	419	435
f_u [MPa]	584	569	574
v [-]	0.28	0.28	0.27

Table 2.2: As-printed WAAM product material properties using ER70s filler wire

As-printed	**Perpendicular (90°)**	**Longitudinal (0°)**	**Intermediate (45°)**
E [GPa]	195	205	198
f_y [MPa]	400	434	427
f_u [MPa]	544	553	544
v [-]	0.28	0.25	0.35

In the WAAM process, considerable deformation can occur in the base plate due to the strong temperature gradients and the repeated heating and cooling in additive manufacturing. A slender plate as the base has poor stiffness, making it more vulnerable to heat expansion and contraction, which results in warping. As the hot material is layered, concentrated heat input causes the metal to expand, followed

by fast cooling that produces shrinkage. The repetitive temperature cycling generates residual stresses that increase, leading to deformation. Moreover, the irregular heat distribution causes different sections of the plate to experience different degrees of expansion and contraction, increasing the bending effect. Consequently, significant imperfeections and eccentricities can appear in the structure, deviating from the initial design. These flaws can substantially impact the mechanical performance of the stiffened plate, thereby lowering its buckling resistance and overall stability. Understanding and reducing these deformations is essential for maintaining the structural integrity of WAAM-manufactured components, especially in applications requiring exact geometric precision.

2.3. Topology optimization

2.3.1. Principles of topology optimization

Topology optimization (TO) is a computational design technique used to determine the optimal material distribution within a given design space to achieve specific performance objectives, such as minimizing weight, maximizing stiffness, or optimizing energy efficiency, subject to constraints like stress limits, manufacturing methods, or functional requirements. The process typically uses FEA to evaluate performance. Some of its biggest advantages are:

- It optimizes material usage by removing unnecessary regions, reducing weight and material costs while maintaining structural integrity;
- it generates designs well-suited for AM techniques like WAAM, where complex geometries can be manufactured without the limitations;
- and it reduces material waste, and aligns with sustainable practices.

Numerical simulations [1] revealed that stiffeners, which have been topologically optimized, can achieve similar or improved critical buckling loads and resistance compared to traditional prismatic stiffeners, with up to 30% material savings. Tapered designs, thickness variations, and optimized openings proved particularly effective in balancing weight reduction with structural performance, showcasing the potential of WAAM to create efficient, tailored solutions for structural applications.

2.3.2. Methods and algorithms for topology optimization

Topology optimization methods combine mathematical models and numerical algorithms to determine the most efficient material distribution within a design space [18]. These methods typically aim to balance objectives such as stiffness or weight with constraints on material usage or manufacturability. By using different interpolation and optimization strategies, topology optimization enables the development of practical structural designs that maintain performance while reducing material usage.

In this thesis, topology optimization is performed using *Tosca Structure* in combination with Abaqus. Tosca Structure provides three material density interpolation schemes: SIMP, RAMP, and MIMP. Before introducing these methods in detail, it is important to define the concept of material interpolation. In topology optimization, the problem is formulated as a material density distribution problem, where each finite element of the geometry is assigned a relative material density ranging from 0 (void) to 1 (solid). The interpolation method then defines how material properties, such as stiffness, are calculated for intermediate density values between 0 and 1. In this way, material can be strategically removed from low-stress regions, resulting in optimized topologies that are structurally efficient.

Material interpolation methods

The first interpolation method is the Solid Isotropic Material with Penalization (SIMP) approach, which is one of the most widely used techniques in topology optimization. In SIMP, the material properties are interpolated as a function of the element density, and a penalization factor is applied to reduce intermediate density values [19]. Equation 2.4 illustrates the relation between the relative density (ρ_e) and the Young's modulus (E), where the penalty factor controls the interpolation curve. Figure 2.5 shows this visually: with a penalty factor of $p = 1$, intermediate densities occur frequently, while with $p = 3$, the interpolation forces material densities to approach either 0 or 1. This behavior is advantageous from a manufacturability perspective, as it avoids designs with highly varying thicknesses and instead promotes geometries with clearer material/void separation.

$$E = E_0 \cdot \rho^p \tag{2.4}$$

The second interpolation method is the Rational Approximation of Material Properties (RAMP). Like SIMP, the RAMP method applies a penalization factor to reduce the occurrence of intermediate density values. However, it employs a different mathematical relationship between the Young's modulus and the relative density, which has been shown to be particularly effective in dynamic optimization problems [20]. Equation 2.5 defines this interpolation, and its effect is shown in Figure 2.5. The black curve illustrates the case with $p = 1$ again, while the red curve shows the RAMP interpolation with $p = 4$. As with SIMP, the RAMP formulation prefers densities toward 0 or 1, resulting in clearer topologies that are more practical for structural applications.

$$E = E_0 \cdot \frac{\rho}{1 + p(1 - \rho)} \tag{2.5}$$

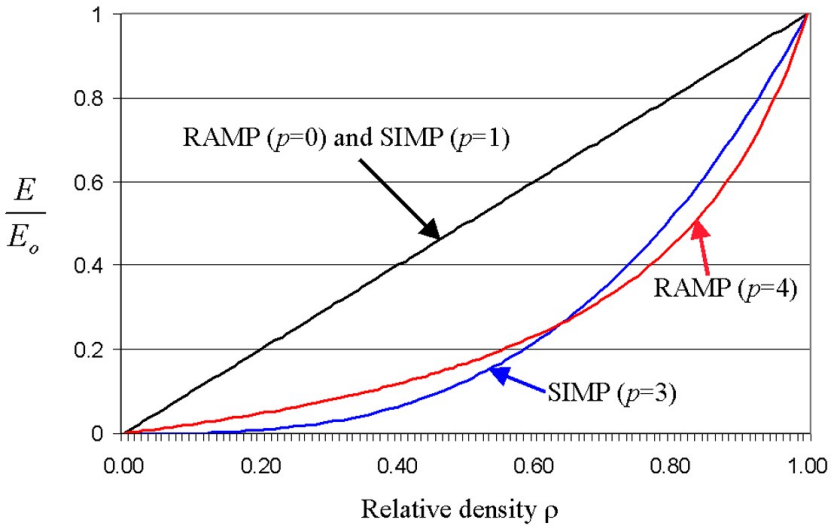

Figure 2.5: Relation between Young's Modulus and relative material density for both the SIMP and RAMP material interpolation methods [20]

The third interpolation scheme available in Tosca Structure is the Modified Interpolation of Material Properties (MIMP). This method can be understood as a hybrid between SIMP and a new density interpolation approach: it takes the SIMP formulation for stiffness interpolation, while applying a different interpolation rule for the physical density. MIMP is particularly recommended for optimization problems where stresses are used directly in the objective or as constraints, as well as in cases where mass-dependent effects, such as acceleration forces, are present [20].

Objectives and constraints

Before initiating the optimization process, it is essential to clearly define the objectives and constraints that govern the problem. The objective represents the goal of the optimization and defines the criterion that the algorithm attempts to minimize or maximize. Typical objectives in structural optimization include minimizing displacements or structural mass, or maximizing eigenfrequencies to improve dynamic performance. Constraints, in contrast, define the boundaries within which the optimization must operate. These are conditions that the optimized design must satisfy in order to remain feasible and practical. Examples include volume constraints, where the material usage is restricted to a certain percentage (e.g., 30% of the design volume), or displacement constraints, which ensure that specific nodes or key points do not exceed prescribed limits. Together, the objectives and constraints form the foundation of the optimization problem and are essential for guiding the process toward a meaningful and realizable design.

Optimization algorithms
Tosca Structure provides the option to use two different optimization algorithms: a sensitivity-based algorithm, the Method of Moving Asymptotes (MMA), and a condition-based algorithm, the Optimality Criteria (OC) method [21]. For this study, the MMA algorithm was selected due to its robustness and efficiency in structural and topology optimization. MMA operates by iteratively constructing and solving simpler, convex subproblems that approximate the original nonlinear optimization problem. Each design variable is constrained by adaptive “moving asymptotes”, which control the step size and ensure numerical stability. By updating these asymptotes at every iteration, the algorithm avoids large, unstable changes while maintaining steady progress toward the optimal solution. This approach allows MMA to provide a reliable and efficient path for converging to an optimal design [22].

2.4. Research gaps and challenges

WAAM has been extensively researched and utilized in the past period, particularly for the reinforcement of structural components. Nevertheless, research on the reinforcement of slender steel plates to enhance their stability and buckling performance is still limited, particularly with topologically optimized stiffener geometries. The research conducted exclusively used numerical methods to explore its possibilities. The outcomes of numerical investigations exhibit uncertainty due to the lack of experimental validation. Anisotropy and other factors can influence the experimental stability performance of WAAM stiffened slender plates. WAAM allows the fabrication of non-prismatic, optimized structures, thereby improving material efficiency and minimizing waste. Challenges including geometric imperfections, residual stresses, and variability in material properties continue to be significant areas for improvement [23]. This research aims to bridge these gaps by experimentally and numerically evaluating the performance of WAAM-manufactured stiffeners in slender plates, exploring their stability under loading conditions, and investigating alternative geometries to improve buckling resistance. By addressing these areas, this study will contribute new insights into the integration of WAAM technology with structural design and optimization.

To comprehensively investigate the potential of optimizing stiffener geometry, various methodologies may be employed, including modifications to materials or the introduction to entirely different geometrical configurations. The modifications related to the stiffeners could include the utilization of various material combinations. In instead of utilizing rectangular geometries for the purpose of topology optimization, alternative shapes may be considered for implementation. Within the scope of this research project, certain methods may not be incorporated; however, they could prove beneficial for further studies. Specifically for the purpose of this research project, the main focus will lie on the validation of WAAM produced slender plate stiffeners and further geometry optimizations of the latter.

3

Methodology

3.1. Experimental design

This section outlines the experimental program developed to investigate the structural behavior of slender steel plates stiffened using WAAM. A series of specimens were fabricated with WAAM-deposited longitudinal stiffeners and subsequently tested under compressive loading. The experimental program consists of three main components. First, the design and fabrication process of the WAAM-stiffened plate specimens is described in detail. Second, the setup and procedure of the main structural compression tests are presented, which form the core of the experimental study. Finally, additional tensile tests were conducted to characterize the mechanical properties of the steel used, which serve as input for the numerical models described later in this thesis.

3.1.1. Specimen fabrication

In order to create complex stiffener geometries, special manufacturing equipment is needed. The specific stiffener geometry for this research has already been briefly introduced. However, the exact dimensions for this stiffener are shown in Figure 3.1 (and can also be found in Appendix B). As can be seen from the figure, the dimensions and angles are very specific and precise. For that reason, WAAM technology is used. The stiffener's thickness is intended to be uniformly 6 mm. The actual manufacturing of the specimens was done at the welding company Valk Welding B.V. in Alblasserdam. The machine that was used to produce both specimens with the complex stiffeners is shown in Figure 3.2.

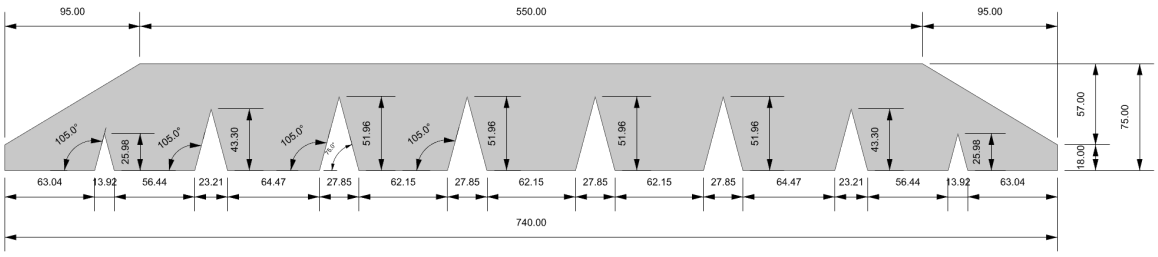

Figure 3.1: The exact geometry of the WAAM-produced stiffeners

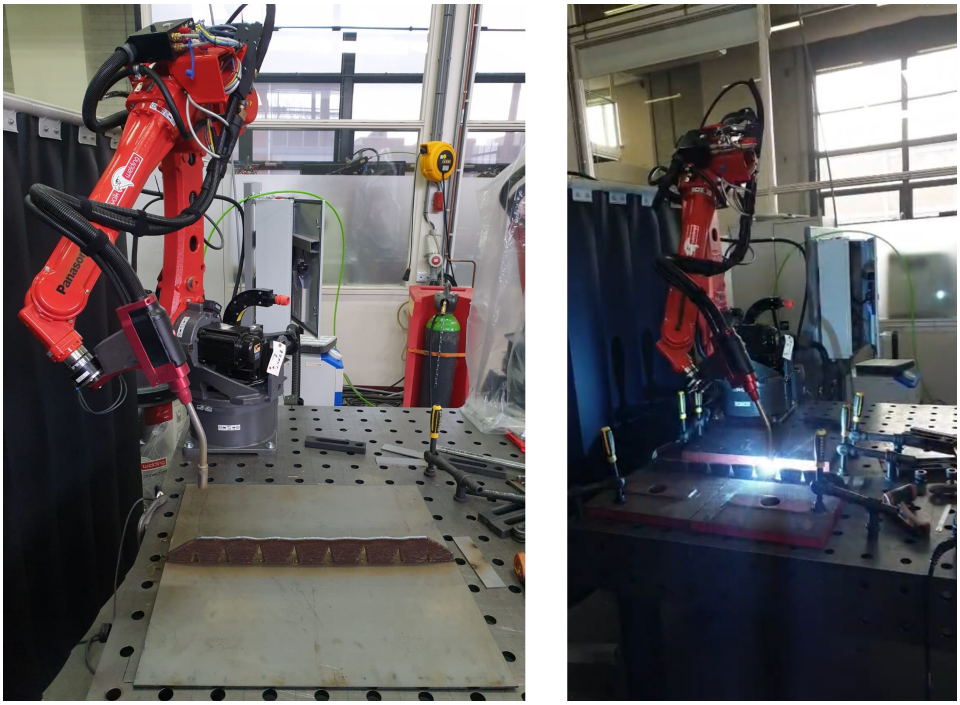

Figure 3.2: The WAAM machine used for the manufacturing of the stiffeners

Before the actual manufacturing of the WAAM specimens, it was necessary to determine appropriate welding parameters. Some of the key parameters that significantly influence the quality of the final product include the voltage and amperage, the welding speed, whether or not a crater time is applied, and the use of a weaving pattern. To identify the optimal combination of these settings, several test welds were performed and evaluated through visual inspection.

During these preliminary tests, it was observed that excessive heat accumulation often caused the molten metal to drip off the edges of the deposited layers. To mitigate this issue, the amperage was reduced to 100 A, which effectively lowered the amount of heat input. However, lowering the amperage too much can adversely affect weld quality by reducing fusion and consistency. Therefore, a balance between sufficient amperage and an appropriate welding speed (0.025 m/min) was established to help reduce heat accumulation while maintaining an acceptable weld quality.

Despite these adjustments, significant heat continued to build up during the deposition process. As a result, the material still tended to flow slowly over the edges of the welding segments, especially as the height of the build increased. This phenomenon led to noticeable height differences along the edges of the segments. Figure 3.3 illustrates this sliding of material off the edge, indicated by the red lines. To partially address this problem and maintain the intended 15-degree overhang angle, a crater time of 1 second was introduced at the ends of each weld segment. The crater function deposits additional welding material for a specified duration at the end of a weld pass, compensating for the loss of material along the edges.

Finally, to further improve weld quality and to achieve the desired weld thickness, various weaving patterns were evaluated. Several configurations were tested, and ultimately a spiral weave was selected as the most effective approach. Figure 3.4 shows the configuration of this spiral weave. The left–right radius of the elliptical weave path was set to 4 mm, while the forward–backward radius was set to 2 mm (half of the lateral dimension).

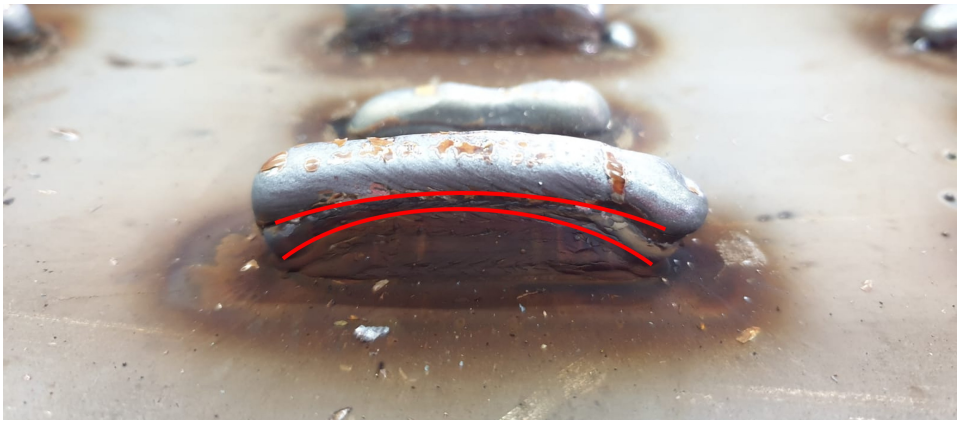

Figure 3.3: The welding material slowly slides off the edge of the weld

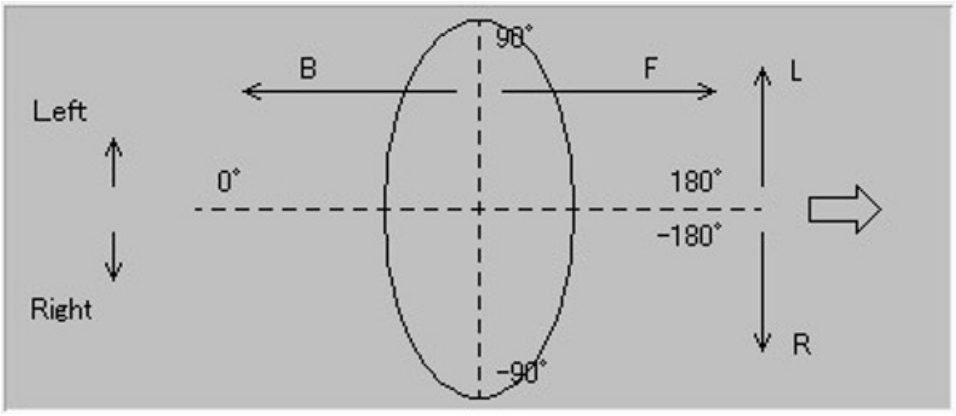

Figure 3.4: Spiral weave welding path. With L and R at 4 mm, B and F at 2 mm

With all critical welding parameters established, the manufacturing process of the WAAM stiffeners could begin. To determine the total number of layers required to achieve the target stiffener height of 75 mm, a preliminary test weld consisting of 10 layers was printed. The total height of this test section was measured and divided by 10 to calculate the average height of a single weld layer. Based on this value, the total number of layers needed was computed to be 47. The stiffener geometry was then divided into 47 corresponding sections within the WAAM software to match this layer count. With the digital model and welding parameters finalized, the actual manufacturing process could proceed.

During the welding process, residual stresses accumulate, often leading to distortion of the base plate. These distortions can significantly affect the WAAM process, especially by altering the relative position between the plate and the welding torch, potentially compromising the stick-out length and overall weld quality. To prevent such deformations, heavy steel weights and clamps were strategically placed on the plate to restrain any out-of-plane movements during deposition.

Before manufacturing the final specimens, a trial stiffener was printed on a test plate to assess the behavior under real welding conditions. This revealed that substantial heat accumulation occurred, particularly as the height of the stiffener increased. To mitigate this issue, high-pressure cold air was applied manually to cool the weld after each deposited layer. In addition, an infrared thermometer was used to monitor the temperature of the weld. Each layer was allowed to cool to below 50°C before the next layer was printed, effectively reducing thermal buildup and minimizing distortion. Using this revised approach, the two final WAAM specimens were successfully manufactured. Figure 3.5 shows the completed stiffeners after production.

It can be observed that around the triangular gaps located at the edges of the weld segments, the

deposited layers still exhibit noticeable sliding due to excessive heat accumulation. This effect is particularly evident in the uppermost layers of the stiffeners, where a distinct wavy surface pattern has developed. At each triangular gap, a pronounced depression or valley can be seen in the weld, resulting in measurable height deviations along the length of the stiffener. In addition to the surface irregularities, the intended target thickness of 6 mm could not be consistently achieved; instead, the final thickness measured approximately 6.4 mm. These deviations highlight the challenges of maintaining both uniform layer geometry and dimensional accuracy when local heat input is not fully controlled, especially in areas where the geometry transitions or overhangs are present.

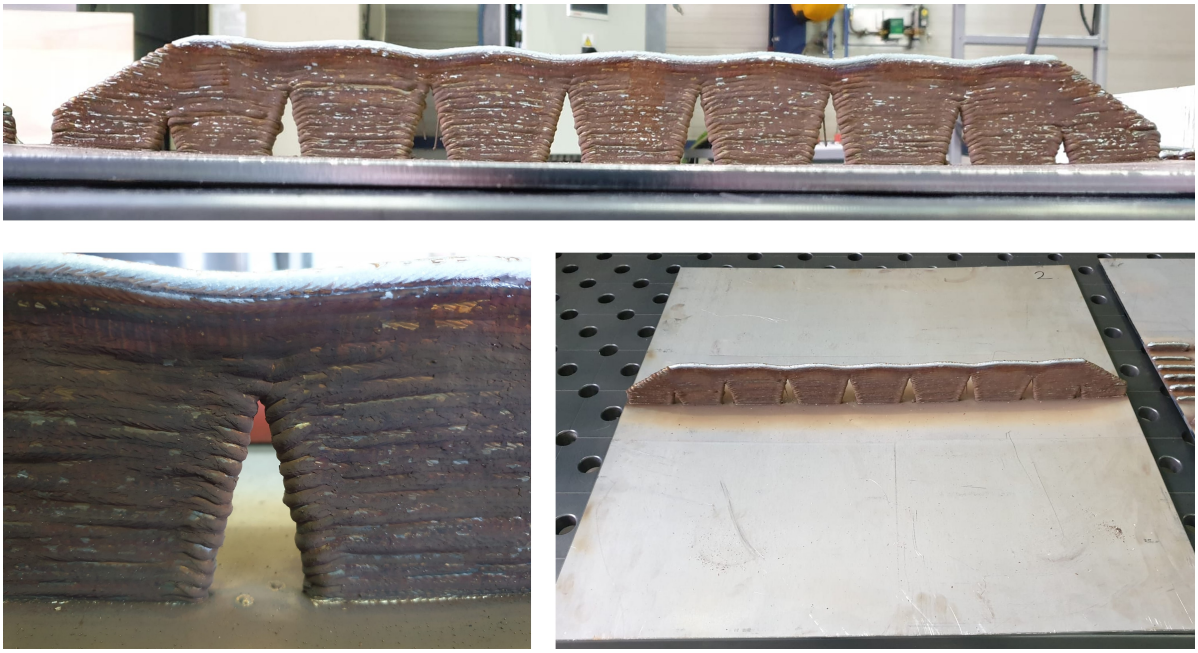

Figure 3.5: Finalized WAAM stiffener specimen

To complete the experimental program, two additional plates featuring prismatic stiffeners were also manufactured. These stiffeners, rectangular in shape with a height of 50 mm and a thickness of 6 mm, were fabricated from the same structural steel as the base plates. Unlike the WAAM-produced stiffeners, these were manually welded onto the plates along both sides of the stiffener using conventional hand welding techniques. The welding was carried out by technical staff at the Stevin Laboratory of TU Delft. To minimize the risk of distortion during welding, the plates were restrained, similar to the approach used in the WAAM process. Figure 3.6 shows the final appearance of the manually welded prismatic stiffeners.

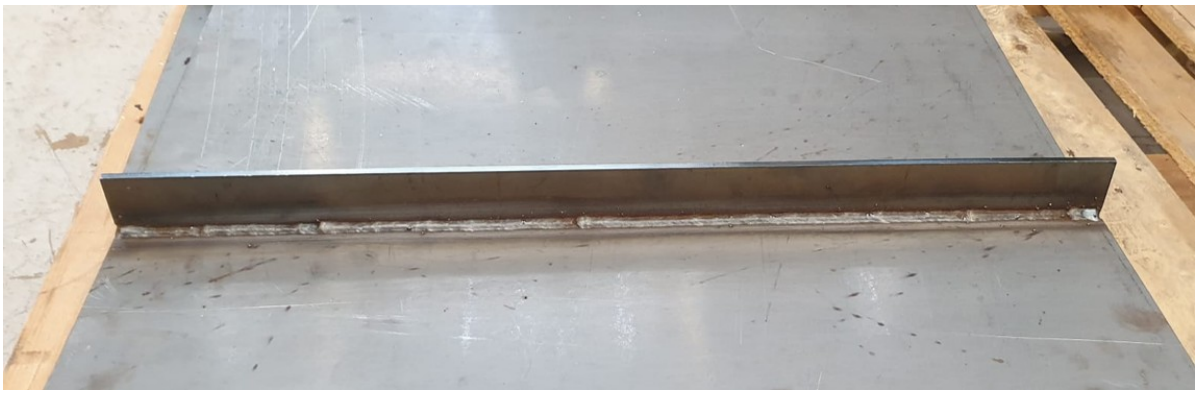

Figure 3.6: Finalized prismatic rectangular stiffener specimen

3.1.2. Experimental test description

3.1.2.1. Test setup

With the specimens successfully manufactured, they were prepared for testing. Each specimen was subjected to a uniaxial compressive load applied in the direction parallel to the stiffener. Figure 3.7 presents a schematic overview of the Instron 8806 testing machine used for this purpose. During the test, the compressive force was applied to the top surface of each specimen. Although the machine generates a concentrated point load, this load was evenly distributed across the full width of the specimen using a modified 300x300x20 mm RHS (Rectangular Hollow Section) profile positioned between the loading head and the specimen. This setup ensured uniform load application and minimized the risk of local stress concentrations during compression.

The RHS profile has been modified in two ways, the first being the addition of holes in the top and bottom webs. To ensure uniform distribution of the point load across the entire specimen, a distributing plate is attached to the top of the RHS profile. The holes allow this plate to be securely bolted onto the profile, as well as the bottom plate. The bottom plate enhances the stiffness of the test setup, preventing any high-stress areas in the setup itself under heavy loading. Like the distributing plate, the bottom plate is also bolted onto the profile. Additionally, to prevent yielding of the RHS profile in the bottom web, an extra reinforcing element is welded to both the top and bottom webs. A continuous rectangular strip runs along the centerline of the profile from end to end, ensuring that stresses are more evenly distributed across the entire profile (Figure 3.7). This design prevents high stress concentrations at the profile-to-specimen interface.

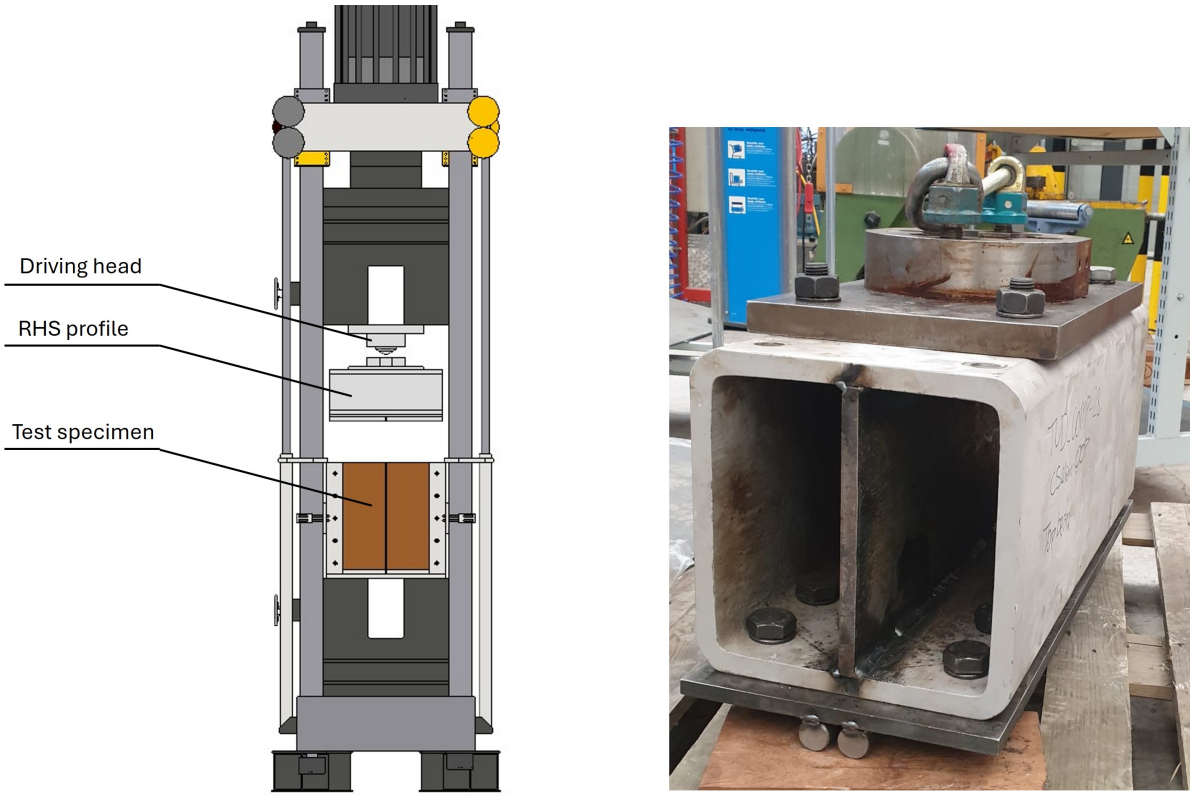

Figure 3.7: Schematic front view of the test setup (left) and the modified RHS profile load distributor (right)

To keep the specimen securely in place during loading, several constraints are applied. To prevent out-of-plane motion, the edges of the specimen plates are positioned between steel rods. As shown in the left image of Figure 3.8, these steel rods are located at the bottom of the RHS profile, leaving a 6 mm gap, matching the plate thickness, so that the plates fit precisely. A similar setup is used at the bottom, where an additional thick plate with attached steel rods ensures alignment.

On the left and right sides of the plates, however, a different method is employed. Instead of steel rods, V-shaped elements hold the plates in place, preventing out-of-plane movement. These elements are bolted to the machine, of which the bolts are indicated in red in the right image of Figure 3.8, and can be adjusted as needed. This setup ensures the plate is fully constrained in the out-of-plane direction along all edges.

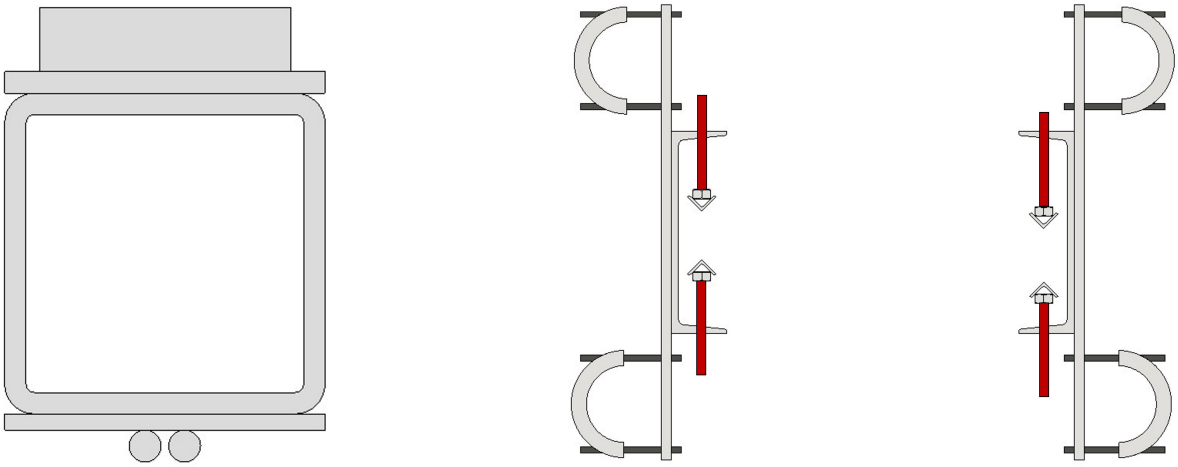

Figure 3.8: Side view of the RHS profile showing the steel rod constraints (left), and a top view of the setup showing the V-shaped bolted element constraints (right)

3.1.2.2. Test procedure

For the actual test procedure, two factors are of primary importance: the loading protocol and the measurement setup used to capture the stability behavior of the plates. As described previously, a concentrated point load is applied and evenly distributed along the top edge of the specimen. This load must be applied gradually to ensure accurate measurement of deformations. If the loading rate is too high, it becomes challenging to record all relevant displacement and strain data; conversely, an excessively slow loading rate would result in impractically long test durations. An appropriate loading speed was determined to be 0.4 mm/min. This velocity corresponds to the rate at which the loading head descends onto the specimen during testing.

To monitor the stability behavior, a single 3D DIC system was employed. In order for the DIC system to reliably register deformations, the entire surface of each plate was prepared with a dedicated DIC spray pattern, consisting of a light grey base coat combined with randomly applied black speckles. After positioning the plate in the test setup, the DIC cameras were aligned centrally with respect to the specimen, so that both sides of the plate—divided by the stiffener—could be captured symmetrically. Figure 3.9 shows the spray-painted plate (left) and the final DIC measurement configuration (right). Because only one DIC system with two cameras was available, it was not possible to fully observe the narrow regions adjacent to the stiffener with both cameras simultaneously. As a result, a small gap appears in the recorded data along this zone. However, this gap is sufficiently narrow that it does not significantly affect the analysis of the overall deformation behavior.

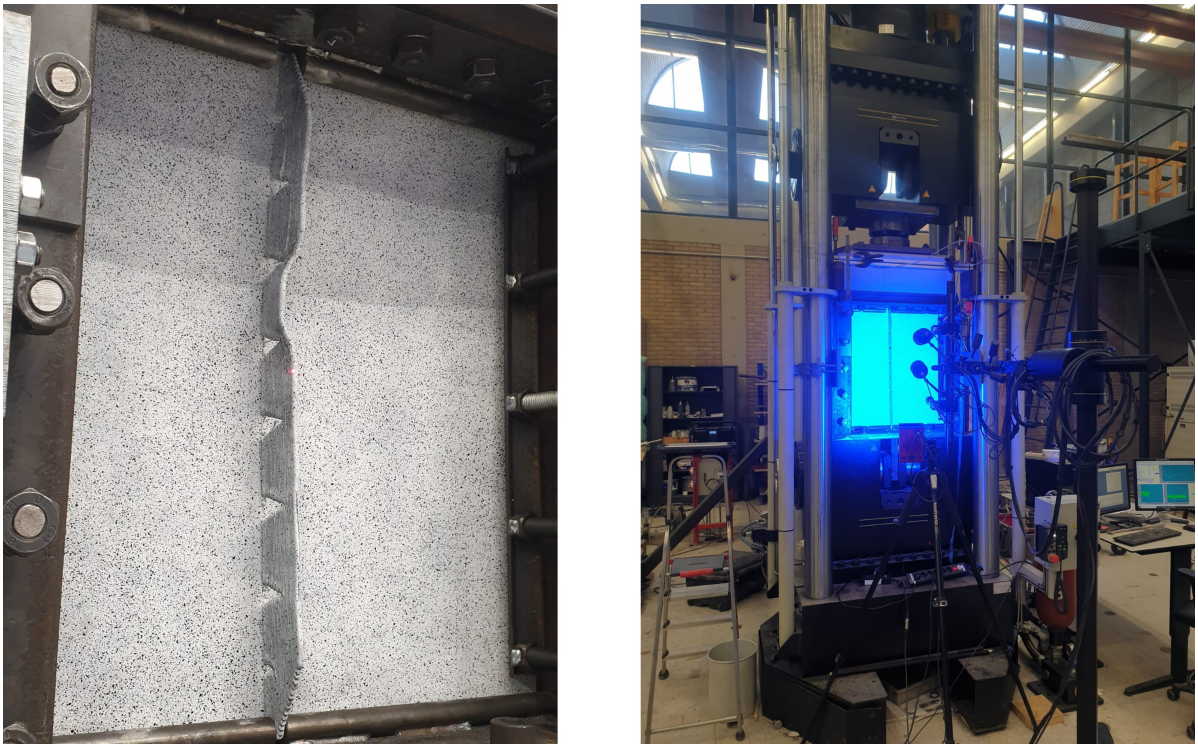

Figure 3.9: The plate with DIC spray paint (left) and the 3D DIC system setup (right)

3.1.3. Tensile testing for material characterization

In addition to the main experiment involving the stability testing of the stiffened plates, a supplementary experiment was conducted to determine the material properties of the base plates. Accurate characterization of these properties was essential to develop reliable FE models. To this end, tensile coupons with a thickness of 6 mm were prepared from leftover S355 steel components that had not been used for the primary specimens. The coupons were machined into the standard dog bone geometry, with the exact dimensions and the corresponding test setup illustrated in Figure 3.10.

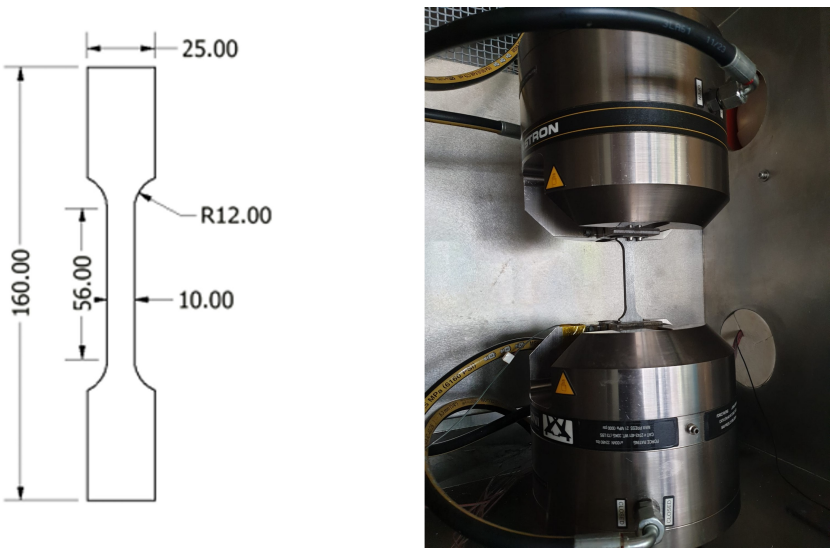

Figure 3.10: The coupon dimensions (left) and the tensile testing setup (right)

The tensile tests were performed using the Instron 1251 machine. A total of three specimens were tested to assess repeatability. During each test, two quantities were recorded over time: the applied

force and the elongation. These measurements were subsequently converted into engineering stress and strain, respectively. The tensile stress was calculated by dividing the measured force by the cross-sectional area of the gauge section, which in this case was 60 mm^2 (10 mm width · 6 mm thickness). The strain was determined by dividing the recorded elongation by the gauge length of 25 mm measured by the extensometer.

The resulting stress–strain relationship is presented in Figure 3.11. As the three tensile tests yielded nearly identical results, only a single representative curve is shown. The graph also highlights the measured yield strength and ultimate tensile strength of the material. The yield strength, in particular, is a critical parameter, as it indicates the onset of plastic deformation, which can significantly influence the stability behavior of the stiffened plates under compressive loading.

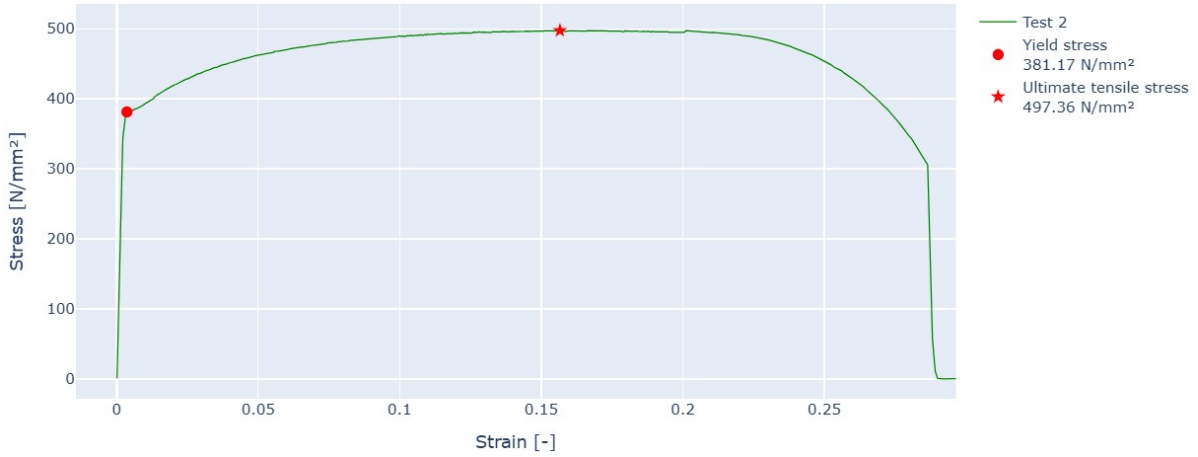

Figure 3.11: Stress-strain model for the S355 steel used for the stability experiment

3.2. Numerical simulations

This section outlines the numerical modeling approach used to simulate the stability behavior of the stiffened steel plates tested experimentally. The primary objective of the numerical simulations is to replicate the structural response observed in the laboratory and to gain further insight into the buckling and post-buckling behavior of the plates. FE modeling is carried out using the software Abaqus/CAE, which allows for the implementation of both geometric and material nonlinearities.

In addition to modeling the global geometry and material behavior, special attention is given to the implementation of initial geometric imperfections. These imperfections, which result primarily from the welding process, significantly influence the buckling response of thin-walled structures. Multiple strategies are employed to introduce imperfections into the numerical models, including the use of 3D-scanned geometries, imperfection fields derived from scan data, and eigenmode-based imperfections extracted from linear buckling analyses. By using a range of modeling approaches, the simulations aim to comprehensively assess the sensitivity of the plate behavior to imperfections and to enable robust validation against experimental results.

3.2.1. General settings

To capture the complex structural response with sufficient accuracy, a nonlinear Riks analysis is employed instead of a conventional linear buckling analysis. The Riks method offers several advantages, as it accounts for both geometric and material nonlinearities. This enables the modeling of the complete load–displacement path, including post-buckling behavior, which is essential for accurately simulating the experimentally observed instability.

For all numerical models in Abaqus, consistent Riks analysis settings are applied. The maximum number of increments is set to 100 to prevent solver termination due to step limitations, although most analyses show buckling within approximately 20 increments. The initial arc-length increment is defined

as 0.01 to maintain a balance between computational efficiency and result accuracy. A minimum arc-length increment of 1E-8 is specified to ensure that the solver can accurately capture the response near the buckling point, where smaller increments are often required. If the increment size is too large in these critical regions, convergence issues may arise due to excessive iteration demands. It should be noted that for these Riks analyses, the solver typically does not fully converge to complete the entire load–displacement path. Therefore, the analysis is manually stopped once buckling is detected. This point is characterized by a significant negative time/load increment value. The time/load increment denotes the time/load gradient in the analysis, indicating that a negative time/load increment signifies a reduction of the load over time.

3.2.2. Geometry and meshing

Each numerical model is divided up into two parts: the plate and the stiffener. Both the stiffener and the plate are modeled using shell elements in Abaqus. This approach efficiently captures the structural behavior of thin-walled components while keeping the computational cost relatively low. By modeling as shells, meshing is now also significantly cleaner and easier.

Both the plate and stiffener are modeled using the same element type, S4R, which is a 4-node (quad-shaped) shell element suitable for thin-walled structures. It features reduced integration (for faster computation), hourglass control (to prevent numerical instabilities), and allows for finite membrane strains (to capture large in-plane deformations). The mesh element sizes differ between the stiffener and the plate. For all specimens, a target element size of 6 mm is used for the stiffener and 8 mm for the plate. This is illustrated in Figure 3.12, which shows the mesh configuration for a plate with a rectangular stiffener; however, the same mesh dimensions are applied to all specimens, including those with WAAM stiffeners. An additional mesh configuration figure of the WAAM stiffener is provided in Appendix B.

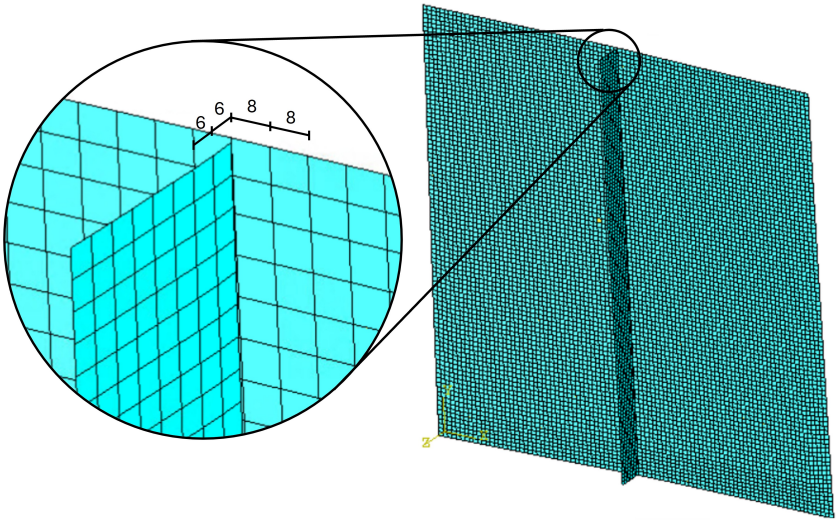

Figure 3.12: General visual representation of mesh sizes of the two different parts

3.2.3. Material properties

To perform a GMNIA analysis, both elastic and plastic material properties must be defined. Since two different materials were used in the experiments, separate sets of properties were assigned. The first material is S355 structural steel, which was used for both the plates and the prismatic stiffeners. For its elastic behavior, a Young's modulus of 210,000 MPa and a Poisson's ratio of 0.3 were applied. The plastic properties of the S355 steel were determined from tensile tests, the results of which are presented in Section 3.1.3.

The second material, ER70s, corresponds to the WAAM-produced stiffeners and requires a different material definition. Based on the properties summarized in Table 2.2 of the Theory section, the elastic parameters were set to an average Young's modulus of 190,000 MPa and a Poisson's ratio of 0.29. To

describe its plastic behavior, a bilinear material model was adopted: the elastic region follows a slope E, while the plastic region continues with a reduced slope of $E/100$. The transition between these two regions occurs at a yield stress of $f_y = 420$ MPa. In all cases, isotropic material behavior was assumed in the FEM software.

3.2.4. Boundary conditions and loading

To prevent any rigid body motion of the model, appropriate boundary conditions are applied. These boundary conditions are defined not only to ensure numerical stability, but also to replicate the experimental setup as accurately as possible. The resulting configuration is illustrated in Figure 3.13, where a perfectly shaped plate with a rectangular stiffener is shown for clarity. This boundary condition setup serves as a general representation for all tested specimens, independent of the stiffener geometry or the presence of imperfections.

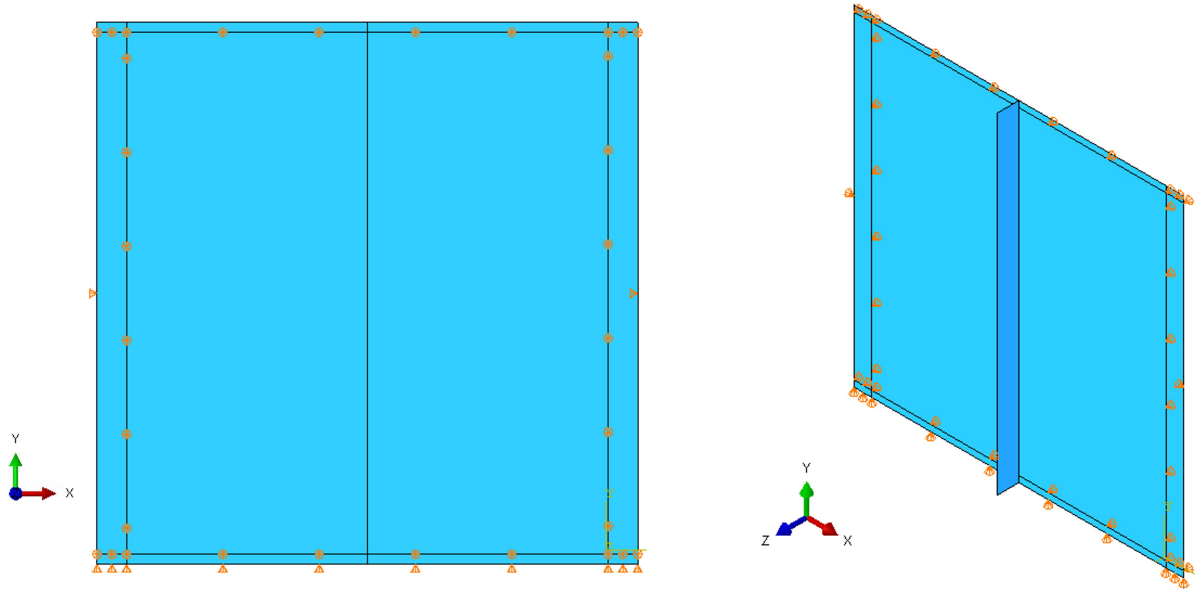

Figure 3.13: General BC configuration resembling the experimental setup

The plate is constrained in the out-of-plane (Z) direction near its edges. Along the top and bottom edges, this constraint spans the full width of the plate, from left to right. On the vertical sides, however, the out-of-plane constraint does not extend fully to the ends of the plate. The exact dimensions of this boundary condition are shown in Figure 3.14, indicated with a dashed line, reflecting the experimental setup with a resolution of 1 mm.

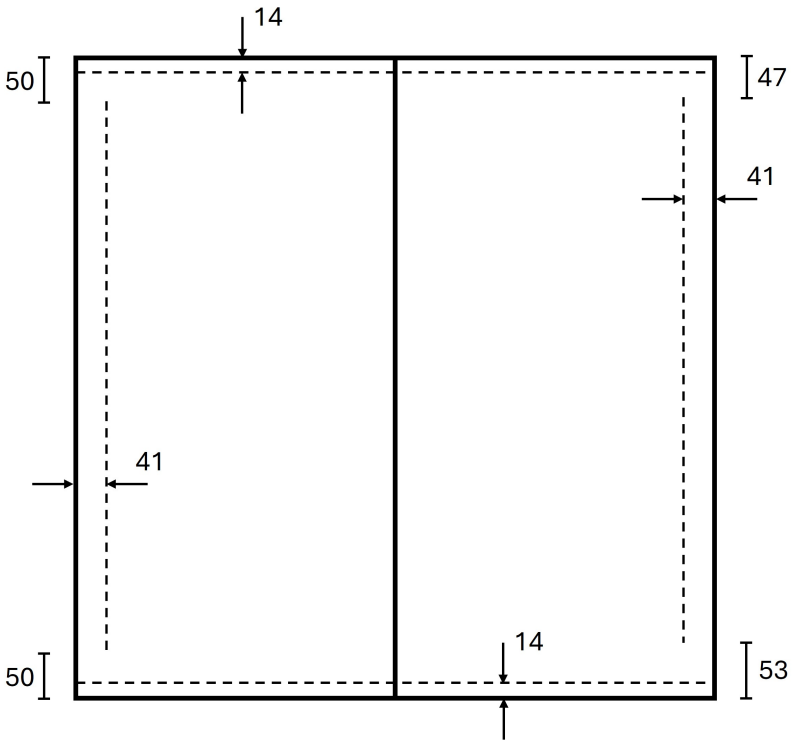

Figure 3.14: A schematic of the out-of-plane BC dimensions

To restrict horizontal movement (X-direction) during loading, additional constraints are applied at two points located at the mid-height of the vertical edges. Due to the predominantly vertical nature of the applied load, lateral displacement in the X-direction is minimal, and fully constraining the sides is unnecessary. This approach helps to reduce computational effort without compromising accuracy.
Furthermore, a line constraint is applied at the bottom edge of the plate in the Y-direction to prevent vertical translation.

The load applied to the plate is introduced as a shell edge load, directed in the global Y-direction. It is important to note that this load direction remains vertical and does not follow the local tangent of the plate edge. For the Riks analysis, an initial load magnitude must be specified to initiate the solution process. During the analysis, this initial load is incrementally scaled by a Load Proportionality Factor (LPF) at each arc-length step, thereby constructing a full loading path over time.
In this study, the initial shell edge load is set to 1000 N/mm. To relate this to the concentrated point load applied in the physical experiment, the shell edge load is multiplied by the loaded edge length and the corresponding LPF. Dividing this result by 1000 yields the equivalent load in kilonewtons [kN]. This simplifies the conversion: the equivalent point load in [kN] can be obtained by multiplying the plate edge length by the LPF.

3.2.5. Geometric Imperfections Implementation

Three approaches were considered for implementing the geometric imperfections of the plates. The first approach involves direct geometry reconstruction in Rhino, where the measured surface is modeled to reproduce the plate's deformed shape. The second approach applies a grid-based out-of-plane interpolation method, in which the imperfection data are mapped onto a predefined nodal grid, allowing the out-of-plane deviations to be assigned directly to the FE model. The third method involves an eigenvalue approach, where the initial imperfections of the plate are based on the buckling modes of a linear buckling analysis.

3.2.5.1. 3D-scanned geometry reconstruction

The first method used to implement geometrical imperfections involves reconstructing the plate geometry based on 3D scan data. The scans provided a highly detailed point cloud consisting of tens of

millions of points, offering an accurate representation of the plate surface. This high density was the result of using a scanner resolution of 0.2 mm. However, due to computational limitations, the point cloud had to be downsampled. A Python script was developed to perform grid-based (voxel) downsampling, reducing the number of points to approximately 30,000; the code is included in Appendix A.

The reduced point cloud was imported into Rhino, where a custom Grasshopper script was used to fit surfaces over the data. An example of the resulting surfaces, shown in red, is presented in Figure 3.15. Only surfaces were created, as the subsequent FE modeling step makes use of shell elements only.

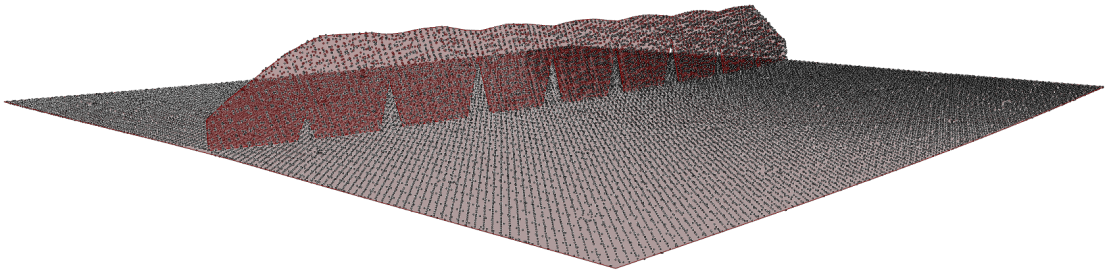

Figure 3.15: The Grasshopper surfaces that fit over the data for WAAM1

Once finalized, the surfaces were baked into Rhino and exported as a STEP file, ensuring interoperability and precision by preserving the geometry across the different CAD software platforms. The exported geometry was then imported into Abaqus for further analysis. The final geometry, including the captured welding-induced imperfections at a 1:1 scale, is shown in Figure 3.16. For each of the four 3D scans of the four distinct specimens, the same procedure is followed.

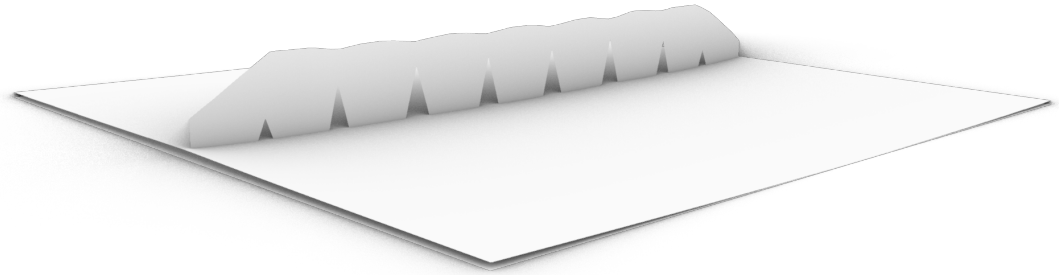

Figure 3.16: The final geometry reconstruction outcome for WAAM1

In Abaqus, the STEP file is imported as two separate parts: one representing the stiffener and the other the plate. These parts visually display the geometrical imperfections as reconstructed from the scan. Boundary conditions, loads, meshing, and other analysis steps can then be directly applied to this imperfect model without requiring any additional processing.

3.2.5.2. Python-scripted imperfection field

The second method for implementing geometrical imperfections focuses solely on the out-of-plane deviations in the z-direction. This approach relies not only on the previously acquired 3D scans of the specimen, but also on the mesh data from an idealized Abaqus model of the plate.

As in the geometry reconstruction method described in Section 3.2.5.1, the initial step involves downsampling the high-resolution 3D scan point cloud to make it computationally manageable. The original scan contains tens of millions of points, which are reduced to a smaller set stored in a text file containing

the 3D coordinates of each point.

In parallel, the coordinates of the mesh nodes from a perfectly shaped Abaqus model (i.e., without any imperfections) are extracted. The mesh type and size used in this model are described in Section 3.2.2. These mesh node coordinates are also exported as a text file and serve as the basis for defining the imperfection field.

To combine the scan data with the mesh, the point cloud is aligned and translated to overlap with the Abaqus mesh nodes. Figure 3.17 illustrates this alignment: the red points represent the downsampled 3D scan, while the blue points indicate the Abaqus mesh nodes. Note that the stiffener is intentionally excluded from this visualization to isolate the plate; as a result, a visible gap appears along the plate's centerline. This is acceptable, as the plate and stiffener are treated separately in this method. Also, the figure's axes are not to scale — the actual imperfections are significantly smaller in magnitude.

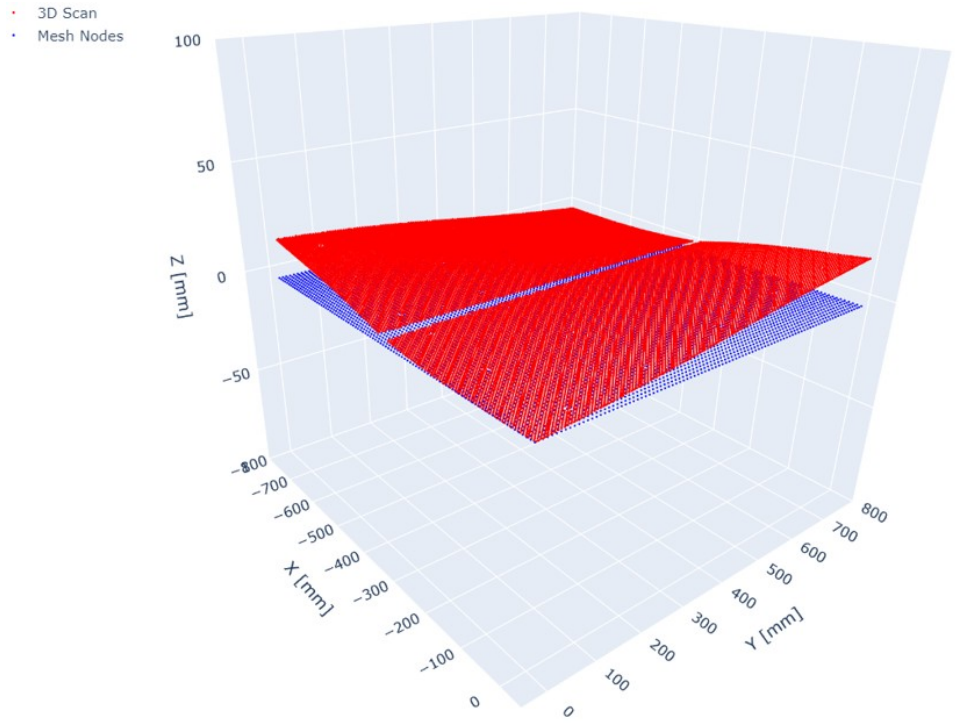

Figure 3.17: Comparison between the scanned trace (red) and mesh trace (blue)

The next step is to compute the out-of-plane imperfections at each mesh node by interpolating the z-coordinate deviation from the scan data. This is done using the *griddata* function from the SciPy library, which performs triangulation-based interpolation. The resulting imperfection field assigns a Δz value to every mesh node, which is then added to the original z-coordinate. An example of the final imperfection field is shown in Figure 3.18, where the previously visible gap at the centerline has also been filled due to the interpolation. The Python code used to calculate the imperfections is found in Appendix A.

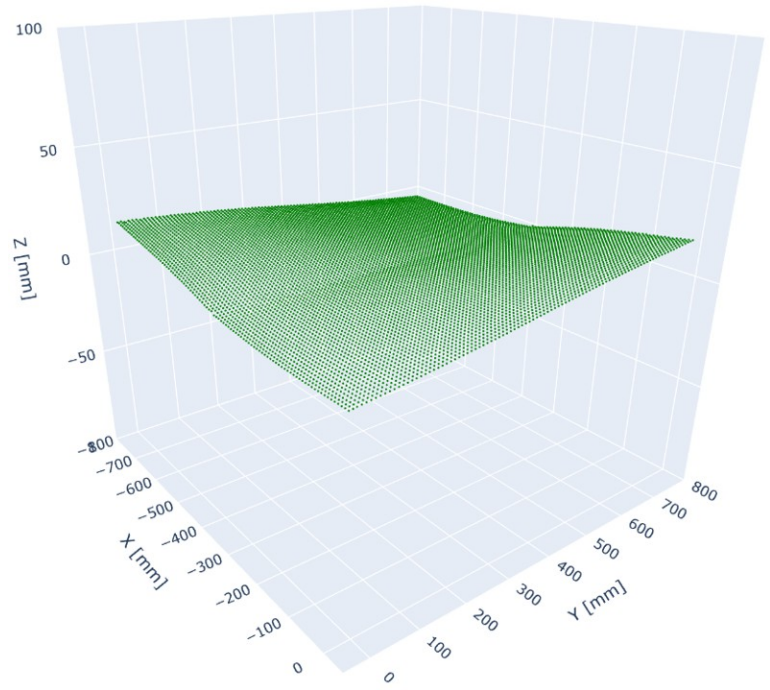

Figure 3.18: Interpolated out-of-plane imperfection field applied to mesh nodes

To import these imperfections back into Abaqus, a different approach is used than for the geometry reconstruction method. A job is created in Abaqus using the perfect geometry model, and an *input file* (.inp) is generated. This can be done by either running a basic analysis or manually writing the input file without execution. The generated file includes all relevant model data, including the original mesh node coordinates. The implementation of imperfections is achieved by replacing the original z-coordinates in the input file with the modified ones obtained from the interpolation script. Running a new analysis with this modified input file results in a simulation that incorporates the scanned imperfections. In essence, this method applies an additional Δz to each mesh node, directly embedding the measured out-of-plane deviations into the FE model.

As the project progressed, it became apparent that implementing the imperfections based on the initial 3D scan data would lead to results not resembling the experimental data. This issue arose because the plates were scanned prior to being positioned in the experimental setup. The act of placing and aligning the plates in the setup induced additional deformations, resulting in imperfections that differed from those captured in the initial scan. To address this discrepancy, the imperfections were instead derived from the DIC measurements. Specifically, the first reference stage of the DIC models was exported as a mesh representation of the undeformed geometry. The nodes of this mesh were then extracted to create a new point cloud dataset, comparable to the point cloud obtained from the 3D scan. This approach allowed the same methods for implementing the imperfections to be applied consistently, now using a more representative and accurate geometry. The 3D scans were not considered without value; rather, they were later utilized for the implementation of residual stresses.

3.2.5.3. Eigenmode-based imperfection

Additionally, a third method is used as a reference: a nonlinear buckling analysis based on the first buckling mode of a linear buckling analysis (LBA). In this case, a perfect plate (i.e., without any geometric imperfections) is analyzed using an LBA, and the first buckling mode shape is extracted. This mode shape is then scaled by an assumed imperfection amplitude and superimposed onto the geometry to perform a nonlinear analysis. According to the Eurocode (EN 1993-1-5, Annex C), the magnitude of the equivalent geometric imperfection is taken as the minimum of a/200 and b/200, where a and b denote the edge lengths of the plate or subpanel. For the present case, the smallest subpanel length corresponds to half the plate width, i.e. 375 mm. This results in a prescribed imperfection amplitude of 1.875 mm, which is applied as the scaling reference for the selected eigenmode shape. This method

does not incorporate the actual measured imperfections of the plates. Instead, it introduces artificial imperfections based on the plate's first buckling mode, solely for the purpose of enabling a nonlinear analysis. Consequently, the first two methods, both of which are based on the real geometry, are expected to yield more accurate results.

The use of measured imperfections provides valuable insight into the behavior of the specific test specimens, but it does not necessarily capture the general imperfection sensitivity of the plate. By introducing an imperfection field based on the first buckling mode, a consistent and standardized representation of the critical imperfection shape is obtained. This approach allows for a direct comparison with design code assumptions and ensures that the numerical analyses are not only adjusted to the tested geometry but are also representative for practical design situations where the exact imperfection field is unknown. Consequently, the eigenmode-based analyses complement the scan-based analyses by providing a broader and more generalizable assessment of the plate's stability behavior.

3.2.6. Residual stress implementation

Throughout the numerical investigation, it became clear that incorporating only the imperfections obtained from the DIC scans was insufficient for capturing all relevant validation conditions. A critical missing factor was the inclusion of residual stresses. These stresses arise from the welding of the plates in both the WAAM stiffener and prismatic stiffener configurations, which causes significant distortion. After welding, the plates reach a force equilibrium in their deformed state. However, when the plates are pushed and aligned into the experimental setup, they are forced away from this equilibrium shape. The physical boundary conditions of the setup restrict this movement, causing the plates to develop residual stresses as they attempt to return to their original distorted form.

The process to quantify these stresses involves several steps. First, the displacements caused by installing the plate into the setup are calculated. This is achieved by subtracting the DIC-measured imperfections from the 3D scan imperfections, yielding the exact displacement field resulting from the installation process. Figure 3.19 compares the 3D scan and DIC deformed states for both stiffener types: the WAAM stiffener from the second experiment (top) and the prismatic stiffener from the third experiment (bottom).

(a) Imperfect plate geometry of 3D scan (red) and DIC (purple) for experiment 2 (WAAM)

(b) Imperfect plate geometry of 3D scan (red) and DIC (purple) for experiment 3 (prismatic)

Figure 3.19: Comparison between the imperfections of the plates with the WAAM stiffeners and the prismatic stiffeners

In the figure, the stiffeners are not shown in order to avoid visual obstruction. It should be noted, however, that the stiffeners are positioned along the center lines of the plates and are oriented perpendicular to the viewing plane, i.e. extending in the direction “into the screen”. The red plates shown in the figures represent the 3D scans of the standalone plate. At a certain stage in the visualization, the color suddenly changes from red to purple. The purple plates correspond to the initial reference stage of the DIC measurement, which already includes the plate positioned in the experimental setup with its initial imperfections. Consequently, the transition from red to purple indicates the point where the scanned standalone plate (red) passes beneath the setup plate (purple). For the WAAM stiffener (top figure), visual inspection reveals only minor differences between the two imperfection fields. In contrast, the prismatic stiffener configuration (bottom figure) exhibits substantial differences, on the order of a centimeter, particularly in the bottom-left and top-right regions of the plate.

To provide a more quantitative comparison of the imperfection differences observed, the out-of-plane imperfection profiles along the width of the previously presented plates are shown in Figure 3.20. The figure presents the profiles obtained from both the 3D scan (red) and the DIC scan (purple) at two different locations on the plate: one along the bottom edge and the other through the mid-width at the plate’s center. These mid- and edge locations are expected to show the largest deformations. In both cases, the profiles span the full plate width in the direction perpendicular to the stiffener. The vertical axis represents the imperfection magnitude, while the horizontal axis indicates the position along the plate width.

The upper plot corresponds to the second experiment with the WAAM stiffener, whereas the lower plot corresponds to the third experiment with the prismatic stiffener. To enable a consistent comparison of imperfections before and after positioning the specimen in the experimental setup, the mid-width profiles (solid lines) should be compared directly to one another, as should the edge profiles (dashed lines).

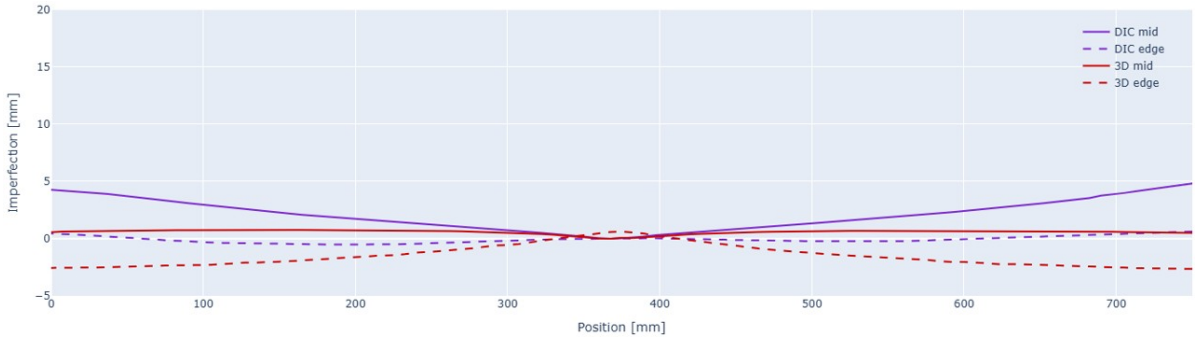

(a) Imperfection profiles along the mid-width (solid) and bottom edge (dashed) for experiment 2 (WAAM).

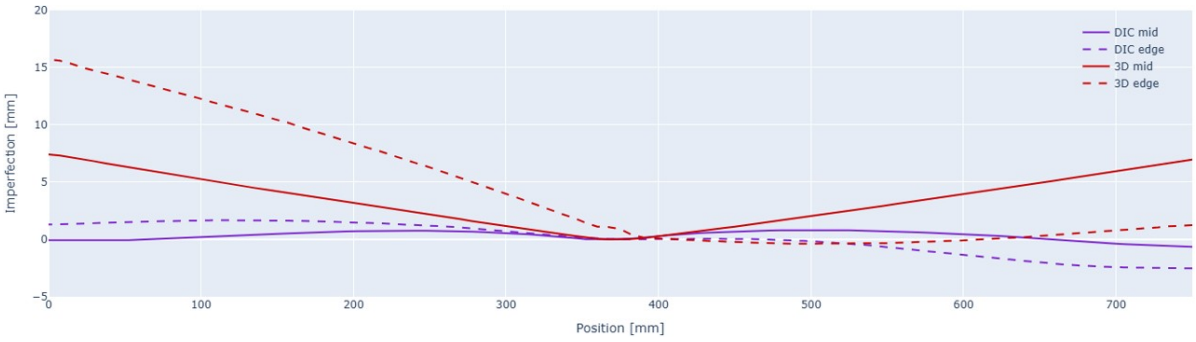

(b) Imperfection profiles along the mid-width (solid) and bottom edge (dashed) for experiment 3 (prismatic).

Figure 3.20: Out-of-plane imperfection profiles obtained from 3D scan and DIC scan for two plate experiments. Solid lines represent the mid-width profiles, while dashed lines correspond to the bottom-edge profiles, both spanning the full plate width perpendicular to the stiffener.

When comparing the mid-width profiles from the second experiment, the difference in imperfections

induced by positioning the plate in the setup is found to be less than 5 mm. For the corresponding edge profiles, the maximum deviation is approximately 3 mm. In contrast, the third experiment with the prismatic stiffener exhibits considerably larger differences. Here, the mid-width profiles show a maximum imperfection difference of about 8 mm, while the edge profiles display even greater deviations, exceeding 16 mm, which is almost four times higher than the second experiment.

The next step is to translate these handling displacements into a residual stress field. In Abaqus, this is done by applying out-of-plane displacement boundary conditions at the nodes corresponding to the experimental restraints, based on the calculated installation displacements. Additional constraints in other directions are included solely to prevent rigid body motion. Running this analysis produces the residual stress distribution associated with the installation process. Figure 3.21 shows the resulting Von Mises stress fields for both stiffener configurations. The WAAM stiffener case exhibits minimal residual stresses apart from localized hotspots near the boundary conditions, with only a faint stress region around the stiffener itself. The prismatic stiffener case, however, displays a pronounced and asymmetric residual stress pattern that is likely to influence the plate's stability behavior.

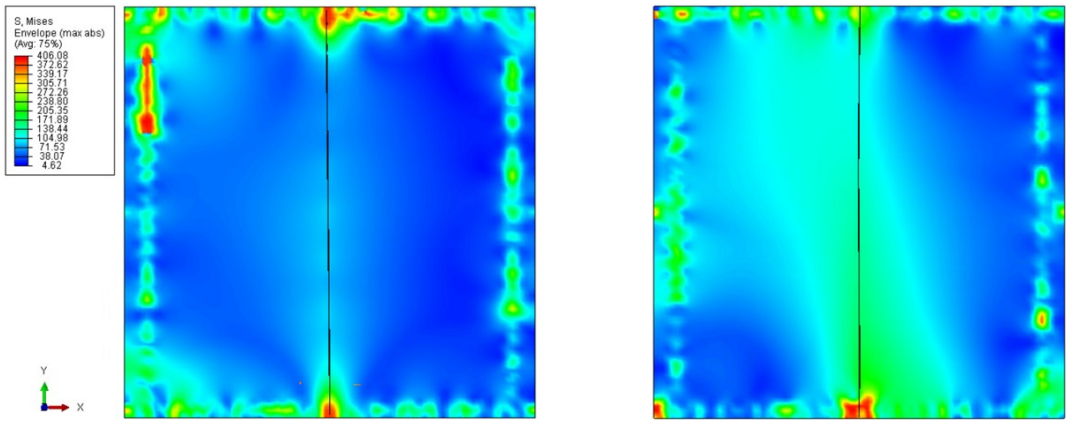

(a) Residual stresses in experiment 2 (WAAM) **(b)** Residual stresses in experiment 3 (prismatic)

Figure 3.21: Comparison between the residual stress fields of the two different stiffener configurations

These calculated residual stresses, along with the associated displacements for the entire plate, are then imported into a new FE model as the initial state. A nonlinear buckling analysis is subsequently performed, incorporating realistic boundary conditions and the residual stress field. This procedure was implemented for the prismatic stiffener configuration, as its distinct imperfection difference and therefore its stress distribution has the potential to significantly affect the structural response. As a further step in the validation process, an alternative approach was adopted. Instead of considering the associated displacements derived from the applied BC displacements, the experimentally measured initial plate imperfections obtained through DIC were employed as the input.

3.3. Optimization process

The optimization phase of this research was carried out in several steps. First, a new initial stiffener geometry was defined, consisting of a prismatic rectangular cross-section taken as the starting point. Based on this cross-section, a revised path and location configuration of the stiffener was assigned on the plate. Following this, the optimization procedure was applied. The defined initial stiffener shapes were subjected to a topology optimization process to evaluate their performance. The outcomes were assessed in terms of stiffener efficiency, which was measured by considering both the weight of the stiffener and the maximum buckling load capacity of the plate.

3.3.1. Initial stiffener shape and configuration

As the basis for the topology optimization study, a set of prismatic rectangular stiffeners was created with a new initial geometry, to evaluate the relative efficiency of the TO stiffener. The new initial shape included determining its basic shape, location on the plate, and thickness. This stiffener with new initial

shape is then topologically optimized and compared to its initial shape. To do this, the deformation behavior of a plate with no stiffener under uniaxial compression was first examined.

Figure 3.22a shows the deformation pattern of a plate without any stiffeners, exhibiting a regular global buckling mode. It is known that decreasing the out-of-plane displacements leads to an increase in the ultimate buckling resistance. By adding a prismatic stiffener along the regions of largest displacement, and aligning it with the load path in the plate under uniaxial compression, the overall out-of-plane displacements can be significantly reduced. However, introducing such a stiffener changes the buckling behavior. As shown in Figure 3.22b, the governing mode now becomes local buckling.

With this concept in mind, a new initial stiffener geometry was defined. The configuration consists of two stiffeners placed on a single plate, each following an ellipse-like curved path and meeting at the midpoints of the plate edges. The purpose of this layout is to eliminate the local buckling zones that were observed in the plate configuration with a single prismatic stiffener placed along the centerline.

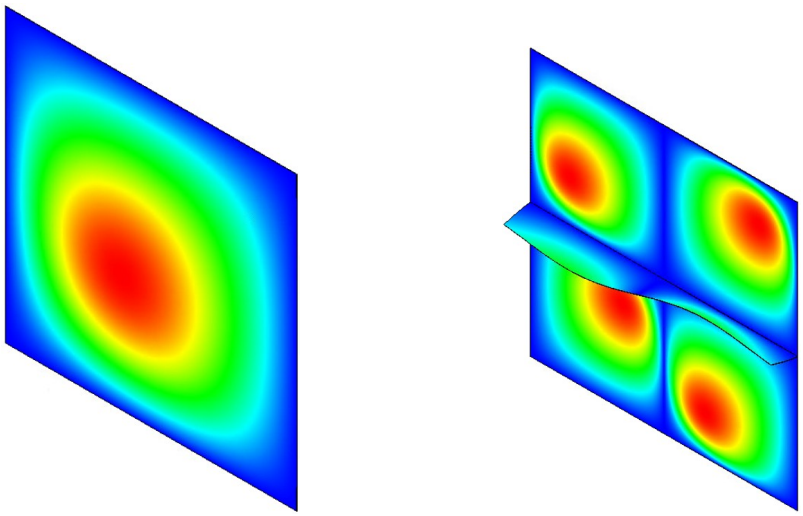

(a) Example of the out-of-plane displacements of the plate with no stiffener

(b) Example of the out-of-plane displacements of the plate with prismatic stiffener

Figure 3.22: Out-of-plane displacement changes after adding a prismatic stiffener along the center line of the plate

Nevertheless, the optimal curvature of the ellipse-shaped stiffeners remains uncertain in terms of both stability performance and topology optimization outcomes. To address this, three variants of the initial stiffener geometry with a thickness of 10 mm each were investigated, each defined by a different curvature parameter. These variants are illustrated in Figure 3.23 and are categorized as small, medium, and large curvature, corresponding to minor ellipse radii of 120 mm, 450 mm, and 800 mm, respectively. By analyzing these three alternatives, a clearer understanding of the influence of stiffener curvature on structural performance can be obtained.

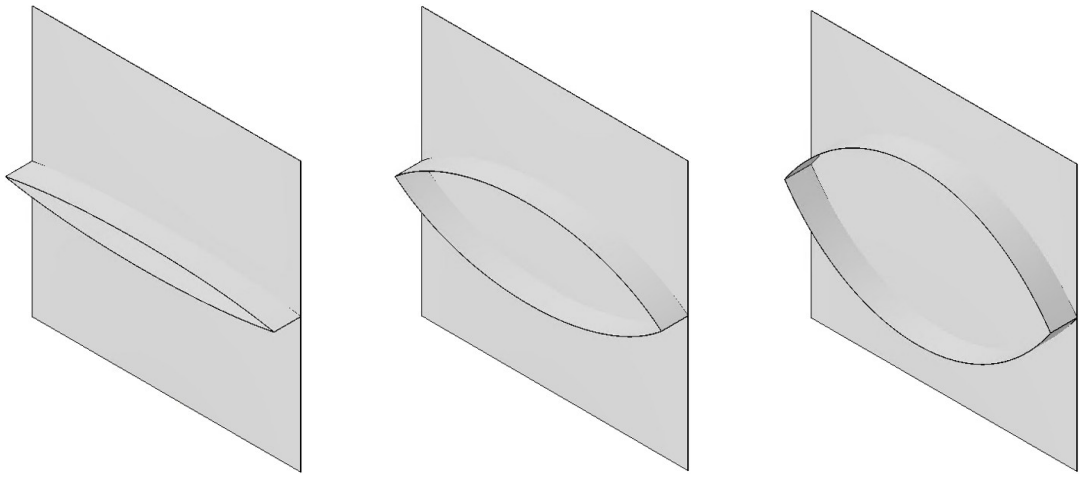

(a) Small variant ($\kappa = 0.284 \cdot 10^{-3}\ mm^{-1}$)

(b) Medium variant ($\kappa = 1.065 \cdot 10^{-3}\ mm^{-1}$)

(c) Large variant ($\kappa = 1.893 \cdot 10^{-3}\ mm^{-1}$)

Figure 3.23: Three initial stiffener geometries with different stiffener curvatures, ranging from small to large

3.3.2. Topology optimization of stiffener geometry

The next step was to perform the topology optimization of these initial geometries using Tosca Structure in combination with Abaqus. The FE model setup for this process was similar to that used for a standard buckling analysis, with some modifications. A 5 mm bow imperfection was applied to the plate. The choice for applying a bow-shaped imperfection in the analysis is motivated by experimental observations from the first part of this research. During the additive manufacturing of the stiffeners using the WAAM process, it was found that the deposition of material onto a slender plate induced a bow-like imperfection field in the plate. The resulting geometric deviations not only exhibited a similar shape but also comparable imperfection magnitudes to those applied in the numerical model, thereby justifying the use of this imperfection type in the TO part of this study.

The optimization task was based on the SIMP method for material interpolation. The objective function was defined as the minimization of the maximum out-of-plane displacement at the center of the plate, as this is a key indicator for the onset of buckling. The constraint applied was a stiffener volume reduction, which was adjusted until the desired balance between weight savings and performance was achieved. For this study, a final volume reduction of 50% was used, meaning the optimizer retained half of the initial stiffener volume while attempting to reduce displacements.

To ensure the resulting design would be manufacturable using WAAM, additional geometric constraints were introduced. Specifically, a maximum overhang angle of 60° was imposed to comply with the process limitations. With all parameters defined, the optimization was run, and the topologically optimized stiffener geometries were obtained, as shown in Figure 3.24.

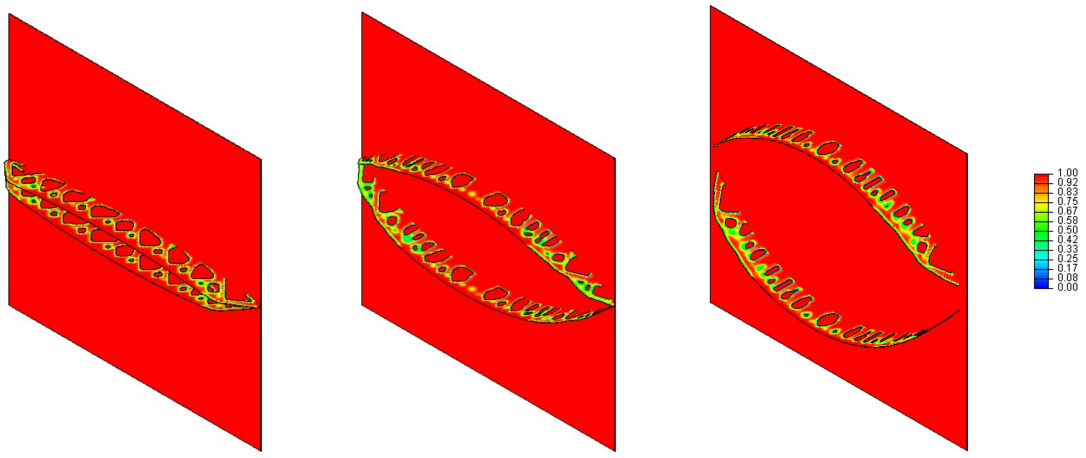

(a) Small variant **(b)** Medium variant **(c)** Large variant

Figure 3.24: The material density contour plots of the three TO stiffener variants

The figure illustrates the material density distribution of the stiffener following the optimization process. In this representation, red regions correspond to a density value of 1, indicating that the stiffener thickness at those locations remained unchanged at 10 mm. Smaller areas in green or yellow indicate regions where the thickness was reduced. However, the number of such reduced-thickness regions is limited for all variants. For the final design, a simplified geometry was therefore adopted, maintaining the original uniform thickness across the entire stiffener.

3.3.3. Analysis procedure

To evaluate the performance of the newly acquired stiffener geometry, specific criteria are required to quantify its effectiveness relative to the new curved stiffeners with prismatic rectangular cross section. This comparison is based on two primary factors:

- The weight of the stiffeners (W).
- The ultimate buckling load of the plates reinforced with the different stiffeners (R_b).

The general BC setup used to calculate the buckling resistances for these models is shown in Figure 3.25. Out-of-plane displacements were restrained along all edges of the plate. To prevent rigid body motion, an additional vertical displacement constraint (Y-direction) was applied at the plate's center, while horizontal displacement constraints (X-direction) were placed at the midpoints of the top and bottom edges. This BC configuration was applied identically to all FE models in this study.

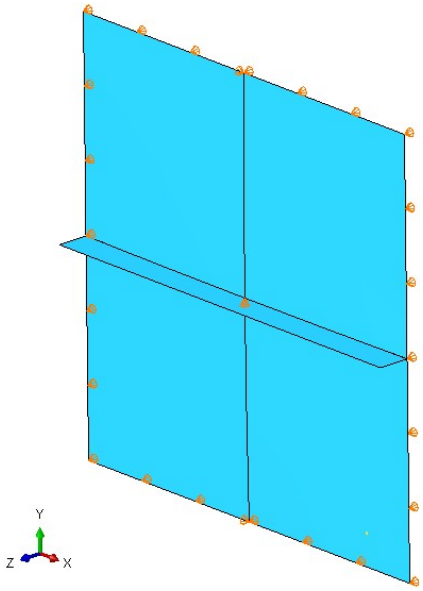

Figure 3.25: General BC configuration for the TO FE models

For material properties, a bi-linear S235 steel model was used for both the plate and stiffener, with a Young's modulus of 210 000 N/mm², Poisson's ratio of 0.3, and yield stress of 235 N/mm². Both components were modeled using S4R shell elements. A target mesh size of 10 mm was applied to the plate, and 6 mm to the stiffeners. These mesh sizes were maintained for all FE models containing the curved prismatic stiffeners. To account for initial geometric imperfections, a bow imperfection of 5 mm was introduced into the base plate geometry.

For each factor (weight and resistance), a ratio is then computed between the new TO stiffener and the curved prismatic stiffener. The weight ratio, W_r, is defined as the weight of the TO stiffener divided by the weight of its prismatic counterpart: the curved prismatic stiffener, while the resistance ratio, R_r, is similarly defined as the ultimate buckling load of the TO stiffener divided by that of the prismatic stiffener:

$$W_r = \frac{W_{TO}}{W_{prism}} \qquad R_r = \frac{R_{TO}}{R_{prism}} \tag{3.1}$$

The overall stiffener efficiency, E_s, is then calculated as:

$$E_s = \frac{R_r}{W_r} \tag{3.2}$$

This formulation allows the relative changes in weight and resistance to be compared directly. A new TO stiffener geometry may have achieved a 50% weight saving; however, these reductions also lead to a decrease in buckling resistance due to the lower material volume. The efficiency metric E_s quantifies this trade-off. If the relative reduction in weight is greater than the relative reduction in resistance, then $E_s > 1$, indicating that the TO stiffener is more efficient than the prismatic stiffener, and that it is worth manufacturing to reduce the total material use.

In the efficiency calculations, the weight of the stiffeners can be replaced by their volume. This substitution is valid because both the WAAM and S235 materials have the same density of 7850 kg/m³, making the weight ratios directly proportional to the volume. The buckling resistance of the plates can be determined using Riks analyses, following the same procedure as applied in the numerical investigation, which is described in detail in Section 3.2.

4

Results

4.1. Experimental results

The first section of the results chapter contains an analysis of the experimental results, obtained using the DIC system. The software used to analyze the DIC results provided accurate visuals of the stability behavior during the experiment, and can be found in this section.

4.1.1. Plates with additively manufactured stiffeners

This subsection discusses the results obtained from the experiments on plates reinforced with WAAM-produced stiffeners. The analysis focuses on the measured displacement fields recorded during testing. These results provide detailed insight into the deformation patterns and buckling response of the specimens.

Experimental results - experiment 1

The initial stage of the analysis involves determining the buckling resistance of the plate for the first experiment. The experimental testing machine recorded a maximum uniaxial load of $991\ kN$, which is taken as the buckling resistance of the plate.

The corresponding buckling mode at this load is shown in Figure 4.1. The figure presents the out-of-plane displacement field of the plate, where blue regions correspond to negative displacements and red regions correspond to positive displacements. In the first experiment, the displacement field is dominated by negative out-of-plane displacements, and it is mostly governed by local buckling of the plate. It has a pronounced hotspot located near the top-left corner of the plate. The right side of the plate also exhibits negative displacements, but with a significantly smaller magnitude. Positive displacements are observed at the bottom of the plate; however, their magnitude is lower than that of the dominant negative displacements.

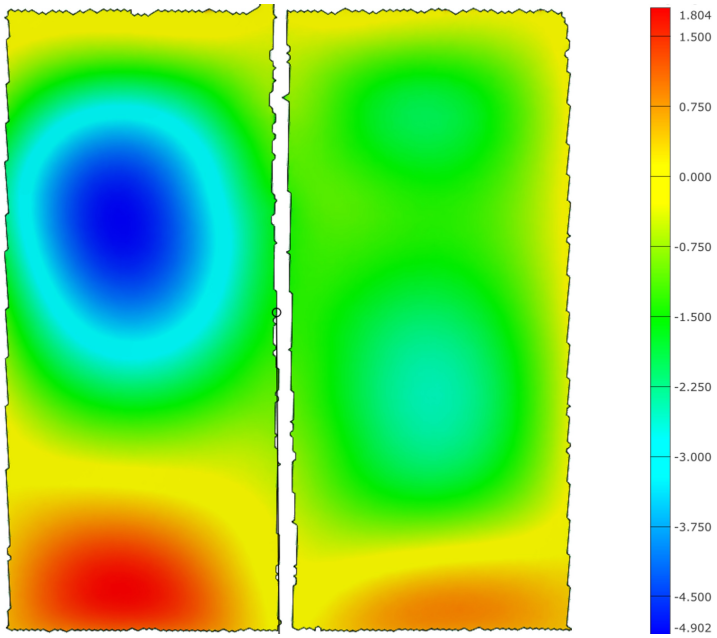

Figure 4.1: Buckling mode from DIC out-of-plane displacement results of the first experiment

Experimental results - experiment 2

For the second experiment, the maximum point load was measured at $1182\ kN$. The corresponding buckling mode at this critical load is shown in Figure 4.2, obtained from the DIC analysis. The figure illustrates the out-of-plane displacement field of the plate. Similar to the first experiment, the response is predominantly governed by local buckling. A prominent negative displacement region is again observed near the top-left corner of the plate. In contrast to the first test, however, a second distinct negative displacement region appears on the right side of the plate, positioned closer to its center. Two smaller positive displacement regions are present, one at the bottom-left corner and one at the top-right corner, but their magnitudes are notably smaller compared to the negative displacement regions.

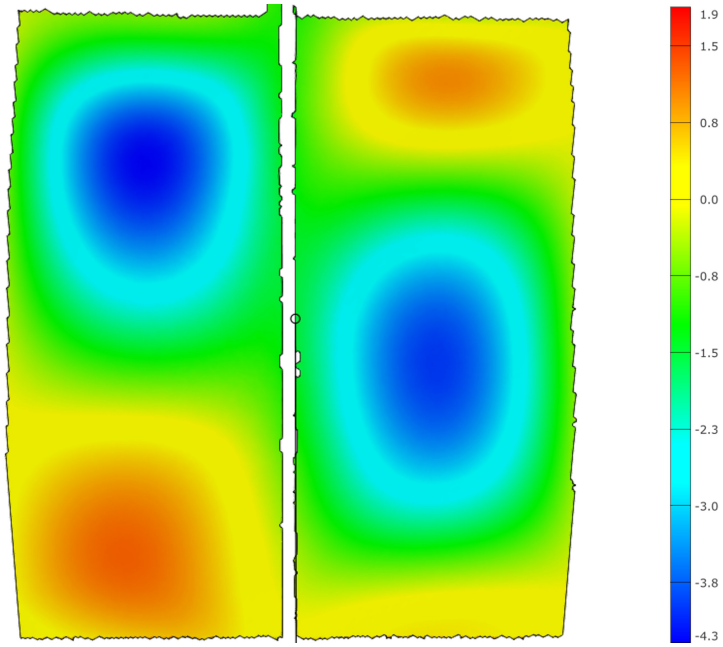

Figure 4.2: Buckling mode from DIC out-of-plane displacement results of the second experiment

Surprisingly, the buckling loads obtained from the two experiments differ by a substantial margin, de-

spite both stiffened plates being manufactured using the exact same method. While the observed variation in buckling modes could potentially be attributed to differences in geometric imperfections, it is unlikely that such imperfections alone account for the large discrepancy in the critical limit point. Instead, it is more likely that the difference arises from variations in the experimental setup between the two tests.

An obvious deviation from the intended experimental setup is observed at the vertical out-of-plane line constraint located on the left side of the plate. Inspection of the negative out-of-plane displacement field in this region reveals that, directly at the plate edge where the constraint is applied, relatively large negative displacements occur. This trend appears to extend beyond the range of the DIC measurements. A likely explanation for this observation is insufficient clamping of the plate within the setup, effectively reducing or even eliminating the constraint at this location. To investigate this hypothesis, the out-of-plane displacements along the constrained edge were extracted and plotted for comparison. Figure 4.3 presents these displacement profiles at the left constraint for both the first and second experiment, evaluated at a load of 990 kN.

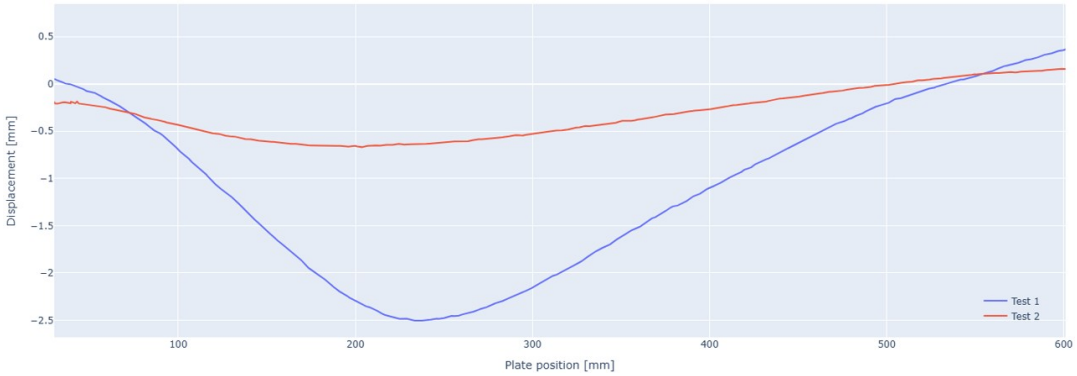

Figure 4.3: Buckling mode from DIC out-of-plane displacement results of the second experiment

In this figure, the profile from the first experiment is shown in blue, and that from the second experiment in red. The y-axis represents the out-of-plane displacement along the plate edge, while the x-axis corresponds to the position along this edge, ranging from 30 mm to 600 mm. Comparing the two experiments, a clear difference in behavior is observed: the first test exhibits a substantially larger maximum negative displacement of approximately -2.5 mm, whereas the second test reaches only slightly above -0.5 mm. It should be noted that some level of out-of-plane displacement at the measurement edge is unavoidable, as the DIC system cannot capture the full plate boundary. The visibility is limited by the physical obstruction of the setup, including the clamping system itself, which prevents measurements directly at the constraint line.

4.1.2. Plates with rectangular stiffeners

Analysis of the DIC results revealed that, as the applied uniaxial compression increased, the stiffener began to interact with the experimental setup. Specifically, it was observed that the stiffener was being pushed into the base plate, which restricts vertical movement of the plate. This interaction is illustrated in Figure 4.4, where the left image, captured directly from the DIC software, clearly shows the stiffener in contact with the base plate. The stiffener is oriented perpendicularly to the base plate, as can be visually confirmed in the figure. A similar interaction was observed at the top end of the plate, indicating that both ends of the stiffener were subject to vertical constraint due to contact with the setup.

To accurately capture this mechanical interaction in the numerical simulations, all subsequent FE models with the rectangular stiffeners implement a vertical constraint at both ends of the stiffener. This updated boundary condition is illustrated in the right image of Figure 4.4. For consistency with the coordinate system used throughout this research, the FE model image is rotated 90 degrees, as the DIC output is displayed horizontally in the figure.

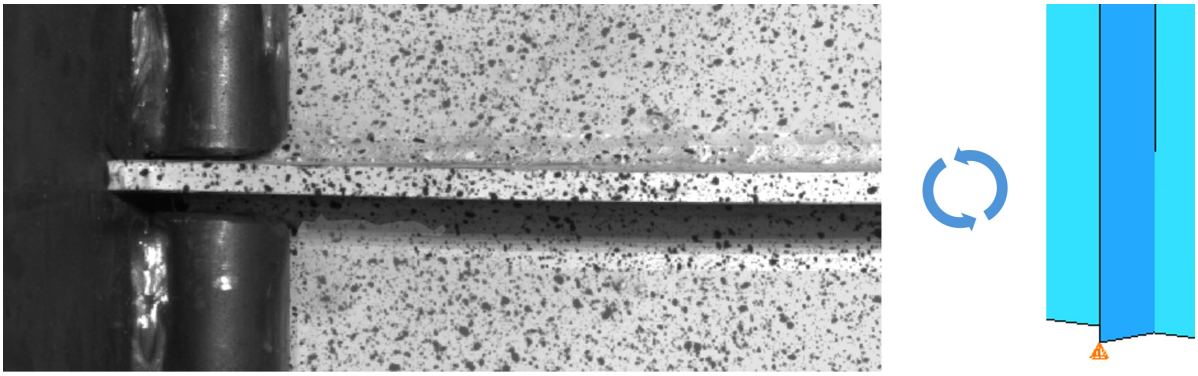

Figure 4.4: Interaction between stiffener and experimental setup (left), and the stiffener BC FE model (right)

Experimental results - experiment 3

The third experiment produced a maximum load within the same range as the second experiment, reaching a limit point of $1144kN$. The corresponding out-of-plane displacements at this load, shown in Figure4.5, illustrate the buckling mode of the plate. Despite exhibiting a similar buckling resistance to the second test, the third experiment revealed a considerably different buckling mode. In this case, the plate developed a highly symmetrical deformation pattern dominated by positive displacements, with three distinct positive and three distinct negative localized buckling regions.

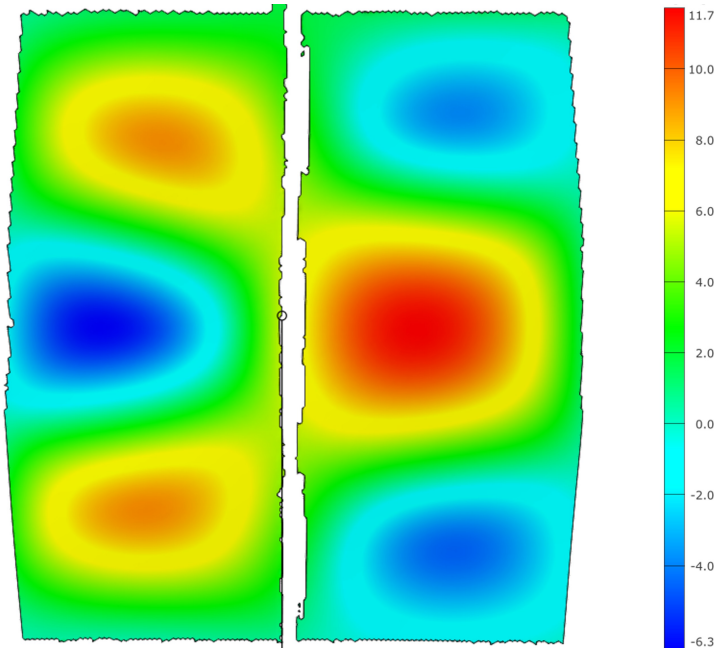

Figure 4.5: Buckling mode from DIC out-of-plane displacement results of the third experiment

Experimental results - experiment 4

The fourth and final experiment resulted in an almost identical buckling resistance to the third test, with a limit point of $1130kN$. The associated buckling mode, shown in Figure4.5, closely resembled that of the third experiment, featuring the same arrangement of three positive and three negative localized buckling regions. The only notable differences were a slight increase in the magnitude of the top-left positive displacement region and a slight decrease in the magnitude of the bottom-left positive displacement region.

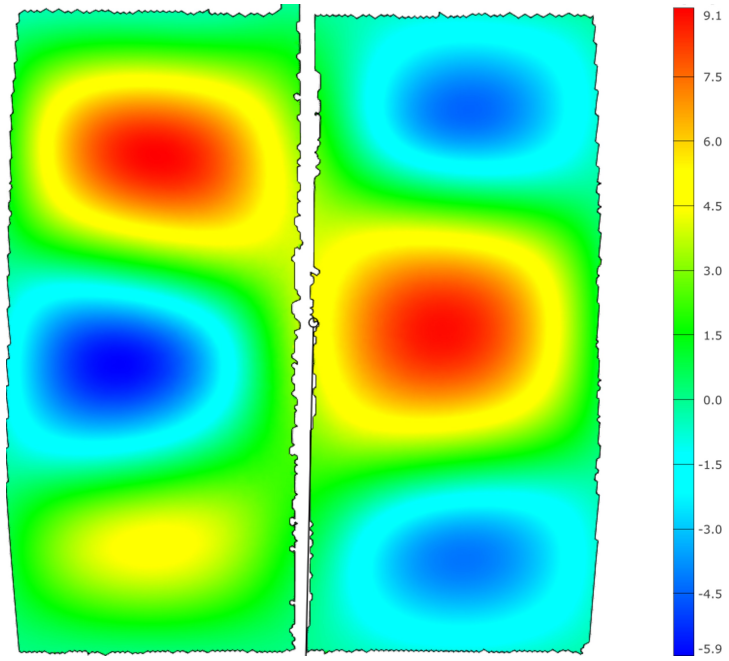

Figure 4.6: Buckling mode from DIC out-of-plane displacement results of the fourth experiment

Overall, the results of the third and fourth experiments are highly consistent, both in terms of buckling resistance and buckling mode. The small variations observed in the deformation patterns are most likely attributable to minor differences in geometric imperfections or subtle variations in the experimental setup.

4.2. Numerical validation

This section presents the numerical validation of the developed FE models. First, an overview of the numerical setup is provided, followed by the results for plates with WAAM stiffeners and plates with conventional rectangular stiffeners. Finally, the numerical predictions are compared against the experimental results to assess the accuracy and reliability of the models.

4.2.1. Overview of the numerical model

The numerical results presented in this section are derived from several sources. The majority originate from simulations conducted using the Abaqus/CAE solver, where nonlinear Riks analyses were performed to capture the stability behavior of the plates with high accuracy. Across all FE models, consistent modeling parameters are employed, such as boundary conditions, mesh types, and mesh densities, to ensure comparability between simulations.

Geometric imperfections of the plates have been incorporated into each model using the mesh grid imperfection interpolation methods. It was found that the implementation of both the geometry reconstruction method and the mesh grid-based interpolation method for the introduction of imperfections led to similar outcomes, independent of the chosen approach. Therefore, the final numerical results presented in this work are based on the latter method. Nevertheless, the imperfect stiffener geometries themselves were obtained through the geometry reconstruction approach. This was particularly relevant for the WAAM stiffeners, which exhibited substantial deviations from the intended design as a consequence of the manufacturing process. A more detailed discussion of the various imperfection implementation methods can be found in Section 3.2.5.

During the validation process, several aspects of the FE models were adjusted to improve agreement with the experimental results. Among these, the BC configuration was found to have the most significant impact on the numerical outcomes. In addition to the initially applied BC configuration described in Section 3.2.4, an alternative and promising configuration was identified. This new setup introduces a

rotational constraint in the X-direction, applied specifically to the top and bottom edges on the right side of the plate. Figure 4.7 illustrates this modification in more detail. It should be noted, however, that this configuration was discovered primarily through trial and error, and a clear physical explanation for its effectiveness has not yet been established. Nevertheless, for each experiment, a separate FE analysis was conducted using this alternative BC configuration to evaluate its influence on the results.

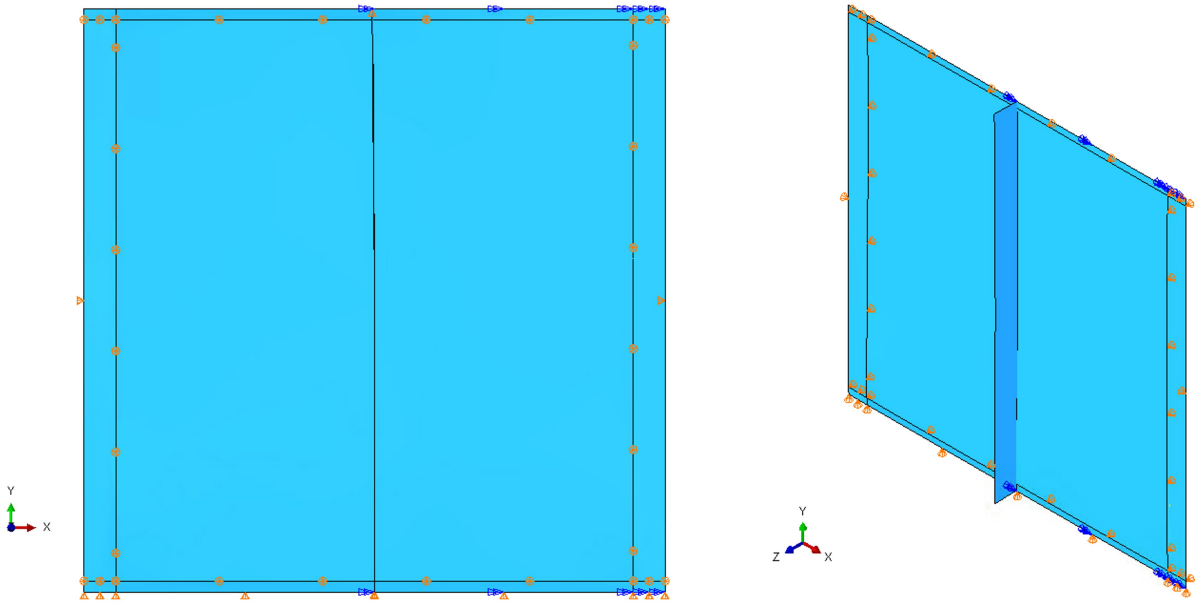

Figure 4.7: General BC configuration resembling the experimental setup, including the half rotational constraint

4.2.2. Plates with additive manufactured stiffeners

This subsection presents the numerical results obtained from the FE analyses of stiffened plates incorporating the WAAM-produced stiffener geometries. Two experimental tests were carried out using this WAAM geometry, and the numerical simulations were conducted to reflect each test setup. Accordingly, the subsection is structured into two parts, with each part focusing on one of the tests and its corresponding FE analysis results.

The plates equipped with the WAAM-produced stiffeners exhibited significantly less distortion during the welding process compared to those with traditional rectangular stiffeners. As a result, the residual stresses remaining in the plates after being pushed and aligned into the experimental setup were minimal. Due to the limited impact of these residual stresses, no additional FE models were developed to account for them in this section. This decision is further supported by the results presented later, which confirm that such residual effects do not significantly influence the structural behavior in this case.

4.2.2.1. Numerical results – experiment 1

As mentioned previously, two FE models were developed for the first experiment. One model used the original boundary condition configuration, while the other incorporated an additional rotational constraint applied to half of the top and bottom edges of the plate. The results discussed in this first part pertain to the first analysis, which was based on the original BC setup.

Upon completing the analysis, the plate exhibited a maximum LPF of 1.6129. This leads to the following calculated buckling resistance:

$$\begin{aligned} R_b &= \text{plate width} \cdot \text{LPF} \\ &= 750 \cdot 1.6129 = 1209.65 \text{ kN} \end{aligned}$$

The corresponding buckling mode is illustrated in Figure 4.8, which presents the out-of-plane displacements of the plate, specifically in the Z-direction (denoted by U3). In the figure, blue areas represent

displacements in the negative Z-direction, while red areas indicate displacements in the positive Z-direction.

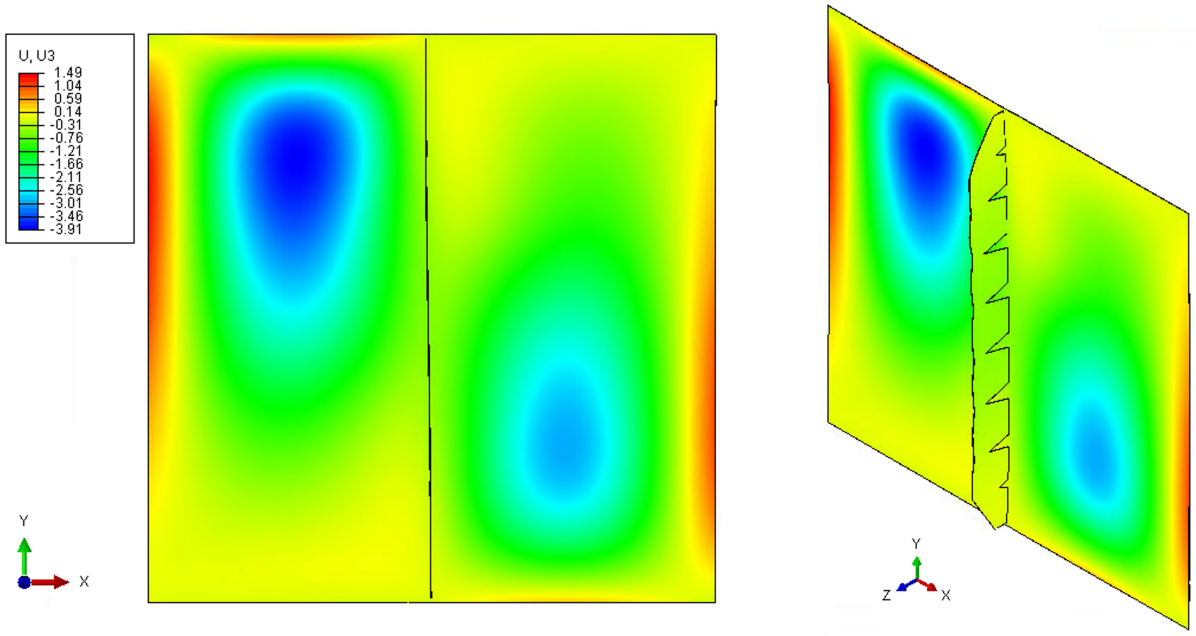

Figure 4.8: The buckling mode of the first test FE model, using the WAAM stiffener

Several observations can be made based on this deformation pattern. First, buckling occurs locally on both sides of the stiffener, which acts as a dividing element within the plate. On each side, the plate buckles in the opposite direction relative to the location of the stiffener. The maximum displacement is observed at the top-left corner of the plate, with a value of -3.91 mm. It is also observed that positive out-of-plane displacements occur along the free edges of the plate. This behavior is attributed to the deformation pattern resulting from the negative displacements within the constrained region; as the plate buckles inward near the stiffener, it causes outward (positive) displacements near the unconstrained, free edges.

Half rotational constraint

The second part of the numerical analysis for the first experiment was conducted using an alternative boundary condition in which a rotational constraint was applied to the right half of the top and bottom edges of the plate. Although the physical justification for this configuration is not entirely clear, it produced promising numerical results. Therefore, the analysis was included for the sake of completeness and comparison.

The same methodology as in the previous analysis was followed, resulting in a maximum LPF of 1.6031. The corresponding buckling resistance is calculated as follows:

$$R_b = 750 \cdot 1.6031 = 1202.31 \text{ kN}$$

While the difference in buckling resistance between the two boundary condition configurations is minimal, some variation can be observed in the corresponding buckling modes. Figure 4.9 illustrates the buckling mode shape of the model with the added rotational constraint. The general buckling pattern is comparable to that of the first configuration, particularly in terms of the locations of maximum out-of-plane displacements on either side of the stiffener. However, slight differences in the magnitude of 0.5 mm of these displacements are evident.

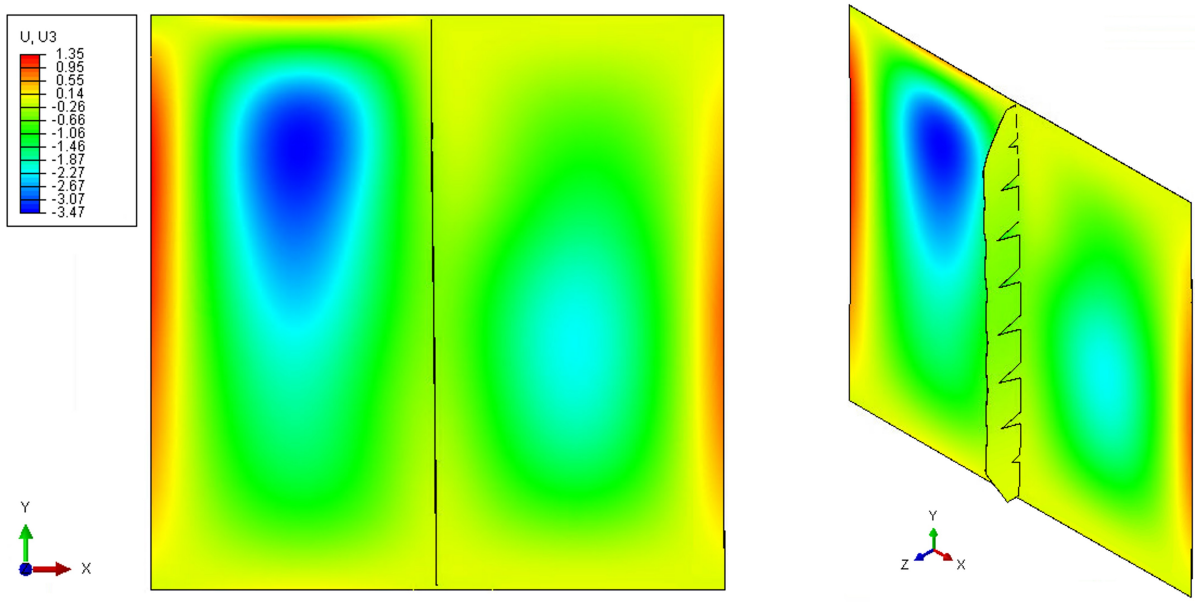

Figure 4.9: Buckling mode of the first test FE model, using the WAAM stiffener and the additional rotational constraint

4.2.2.2. Numerical results − experiment 2

As with the first experiment, two FE models were developed for the second experiment. The first model, discussed in this section, uses the original BC configuration without any rotational constraints.

The Riks analysis for this model yielded a peak LPF of 1.6332, resulting in a calculated buckling resistance of:

$$R_b = 750 \cdot 1.6332 = 1224.90 \text{ kN}$$

The corresponding buckling mode shape is presented in Figure 4.10. Compared to the first experiment, this analysis reveals several notable differences. Most significantly, positive out-of-plane displacements now occur within the constrained region of the plate, rather than only at the free edges as observed previously. Additionally, the free edges of the plate exhibit virtually no out-of-plane displacement in this case.

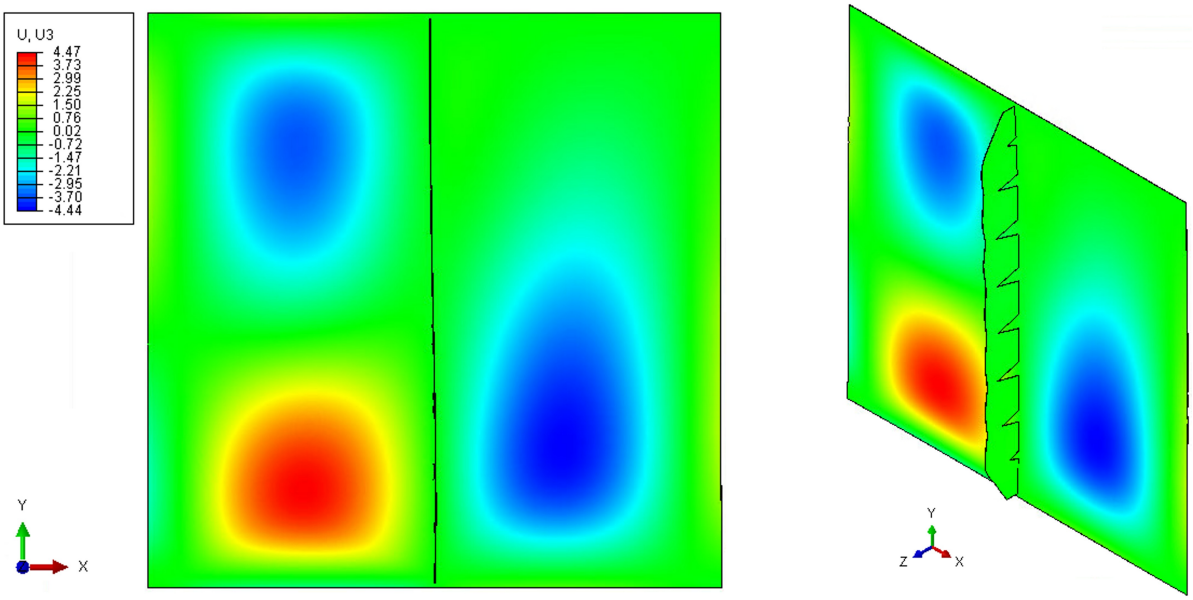

Figure 4.10: The buckling mode of the second test FE model, using the WAAM stiffener

These differences are attributed entirely to the variation in initial geometric imperfections between the two models, as all other parameters were kept identical. Another important observation is the shift in the location and magnitude of the maximum displacements. The maximum negative displacement is now located on the right side of the plate, reaching a value of −4.44 mm, while the maximum positive displacement is observed on the left side, with a value of 4.47 mm.

Half rotational constraint

The same methodology as in the previous analyses was applied to the FE model of the second experiment, this time incorporating the rotational constraint applied to the right half of the top and bottom edges of the plate. This analysis resulted in a maximum LPF of 1.6447, yielding the following buckling resistance:

$$R_b = 750 \cdot 1.6447 = 1233.53 \text{ kN}$$

Similar to the results from the first experiment, the differences in both buckling resistance and buckling mode shape compared to the unconstrained model are relatively small, as can be seen in Figure 4.11. However, a shift in the buckling pattern is observed. The local buckling region on the right side of the plate has moved slightly upward toward the center, and the overall magnitude of the out-of-plane displacements has decreased marginally by half a millimeter.

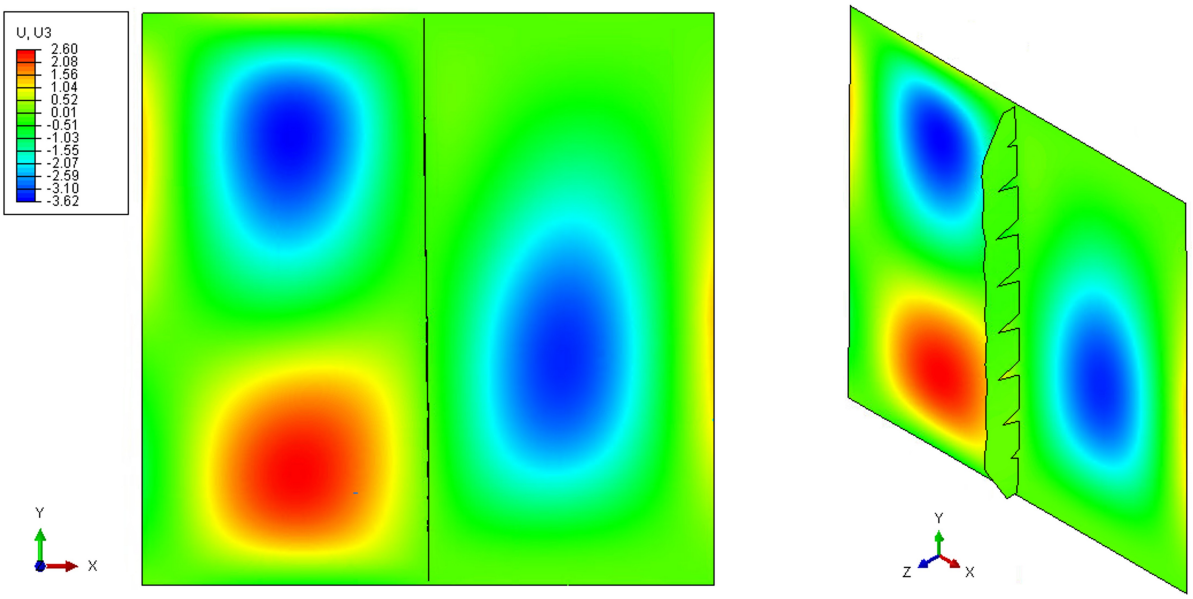

Figure 4.11: The buckling mode of the second test FE model, using the WAAM stiffener and a rotational constraint

4.2.3. Plates with rectangular stiffeners

This subsection presents the numerical results obtained from the FE analyses of stiffened plates incorporating traditional prismatic rectangular stiffener geometries. As with the previous experiments, two FE models were created for each test: one using the original BC configuration, and one including a rotational constraint applied to the right half of the top and bottom edges of the plate.

However, the plates with rectangular stiffeners were found to have significantly larger initial geometric imperfections. When these plates were pushed and aligned into the experimental setup, the interaction between these imperfections and the applied constraints led to substantial residual stresses. To further investigate the stability behavior under these conditions, two additional FE models were developed: one with the original BC configuration and one with the partial rotational constraint, explicitly incorporating the residual stress effects. As discussed in the Methodology chapter (See Section 3.2.6), two different approaches were employed together with the residual stresses implementation. In the first approach, the initial plate imperfections were derived from the BC displacements, which represent the deformations introduced by 'pushing' the plate into the setup. In the second approach, the initial imperfections were directly taken from the DIC measurements. The results showed that there was little to no difference between the two methods. Therefore, only the results from the first approach are presented in this section, while the results obtained using the residual stresses in combination with the DIC-based initial imperfections are provided in Appendix A.1. This resulted in a total of four FE models being analyzed for each of the two final experiments in this section.

4.2.3.1. Numerical results − experiment 3

As mentioned previously, four FE models were developed for the third and fourth experiments. Two of these models used the original BC configuration, while the other two included an additional rotational constraint applied to the right half of the top and bottom edges of the plate. Furthermore, for each BC configuration, models were created both with and without the implementation of residual stresses stemming from geometric imperfections. The results discussed in this first part pertain to the original BC configuration without the inclusion of residual stresses.

Following the analysis, the plate exhibited a maximum LPF of 1.5846, resulting in the following buckling resistance:

$$R_b = 750 \cdot 1.5846 = 1188.47 \text{ kN}$$

The corresponding buckling mode shape is shown in Figure 4.12. In contrast to the first two experiments involving the WAAM-produced stiffeners, which demonstrated predominantly local buckling behavior, this experiment displays characteristics of both global and local buckling. While the plate exhibits an overall global buckling mode, a localized buckling zone can be observed on the right side, where a higher out-of-plane displacement is concentrated.

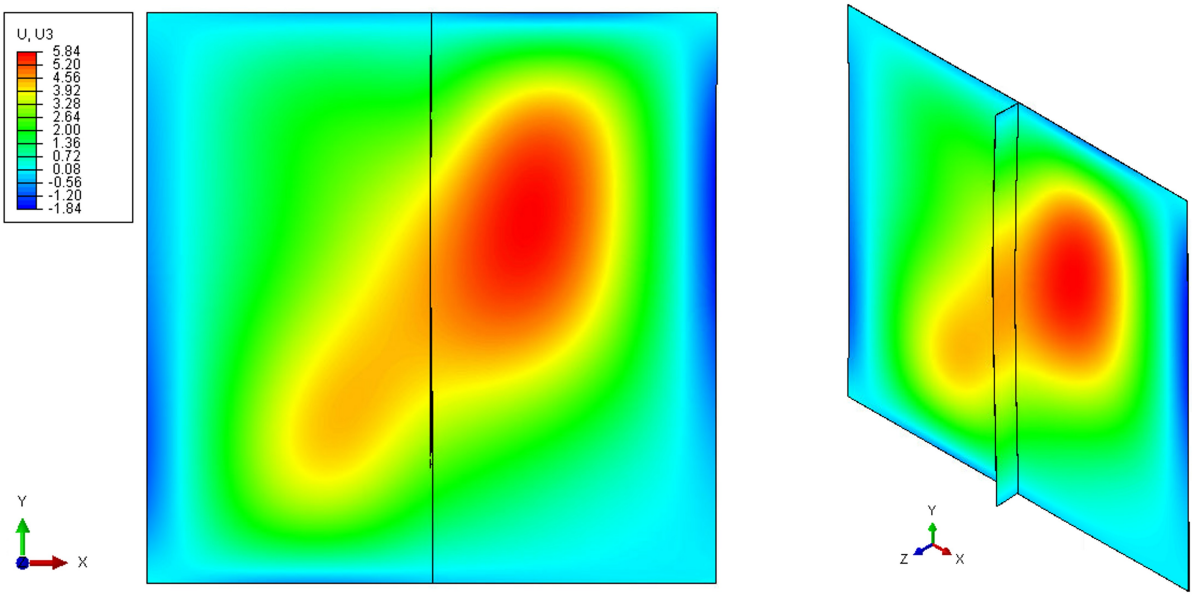

Figure 4.12: The buckling mode of the third test FE model, using the rectangular stiffener

Additionally, unlike the previous experiments, the plate in this case exhibits exclusively positive out-of-plane displacements within the constrained region. The only negative displacements are found at the free edges, and are likely induced by the deformation of the central part of the plate moving outward.

Half rotational constraint

Adding the rotational constraint to half of the top and bottom edges of the plate for the third experiment results in a maximum LPF of 1.5595, at which it reaches a buckling resistance of:

$$R_b = 750 \cdot 1.5595 = 1169.6 \text{ kN}$$

The addition of the rotational constraint resulted in a reduction in the buckling resistance of the stiffened plate. Unlike the experiments involving WAAM-produced stiffeners, where the effect of the rotational constraint on the buckling mode was minimal, this case exhibited a notable change in buckling behavior. As shown in Figure 4.13, the buckling mode now includes an additional local buckling region on the left side of the plate. While the overall deformation pattern still resembles global buckling, the presence of positive out-of-plane displacements on the left side introduces more pronounced local buckling characteristics. The maximum out-of-plane displacement has slightly decreased compared to the previous configuration, with a peak value of 4.65 mm.

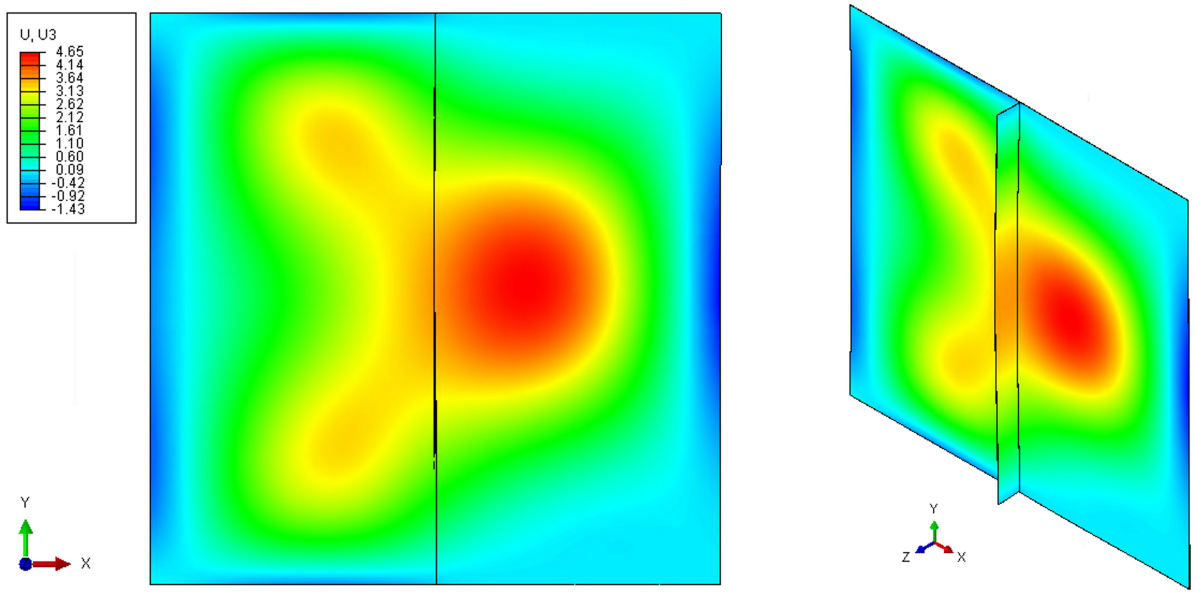

Figure 4.13: The buckling mode of the third test FE model, using the rectangular stiffener and a rotational constraint

Residual stress implementation

Significant distortions observed in the plates with rectangular stiffeners due to the welding process result in notable residual stresses once the plates are aligned and secured in the experimental setup. To obtain more accurate numerical results and to thoroughly investigate all relevant conditions for model validation, it is essential to account for these residual stresses. Incorporating them into the FE model led to a maximum LPF of 1.4443, corresponding to a buckling resistance of:

$$R_b = 750 \cdot 1.4443 = 1083.21 \text{ kN}$$

The resulting buckling mode, shown in Figure 4.14, is similar to that of the first FE model from the third experiment. The deformation pattern is primarily characterized by global buckling, with additional local buckling regions appearing on both sides of the stiffener. The presence of residual stresses amplifies these local effects: the local buckling zones are more clearly defined and exhibit higher out-of-plane displacements relative to the overall global deformation. This highlights the influence of residual stresses on both the mode shape and the plate's buckling behavior.

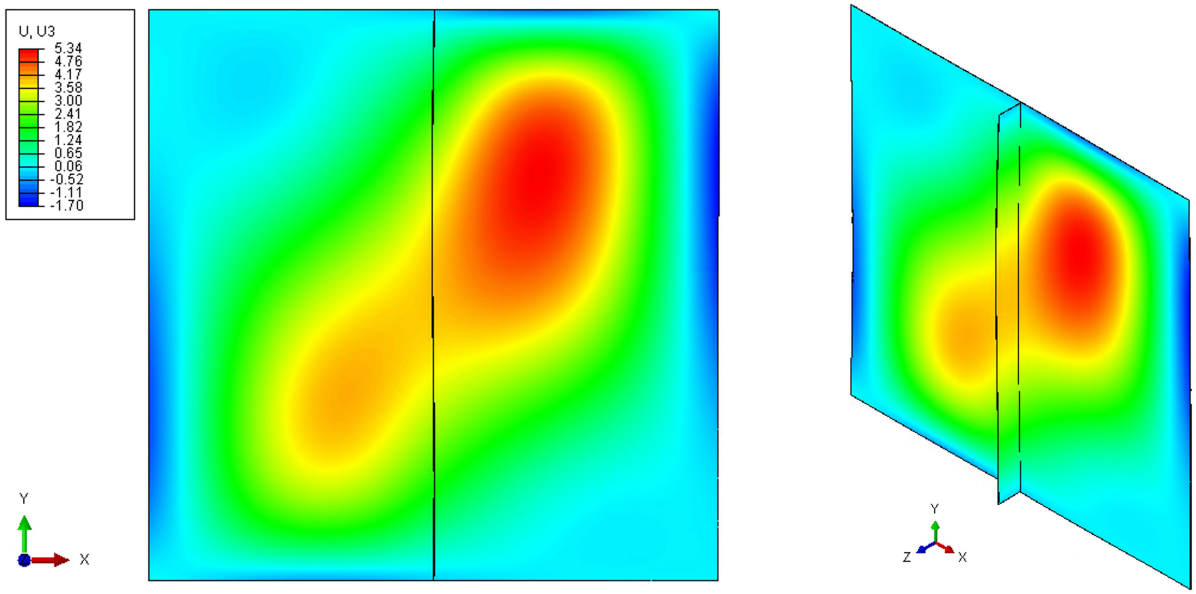

Figure 4.14: The buckling mode of the third test FE model, using the rectangular stiffener and implementing residual stresses

Residual stress implementation and half rotational constraint

In addition to incorporating the residual stresses caused by aligning the plate in the experimental setup, the modified boundary condition with the half rotational constraint was also applied. This combined configuration resulted in a maximum LPF of 1.6046, corresponding to a buckling resistance of:

$$R_b = 750 \cdot 1.6046 = 1203.44 \text{ kN}$$

The associated buckling mode shape is presented in Figure 4.15. Similar to the previous models, the dominant deformation mode remains global buckling. However, in contrast to the second FE model of the third experiment, the secondary local buckling region on the left side of the plate has largely disappeared. Additionally, compared to the other results from the third test, local buckling plays a significantly reduced role in this configuration. The response is now primarily governed by global plate behavior, indicating a stabilizing effect of the combined residual stress and boundary condition configuration.

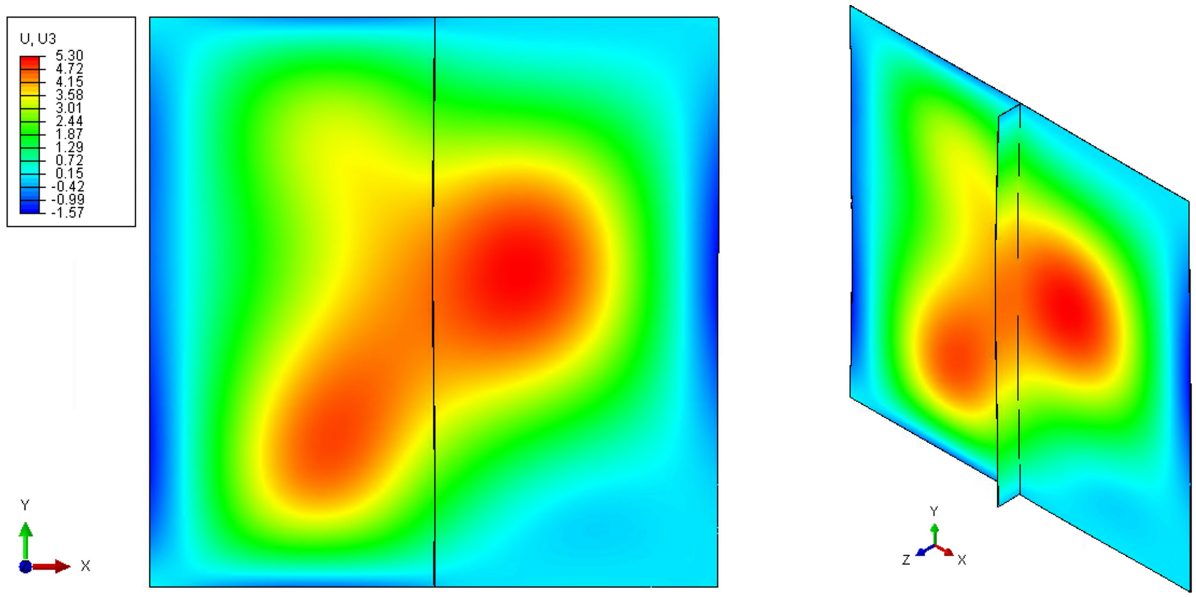

Figure 4.15: The buckling mode of the third test FE model, using the rectangular stiffener, a rotational constraint and implementing residual stresses

4.2.3.2. Numerical results – experiment 4

As with the third experiment, four FE models were developed for the fourth experiment. The first model, discussed in this section, utilizes the original boundary condition configuration, without any rotational constraints and without incorporating residual stresses resulting from aligning the plate in the experimental setup. The Riks analysis of this model produced a peak LPF of 1.598, corresponding to a calculated buckling resistance of:

$$R_b = 750 \cdot 1.598 = 1198.50 \text{ kN}$$

The associated buckling mode shape is shown in Figure 4.16. In contrast to all previously observed buckling responses, this mode exhibits minimal signs of local buckling. The plate predominantly undergoes global buckling, with only a slightly elevated region of positive out-of-plane displacement on the right side of the stiffener, though this effect remains minor. As a result of the dominant global buckling behavior, a higher overall out-of-plane displacement is observed, which is at 6.03 mm.

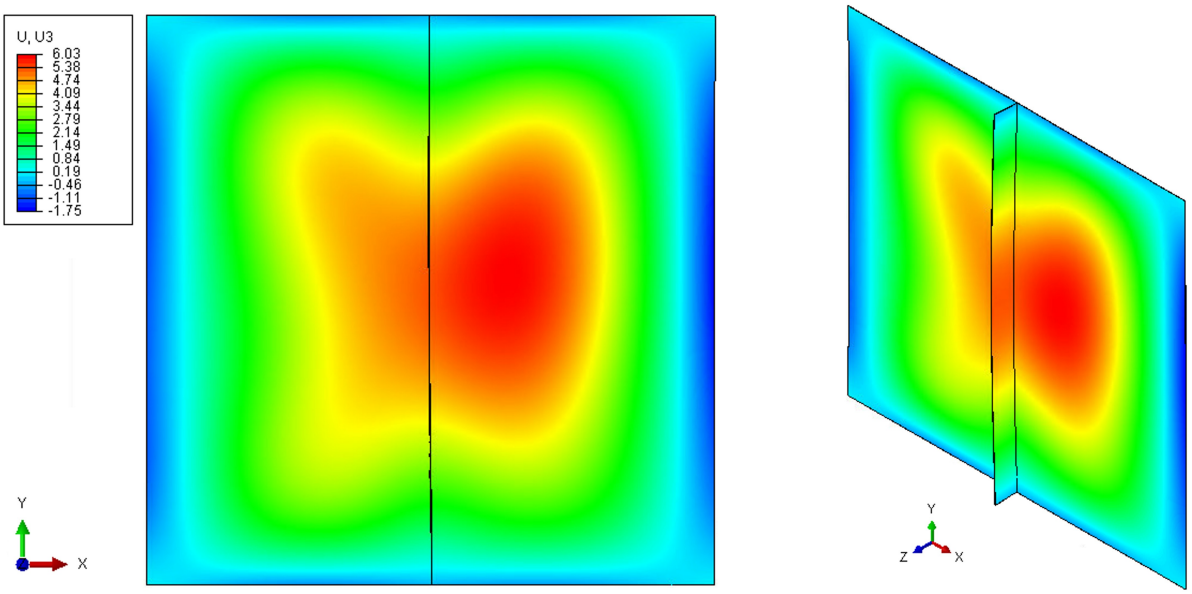

Figure 4.16: The buckling mode of the fourth test FE model, using the rectangular stiffener

Half rotational constraint

Applying the rotational constraint to half of the top and bottom edges of the plate in the fourth experiment resulted in a maximum LPF of 1.5967, corresponding to a buckling resistance of:

$$R_b = 750 \cdot 1.5967 = 1197.50 \text{ kN}$$

The out-of-plane displacements associated with this buckling resistance are presented in Figure 4.17, which illustrates the corresponding buckling mode. The deformation pattern resembles that observed in the third experiment with the same boundary condition configuration. However, this model exhibits relatively higher out-of-plane displacements in the localized buckling region near the top left part of the plate. Aside from this, the overall magnitude of out-of-plane displacements remains comparable to previous cases, with a peak positive displacement of 4.88 mm.

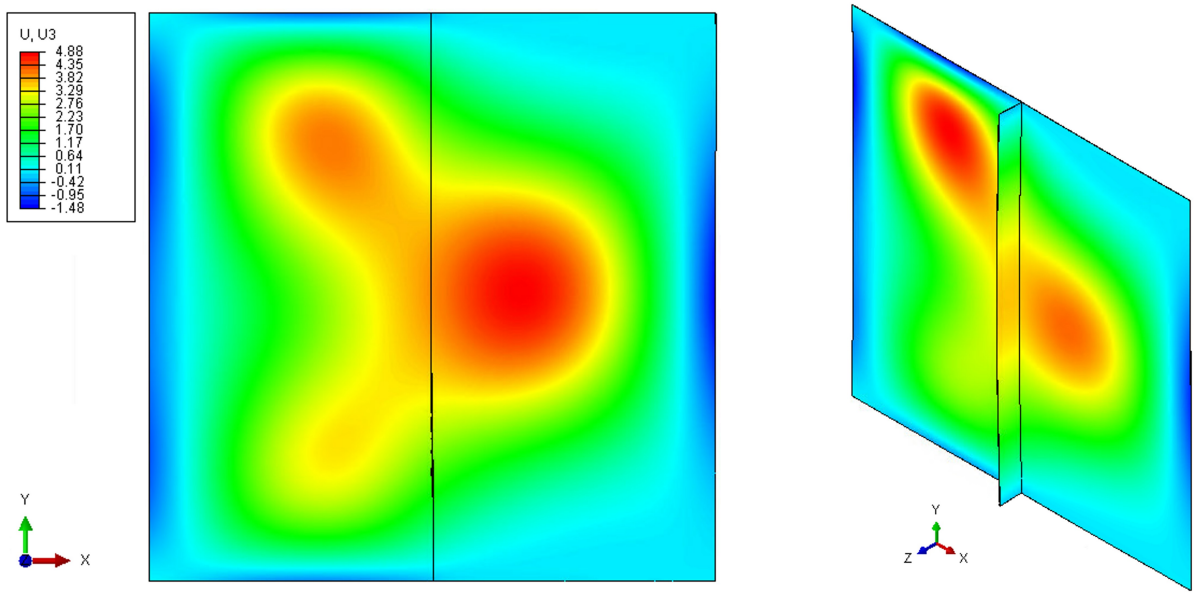

Figure 4.17: The buckling mode of the fourth test FE model, using the rectangular stiffener and a rotational constraint

Residual stress implementation

As with the third experiment, residual stresses were now also implemented to allow for a more detailed and realistic representation of the physical setup. The analysis resulted in a maximum LPF of 1.4327, corresponding to a buckling resistance of:

$$R_b = 750 \cdot 1.4327 = 1074.55 \text{ kN}$$

Once again, the inclusion of residual stresses led to a notable reduction in buckling resistance compared to the corresponding case without residual stresses, confirming their detrimental effect. The resulting buckling mode is shown in Figure 4.18. Unlike the third experiment, where the buckling modes with and without residual stresses were quite similar, this analysis reveals a clear difference. A pronounced localized buckling zone is observed on the right side of the plate, accompanied by a smaller localized deformation near the bottom left. The maximum positive out-of-plane displacement was found to be 4.86 mm.

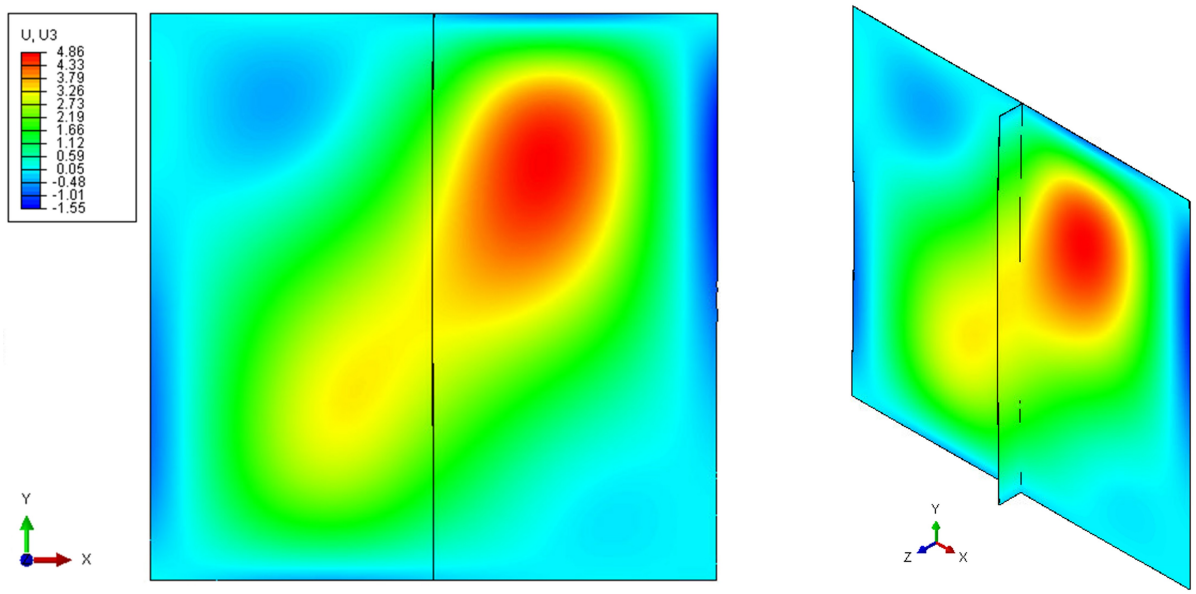

Figure 4.18: The buckling mode of the fourth test FE model, using the rectangular stiffener and implementing residual stresses

Residual stress implementation and half rotational constraint

For the final FE model analysis, both additional aspects were incorporated: the partial rotational constraint and the residual stresses induced by the boundary condition displacements. This model yielded a peak LPF of 1.6773, resulting in a calculated buckling resistance of:

$$R_b = 750 \cdot 1.6773 = 1257.98 \text{ kN}$$

Interestingly, the buckling resistance increases significantly when both effects are combined. While the residual stresses alone had previously reduced the resistance, the introduction of the partial rotational constraint appears to more than offset this reduction. The resulting buckling mode, shown in Figure 4.19, closely resembles that of the third experiment with the same FE configuration. The response is largely governed by global plate behavior, with comparable magnitudes of out-of-plane displacements.

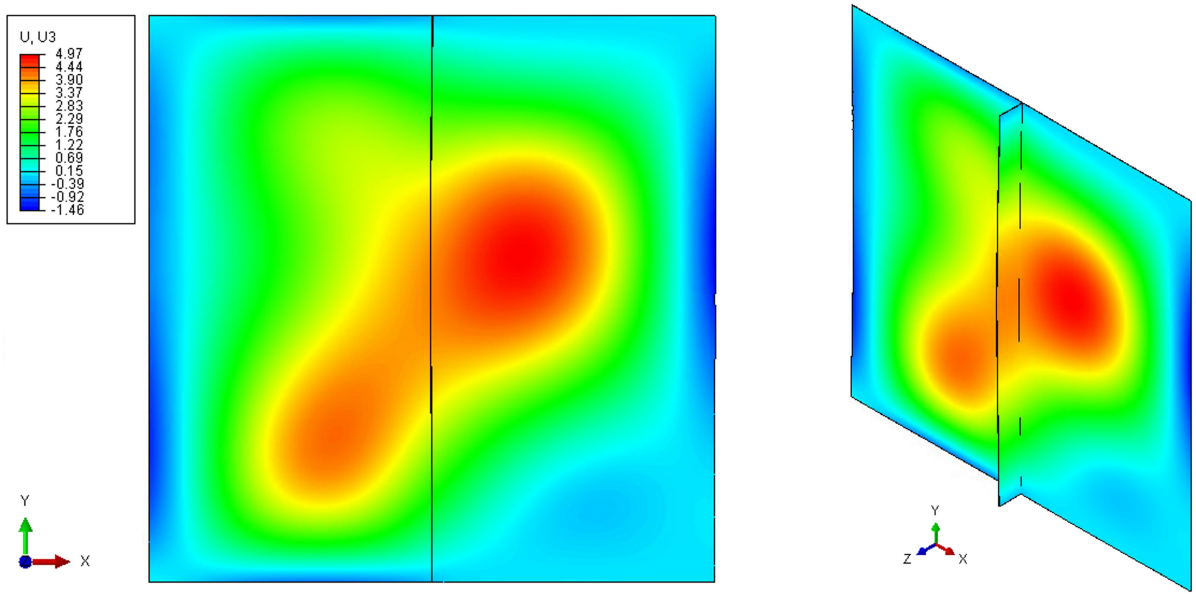

Figure 4.19: The buckling mode of the fourth test FE model, using the rectangular stiffener, a rotational constraint and implementing residual stresses

4.2.4. Numerical vs. experimental comparison

4.2.4.1. Experiment 1 - additive manufactured stiffener

Table 4.1 presents a visual comparison from experiment 1 between the experimentally measured buckling mode shapes using DIC and those predicted by the FE models. The top image shows the DIC results, while the bottom rows illustrate the FE simulations with and without rotational constraints.

Table 4.1: Comparison of out-of-plane displacements between DIC and FE model results at the buckling mode for experiment 1

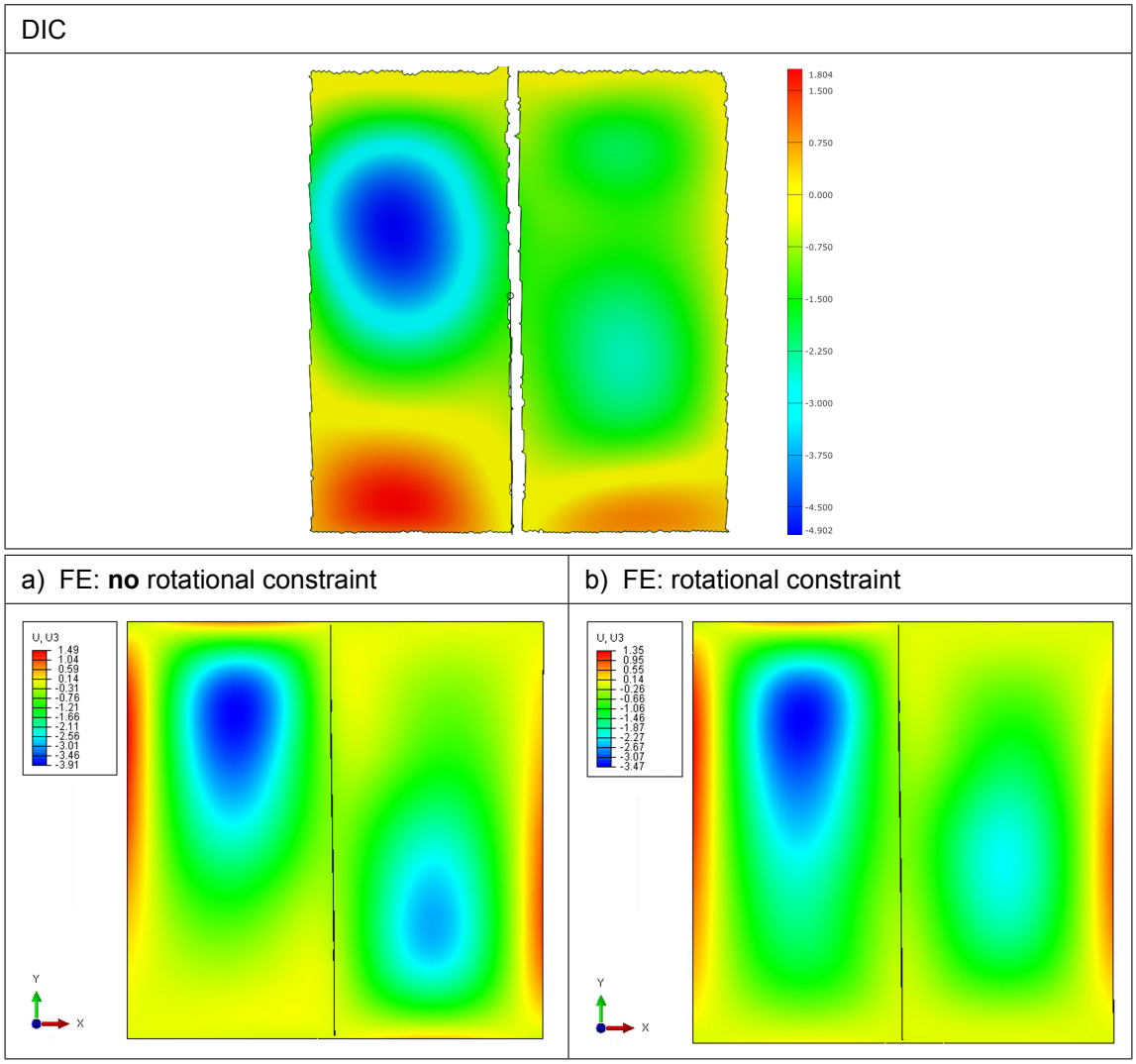

Matching buckling modes between the FE models and the experimental results is essential for validating the accuracy of the numerical model, ensuring reliable design predictions, and capturing critical behaviors such as mode interaction. For the first experiment, the general buckling shapes observed in both FE models, regardless of the presence of rotational constraints, closely resemble those captured by the DIC measurements. Both the experimental and numerical results exhibit distinct negative out-of-plane displacements in the top-left region of the plate. On the right-hand side, the buckling patterns also appear consistent across the DIC and FE results, particularly just below the center of the plate, where smaller negative displacements are observed in all cases.

One notable difference, however, is the presence of significant positive out-of-plane displacements at the bottom of the plate in the experimental results, which are absent in both FE models. A possible explanation for this deviation could be minor looseness in the experimental setup, specifically, a small amount of freedom at the base of the plate between its out-of-plane constraints. Despite this difference, the overall mode shape correlation between the FE simulations and the experimental observations is strong, especially in the upper and central regions of the plate.

To further assess the similarity in buckling behavior, a quantitative comparison of displacement magnitudes was performed. This involved extracting the out-of-plane displacements along the full height of the plate at specific lateral positions. These lines were taken at the center of both the left and right halves of the plate. The resulting displacement profiles, plotted with the out-of-plane displacement on the vertical axis and the corresponding height position on the plate (Y-axis) on the horizontal axis, are shown in Figure 4.20. Each plot contains three curves representing the DIC results and the two FE models. This comparison enables a more detailed evaluation of the local buckling response along the plate height.

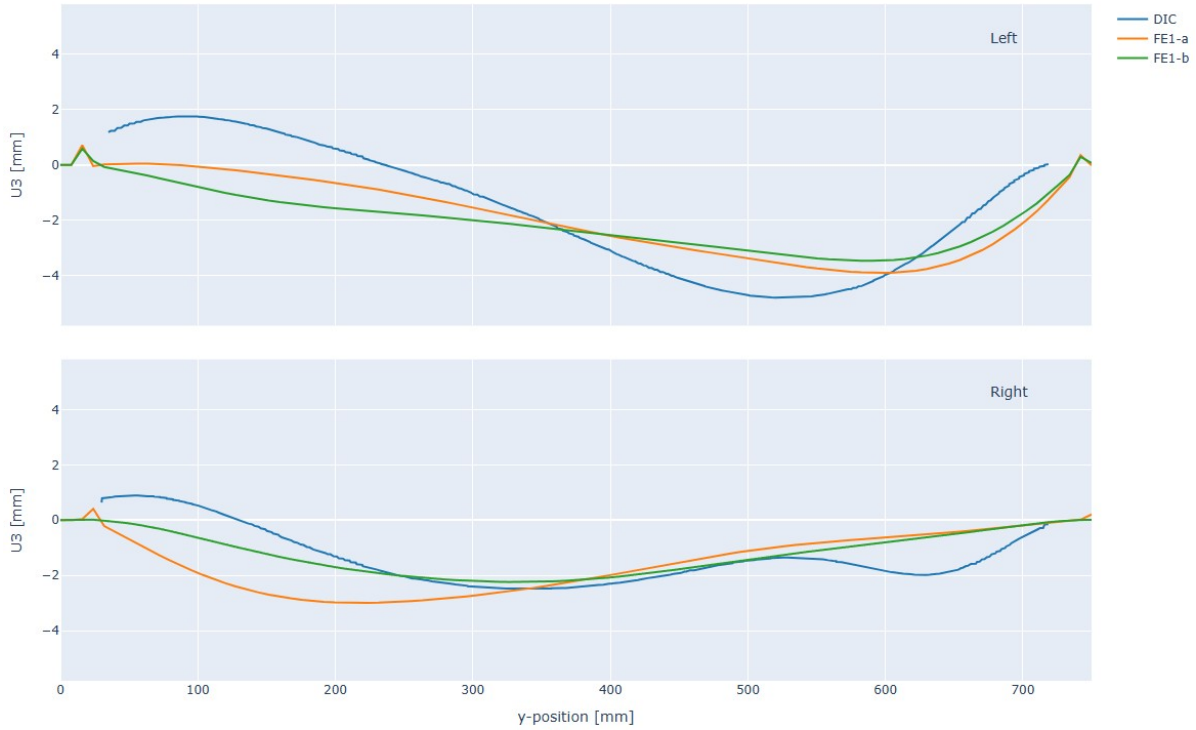

Figure 4.20: Out-of-plane displacement profiles plotted along the center lines of both the left and right sides of the plate for experiment 1

The figure presents two plots: the top plot corresponds to the left side of the plate, while the bottom plot represents the right side. A y-position of 0 is at the bottom of the plate, and $y = 750$ represents the top of the plate. The blue lines indicate the results obtained from the DIC measurements. On the left side of the plate, the out-of-plane displacement curves from the FE simulations generally follow a similar trend. However, when compared to the DIC results, a noticeable shift is observed in the Y-position of the negative displacement region. Additionally, the DIC data shows a distinct positive displacement region near the lower Y-positions, which is not captured by any of the FE models.

For the right side of the plate (bottom plot), the out-of-plane displacements are generally lower in magnitude compared to the left side. The DIC results reveal two small negative displacement peaks located around $y = 350\ mm$ and $y = 625\ mm$. In contrast, both FE simulations produce only a single negative displacement peak. In the case of FE1-a, the peak is located closer to the bottom of the plate, whereas in FE1-b, the peak aligns more closely with the second DIC peak around $y = 625\ mm$, and even shows comparable displacement magnitude. In summary, FE1-a demonstrates better agreement with the DIC data on the left side of the plate, while FE1-b provides a closer match on the right side.

An important aspect of the comparison between the numerical and experimental results is the evaluation of buckling resistance. Table 4.2 presents the buckling resistances obtained from both the experimental measurements and the FE simulations. In addition, the table includes the relative errors between each FE model and the corresponding DIC results, providing a quantitative measure of the model accuracy. In this context, FE1-a refers to the first finite element model, which does not incorporate any

rotational constraints (also see Figure *a* in Table 4.1). FE1-b, on the other hand, represents the second model, which includes rotational constraints at the top and bottom of the right half of the plate. This comparison allows for a direct assessment of the influence of boundary conditions on the predicted buckling resistance.

Table 4.2: Relative buckling resistance errors between the DIC results and the FE results of experiment 1

		DIC	FE1-a	FE1-b
R_b	[*kN*]	991	1210	1202
Error	[%]	-	22.1	21.3

The relative errors between the buckling resistances obtained from the DIC measurements and the FE models are approximately 20%. This indicates a significant deviation between the experimental and numerical results. The discrepancy is likely due to limitations in the experimental setup, particularly related to the boundary conditions, which may not have been perfectly replicated or controlled. While the FE models capture the overall buckling behavior well, differences in constraint conditions could explain the observed variation.

Lastly, to validate the FE models against the experimental results, the force–displacement graphs of both the DIC measurements and the FE simulations are compared. These graphs provide valuable insight into the global structural response and stiffness of the plate up to the point of buckling. By comparing the curves, it becomes possible to assess not only whether the FE models predict the correct buckling resistance, but also whether they capture the overall load–displacement behavior under increasing load. Figure 4.21 presents the force–displacement graphs for the first experiment.

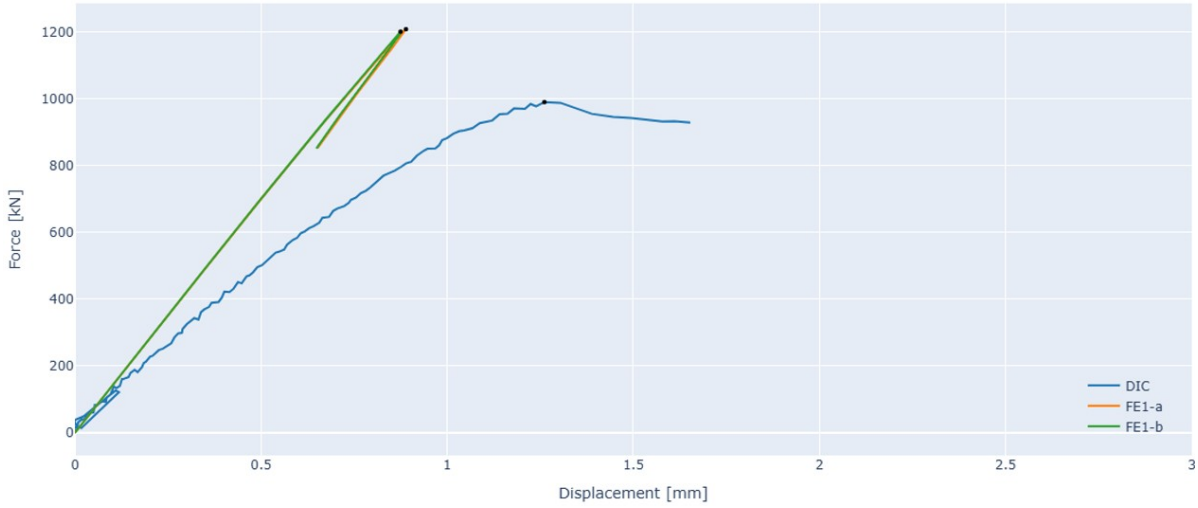

Figure 4.21: Force-displacement graphs of the DIC and FE model results from experiment 1

The blue line in the figure represents the force–displacement response of the first experiment, while the remaining curves correspond to the FE simulations. The vertical axis indicates the uniaxial compression force, applied as a point load, and the horizontal axis shows the vertical displacement measured at the top of the plate. Both FE models exhibit nearly identical force–displacement behavior. In contrast, notable differences are observed when comparing the FE results to the DIC-measured displacements from the experiment. The experimental results show a higher vertical displacement at the onset of buckling, but at a lower applied force. This suggests that the FE models predict a significantly stiffer response compared to the actual behavior of the tested plate.

Since the stability response of all FE models deviated significantly from the DIC measurements, a new FE model was developed in an attempt to improve the correlation. In this model, the experimentally

observed out-of-plane displacements at the left vertical constraint of the plate (as described in Section 4.1.1) were implemented directly as BC displacements. With this modification, the maximum buckling load was determined to be 1146 kN. Although this value is somewhat lower than in the previous FE models, it still remains far from the experimentally observed maximum load. The buckling mode shape of the updated FE model, which is presented in Appendix A.2, remained generally similar to that of the original models. In summary, the incorporation of the measured BC displacements led to a marginal reduction in the predicted buckling resistance, but the improvement is insufficient to reliably capture the experimental behavior.

4.2.4.2. Experiment 2 - additive manufactured stiffener

Table 4.3 presents a visual comparison from experiment 2 between the experimentally measured buckling mode shapes using DIC and those predicted by the FE models. The top image shows the DIC results, while the bottom rows illustrate the FE simulations with and without rotational constraints.

Table 4.3: Comparison of out-of-plane displacements between DIC and FE model results at the buckling mode for experiment 2

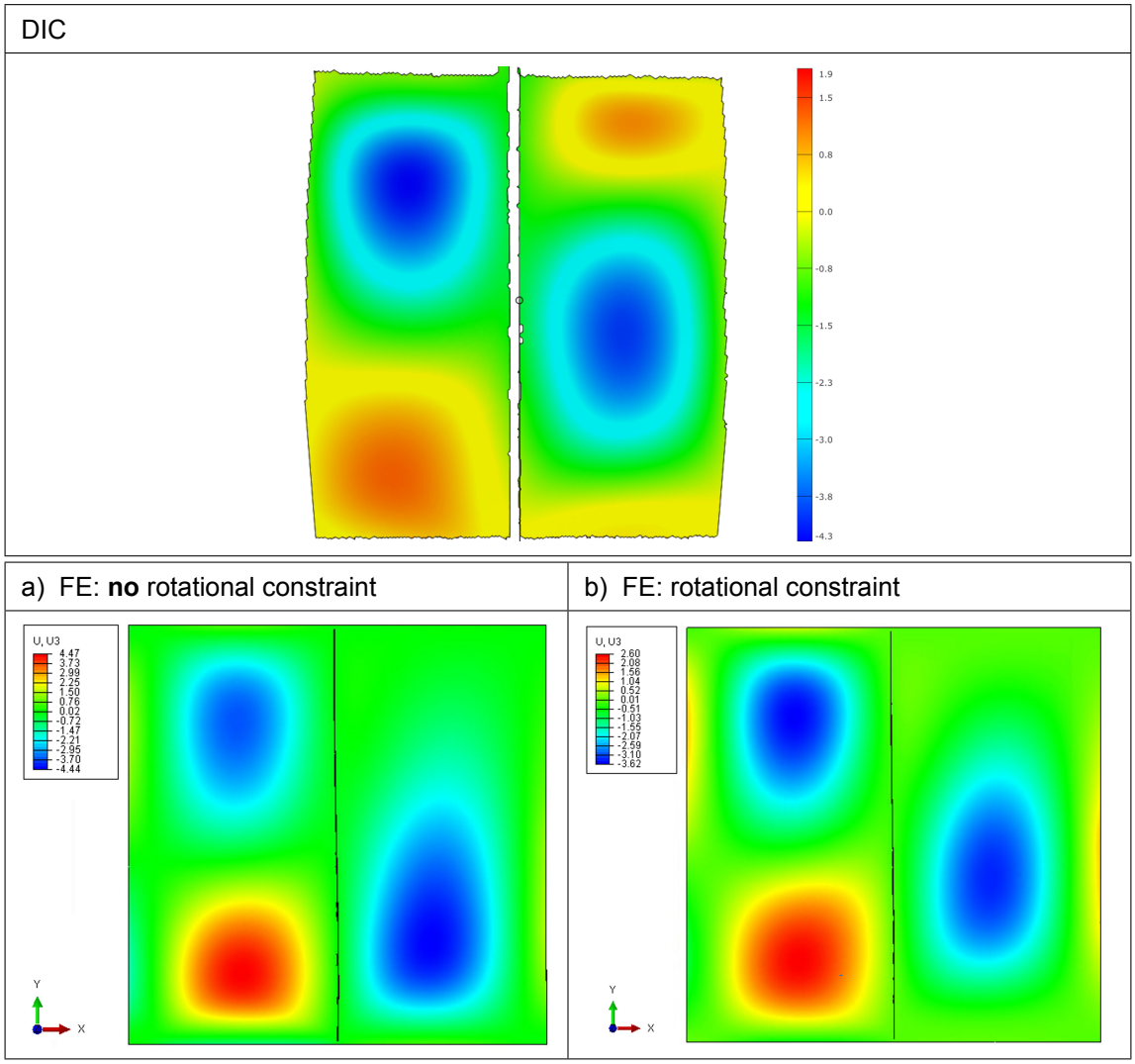

For the second experiment, the overall buckling patterns observed in both FE models, regardless of whether rotational constraints are applied, closely resemble those captured by the DIC measurements. In both the experimental and numerical results, a clear region of negative out-of-plane displacements appears in the top-left corner of the plate, accompanied by a region of positive displacements at the bottom left. On the right side of the plate, both the DIC and FE models display a distinct area of negative out-of-plane displacement, although its location appears slightly shifted downward in the FE simula-

tions. A notable difference is the presence of a small region with positive displacements in the DIC results, which is absent in both FE models. Overall, the FE models show strong agreement with the DIC measurements, particularly on the left side of the plate, while the right side exhibits slightly less accurate correspondence.

To further support the comparison between the DIC and FE results for the second experiment, out-of-plane displacement profiles are plotted along the center lines of both the left and right sides of the plate. Figure 4.22 presents these two plots, each containing three curves: one from the DIC measurements and one from each FE model. These plots offer a more detailed, quantitative comparison of the displacement behavior across the key regions of the plate.

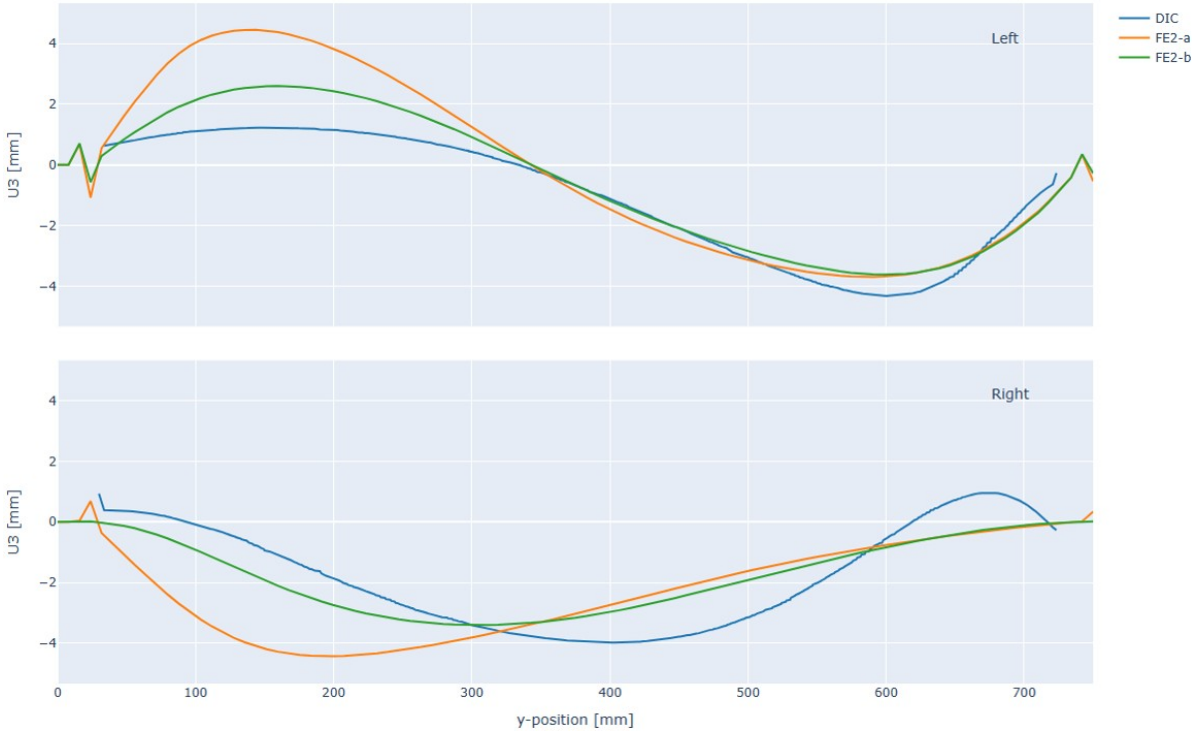

Figure 4.22: Out-of-plane displacement profiles plotted along the center lines of both the left and right sides of the plate for experiment 2

For the left side of the plate, two distinct peaks are observed in the DIC results: a positive displacement peak around $y = 150\ mm$, and a negative peak near $y = 600\ mm$. Both FE models capture these peak locations accurately, with differences primarily in the displacement magnitudes. FE2-b shows slightly better agreement with the DIC for the positive peak in terms of magnitude, while for the negative peak, both FE models perform similarly and produce nearly identical displacement values. Overall, both FE models closely resemble the DIC measurements for the left side of the plate, with FE2-b demonstrating a marginally better match.

For the right side of the plate, the DIC data again shows a positive and a negative displacement peak, although their positions are reversed compared to the left side. The negative peak appears around $y = 400\ mm$, while the positive peak is located near $y = 675\ mm$. The FE models, however, only display a single negative peak, both located roughly around $y = 200\ mm$ and $y = 300\ mm$. While the negative displacement magnitudes in the FE models are comparable to those in the DIC results, the y-locations do not align, with FE2-b however getting relatively close. Additionally, neither FE model captures the positive peak present in the DIC data. In summary, while the displacement magnitudes are reasonably accurate, the spatial distribution of the displacement in the FE models does not correspond well with the DIC measurements for the right side of the plate.

Table 4.4 summarizes the buckling resistances obtained from the second experiment, including both the experimental results from the DIC measurements and the numerical predictions from the FE simulations.

The table also lists the relative errors between each FE model and the corresponding DIC results. As before, FE2-a refers to the first FE model without rotational constraints, while FE2-b corresponds to the model that includes rotational constraints at the top and bottom right sides of the plate.

Table 4.4: Relative buckling resistance errors between the DIC results and the FE results of experiment 2

		DIC	FE2-a	FE2-b
R_b	[*kN*]	1182	1225	1234
Error	[%]	-	3.6	4.4

Compared to the buckling resistance errors of the first experiment, the second experiment shows a notable improvement in relative error. Both FE simulations exhibit a relative error of approximately 4%, indicating a strong agreement with the experimental results in terms of buckling resistance. This small discrepancy suggests that the FE models are accurately capturing the maximum load the structure can resist before buckling occurs. It also reflects a solid validation of the modeling assumptions, boundary conditions, and material properties used in the numerical setup.

To further validate the FE models against the experimental results, the force–displacement graphs of both the DIC measurements and the FE simulations are compared. These graphs provide valuable insight into the overall stiffness and structural response of the plate under increasing load. Figure 4.23 presents the force–displacement graphs for the second experiment, enabling a direct comparison of the load–displacement behavior across the different cases.

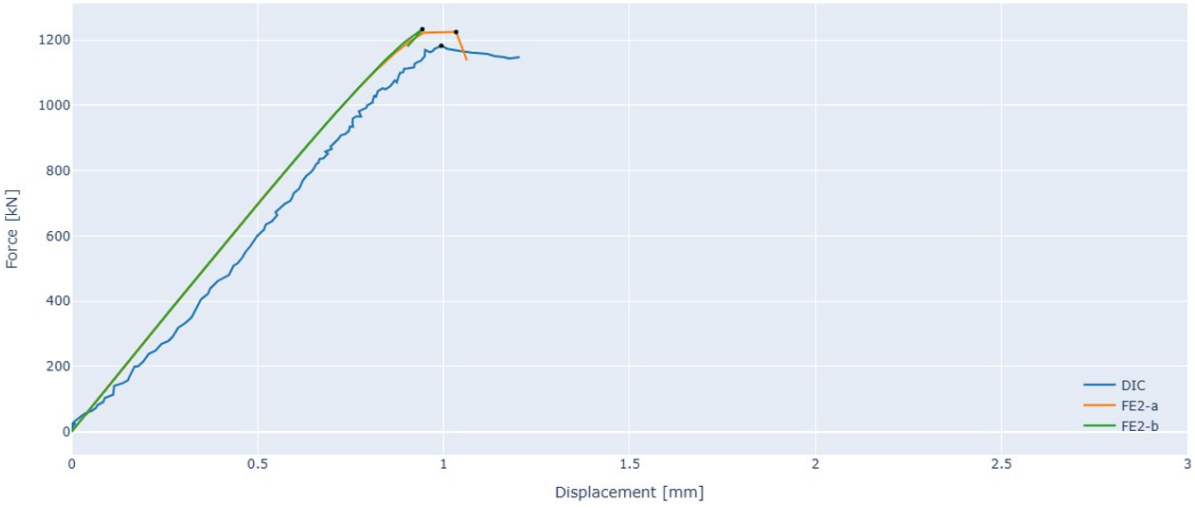

Figure 4.23: Force-displacement graphs of the DIC and FE model results from experiment 2

Similar to the first experiment, the force–displacement curves of the FE models are nearly identical, with only a slight variation in the total vertical displacement at the buckling point. When compared to the displacements obtained from the DIC measurements, the FE simulations produce closely matching curves. Both the DIC results and the FE simulations exhibit the same slope in the force–displacement relationship, indicating that the stiffness of the plate is consistent between the experiment and the numerical models. The difference in total vertical displacement at the point of buckling is minimal, with all values being approximately 1 mm.

4.2.4.3. Experiment 3 - rectangular stiffener

Table 4.5 presents a visual comparison from experiment 3 between the experimentally measured buckling mode shapes using DIC and those predicted by the FE models. The top image shows the DIC results, while the bottom rows illustrate the FE simulations with and without rotational constraints and residual stress effects.

Table 4.5: Comparison of out-of-plane displacements between DIC and FE model results at the buckling mode for experiment 3

DIC
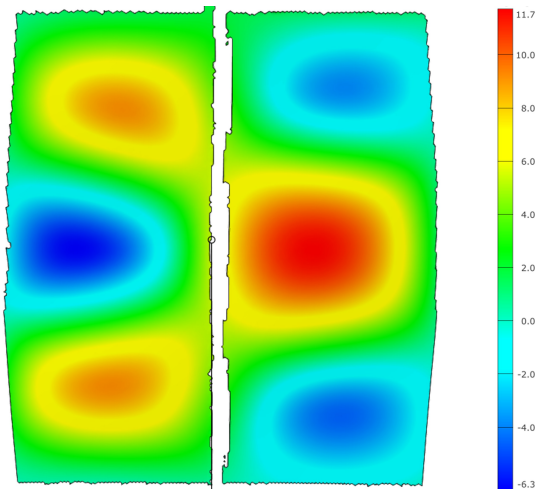
a) FE: **no** rotational constraint
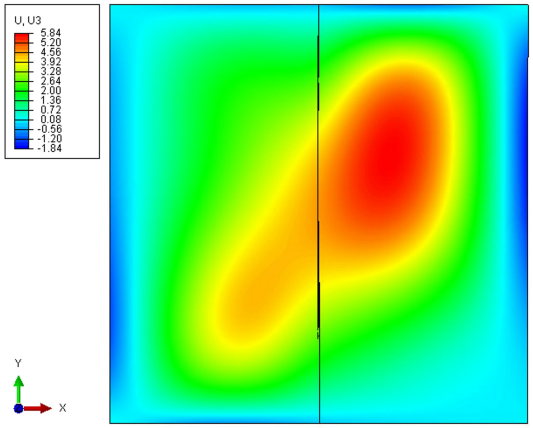
b) FE: rotational constraint
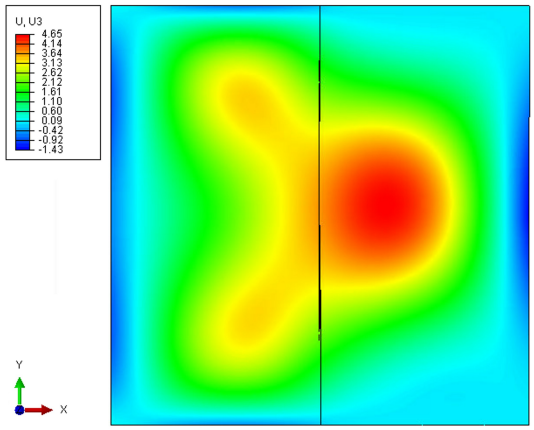
c) FE: residual stress + **no** rotational constraint
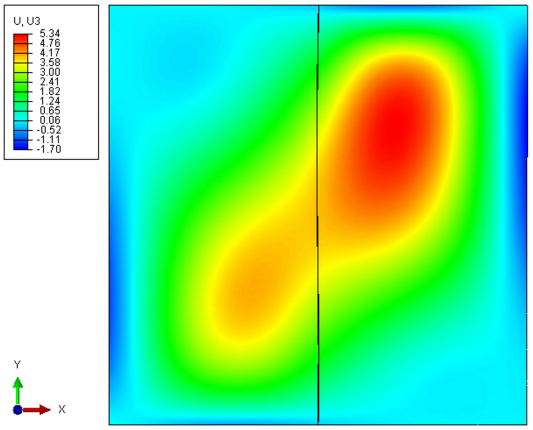
d) FE: residual stress + rotational constraint
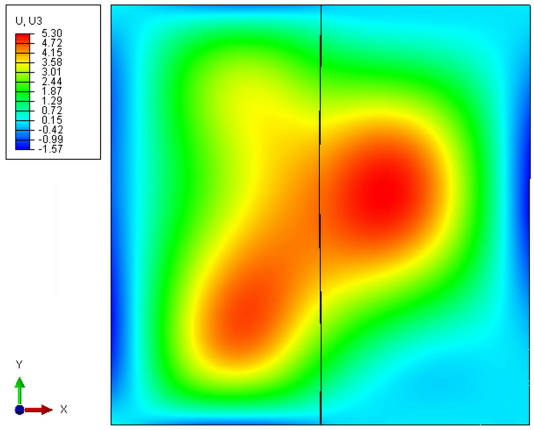

The third experiment includes two additional FE models, this time incorporating the effect of residual stresses. These residual stresses arise from the deformation introduced when the distorted plates are manually pushed into the experimental setup. Depending on their nature, these stresses can have either favorable or unfavorable effects on the validation process. However, before considering these

models, the two FE simulations without residual stresses are first examined. In contrast to the previous experiments, these two models exhibit significantly different buckling modes.

The contour plot of the first model (Figure 4.5-a), which includes no rotational constraints and no residual stresses, reveals a buckling shape that deviates notably from the DIC results. While both show a positive out-of-plane displacement hotspot near the center-right and another smaller one on the bottom left, the rest of the deformation pattern differs. Notably, the DIC results display negative out-of-plane displacements in some areas, which are absent in this FE simulation.

The second FE model (Figure 4.5-b), which also excludes residual stresses but applies a rotational constraint to the top and bottom of the right plate edge, shows improved agreement with the DIC results. It captures the general symmetrical pattern of positive Z-displacements observed in the experiment. However, the negative displacements present in the DIC data are still missing from the simulation.

The comparison then shifts to the FE models that include residual stresses. The third model (Figure 4.5-c), which applies residual stresses but no rotational constraint, produces a buckling mode similar to the first model. While the inclusion of residual stresses slightly alters the deformation shape, the overall match with the DIC results does not significantly improve.

The fourth and final FE model (Figure 4.5-d) includes both residual stresses and the partial rotational constraint. Compared to the second model, the buckling behavior shifts slightly due to the added stresses. This simulation still shares some similarities with the DIC results in terms of positive displacement locations, but the overall response remains more globally dominated, whereas the DIC data clearly indicates localized buckling.

As with the previous experiments, out-of-plane displacement profiles are extracted along the vertical center lines of both the left and right sides of the plate. Figure 4.24 presents these plots, showing five curves: one from the DIC measurements and one from each FE simulation. These profiles provide a more detailed quantitative comparison of the deformation patterns, offering further insight into how well each model captures the local buckling behavior observed experimentally.

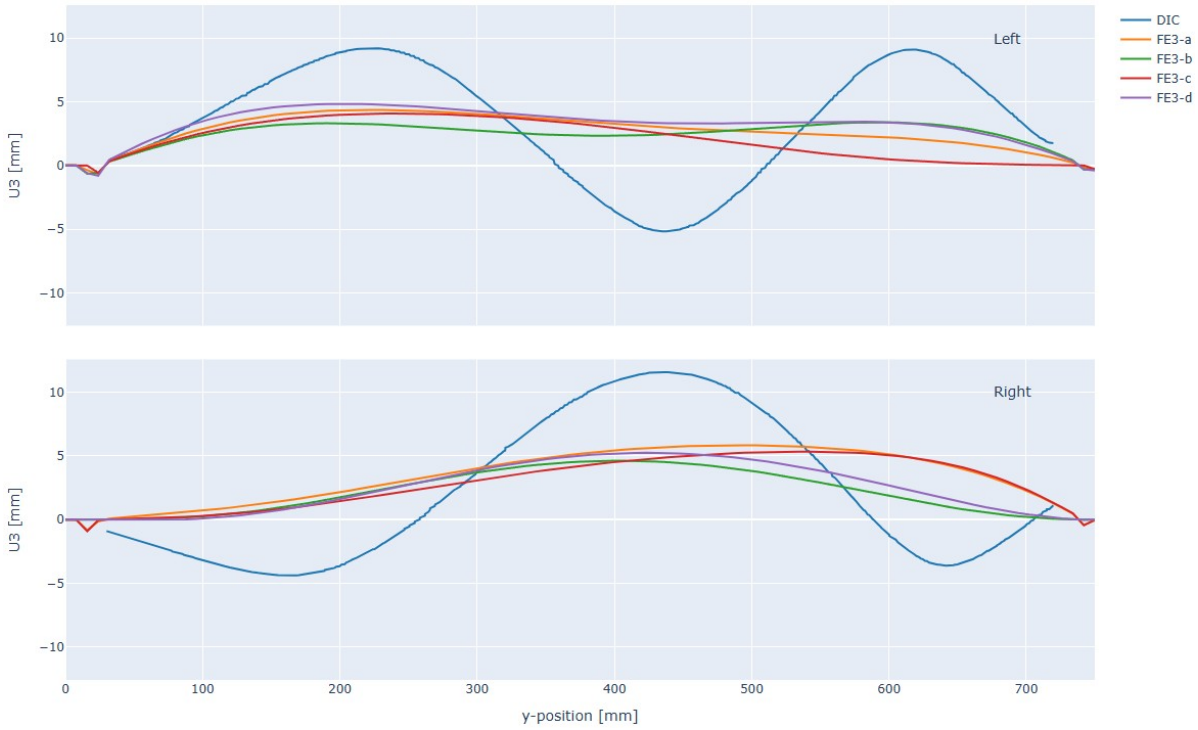

Figure 4.24: Out-of-plane displacement profiles plotted along the center lines of both the left and right sides of the plate for experiment 3

For the left side of the plate, three distinct displacement peaks are observed in the DIC results: two positive and one negative. In contrast, none of the FE models reproduce these clear peak patterns. All FE models exhibit only positive displacements, with the FE3-b model being the only one that somewhat

clearly shows two positive displacement peaks. Notably, these peaks occur at approximately the same locations along the center line of the plate as in the DIC results, around $y = 200\ mm$ and $y = 600\ mm$. However, the displacement magnitudes predicted by the FE3-b model differ substantially from those measured by the DIC.

On the right side of the plate, three displacement peaks are identified in the DIC data: two negative and one positive. While all FE models tend to show a single positive displacement peak, the FE3-a and FE3-c models predict this peak at different y-positions than those observed in the DIC results. The other two models do capture a positive displacement peak at approximately $y = 425\ mm$, consistent with the DIC. Nevertheless, as was the case on the left side, the predicted displacement magnitudes differ significantly from the experimental DIC measurements.

Table 4.6 summarizes the buckling resistances and corresponding relative errors for all FE models in the third experiment.

Table 4.6: Relative buckling resistance errors between the DIC results and the FE results of experiment 3

		DIC	FE3-a	FE3-b	FE3-c	FE3-d
R_b	[*kN*]	1144	1188	1170	1083	1203
Error	[%]	-	3.9	2.2	-5.3	5.2

The first two simulations (FE3-a and FE3-b), which do not include residual stresses, show very low relative errors—both under 5%—indicating a slight overestimation of the buckling resistance compared to the experimental DIC results. When residual stresses are introduced without rotational constraints (FE3-c), the relative error becomes negative (approximately -5%), suggesting that the added residual stresses have an unfavorable impact on the buckling resistance prediction. Interestingly, when a rotational constraint is added to this model (FE3-d), the relative error becomes positive again, rising to around +5%. This shift implies that the rotational constraint helps compensate for the influence of the residual stresses. Despite the variation, all absolute relative errors remain around or below 5%, which is generally considered acceptable for validation purposes in terms of buckling resistance.

The final step in the validation process of the third experiment involves analyzing the force–displacement behavior of both the DIC measurements and the numerical simulations. Figure 4.25 presents the force–displacement curves for all four FE models alongside the experimental data, allowing a direct comparison of structural response.

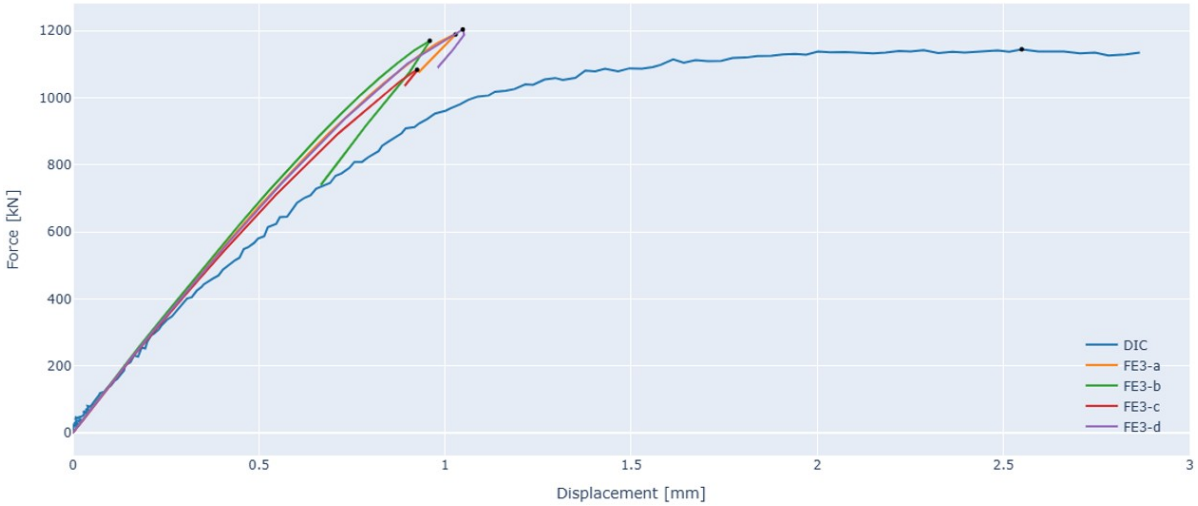

Figure 4.25: Force-displacement graphs of the DIC and FE model results from experiment 3

All FE models produce similar force–displacement responses, with each simulation reaching a vertical

displacement of approximately $1\ mm$. In all cases, the FE results display a stable behavior in which the force increases almost linearly with displacement up to the bifurcation point. Beyond this point, the displacement drops abruptly while the applied force decreases, indicating the onset of buckling. In contrast, the DIC results show little to no linear behavior. Instead, the experimental curve reaches a plateau, ultimately achieving a significantly higher maximum force at a vertical displacement exceeding $2.5\ mm$.

4.2.4.4. Experiment 4 - rectangular stiffener

Table 4.7 presents a visual comparison from experiment 4 between the experimentally measured buckling mode shapes using DIC and those predicted by the FE models. The top image shows the DIC results, while the bottom rows illustrate the FE simulations with and without rotational constraints and residual stress effects.

Table 4.7: Comparison of out-of-plane displacements between DIC and FE model results at the buckling mode for experiment 4

DIC	
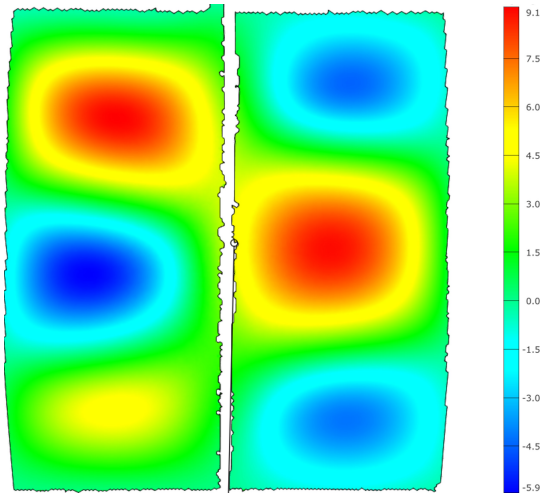	
a) FE: **no** rotational constraint	b) FE: rotational constraint
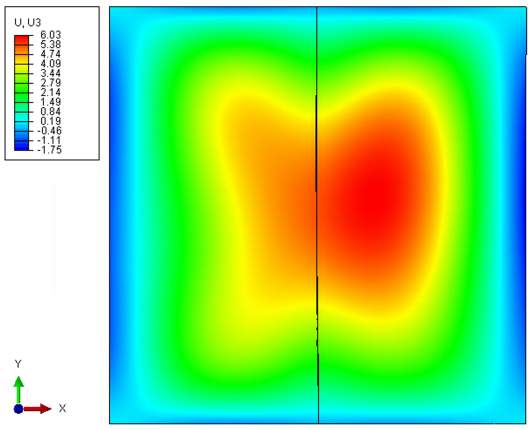	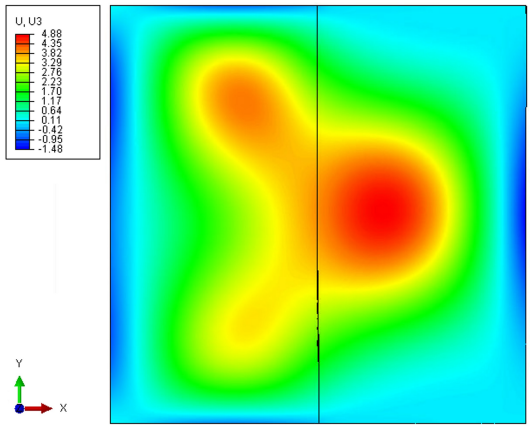
c) FE: residual stress + **no** rotational constraint	d) FE: residual stress + rotational constraint
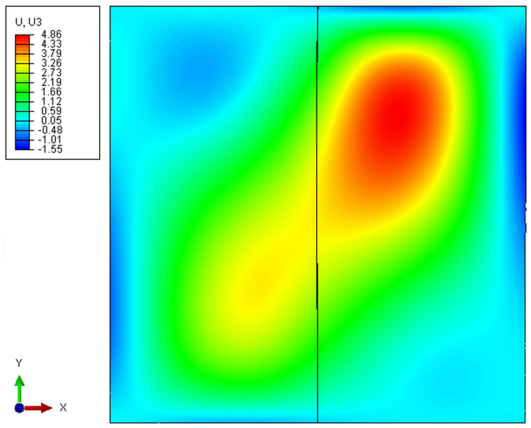	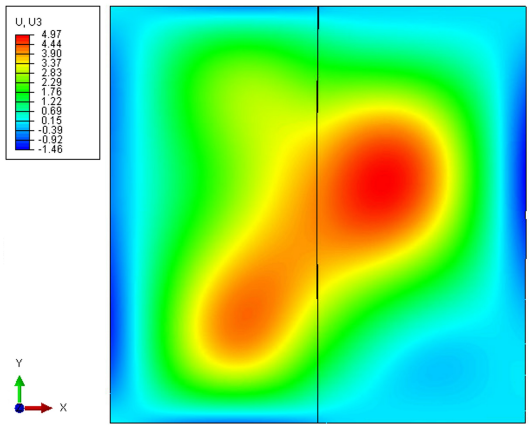

As with the previous experiment, a total of five contour plots are compared: one derived from the DIC measurements and four from different FE simulations. Figure 4.7-a displays the FE simulation without residual stress implementation and without a rotational constraint. A visual comparison between the DIC and this FE model reveals little resemblance. The FE simulation exhibits only a global buckling

mode, whereas the DIC results clearly demonstrate a localized buckling pattern.

The second FE simulation (Figure 4.7-b) shares the same setup as the second configuration of the third experiment. While residual stresses are still not included, a half rotational constraint is applied at the top and bottom right of the plate. This model exhibits a buckling pattern that more closely resembles the DIC results. Notably, symmetrical positive out-of-plane displacement regions are present, while the top and bottom left regions show slight asymmetry—similar to the DIC data. However, this simulation does not capture the negative out-of-plane displacements observed in the DIC measurements.

The third and fourth FE models incorporate residual stresses, with the distinction that the third model does not include rotational constraints, while the fourth does. In the third model, some qualitative similarities with the DIC results are observed. On the right side of the plate, an out-of-plane displacement area is visible, aligning with the DIC data. Additionally, a smaller positive displacement hotspot is present in the lower left corner, also matching the experimental results. However, both buckling regions appear to be shifted upward when compared to the DIC measurements.

The final FE simulation includes both residual stresses and the half rotational constraint. As was also observed in the third experiment, the addition of residual stresses slightly modifies the buckling behavior compared to the second FE model. While this configuration retains some similarity to the DIC results in terms of the locations of positive out-of-plane displacements, the overall deformation pattern remains predominantly global. In contrast, the DIC results exhibit clear localized buckling.

In line with the methodology used in the previous experiments, out-of-plane displacement profiles are extracted along the vertical center lines of both the left and right sides of the plate. Figure 4.26 presents these displacement curves, comprising one from the DIC measurements and four from the respective FE simulations.

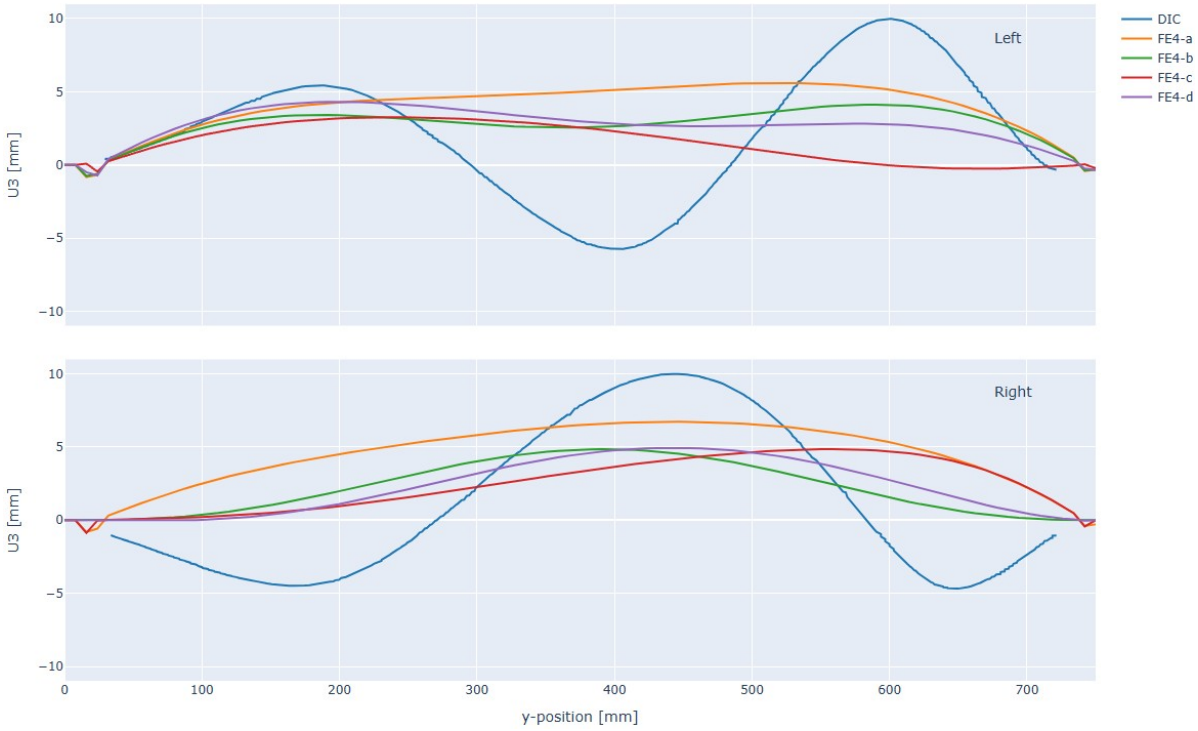

Figure 4.26: Out-of-plane displacement profiles plotted along the center lines of both the left and right sides of the plate for experiment 4

On the left side of the plate, three distinct displacement peaks are observed in the DIC results: two positive and one negative. In contrast, none of the FE4 models successfully reproduce these clear peak patterns. All FE4 models exhibit only positive displacements, with the FE4-b model being the only one that somewhat clearly displays two positive displacement peaks. These peaks appear at approximately the same locations along the center line of the plate as in the DIC results, around $y = 175\ mm$ and $y = 600\ mm$. However, the magnitude of the second positive peak predicted by the FE4-b model differs

substantially from that measured in the DIC data.

On the right side of the plate, three more displacement peaks are evident in the DIC measurements: two negative and one positive. While all FE4 models tend to show a single positive displacement peak, the FE4-c model predicts this peak at a different y-position than observed in the DIC data, and the FE4-a model exhibits one broad bulge across the entire plate rather than distinct peaks. The FE4-d model does capture a positive displacement peak at approximately $y = 425\ mm$, aligning with the DIC results. The FE4-b model also shows a positive peak, albeit slightly below this y-position. Nevertheless, as with the left side of the plate, the predicted displacement magnitudes deviate significantly from the DIC measurements.

Table 4.8 provides an overview of the calculated buckling resistances and the corresponding relative errors for all FE models considered in the fourth experiment.

Table 4.8: Relative buckling resistance errors between the DIC results and the FE results of experiment 4

		DIC	FE4-a	FE4-b	FE4-c	FE4-d
R_b	[*kN*]	1130	1199	1198	1075	1258
Error	[%]	-	6.1	6.0	-4.9	11.3

In line with the findings from the third experiment, the first two FE simulations (FE4-a and FE4-b) exhibit similar relative errors of approximately +6%, indicating a slight overestimation of the buckling resistance compared to the experimental value. The introduction of residual stresses in the third simulation (FE4-c), without the application of a rotational constraint, leads to a notable reduction in buckling resistance. This suggests that the residual stresses have an adverse effect on the structural performance in this configuration, resulting in a negative relative error. When both residual stresses and the half rotational constraint are applied (FE4-d), the relative error increases substantially to over 10%. This mirrors the trend observed in the fourth simulation of the third experiment, where the combined influence of residual stresses and rotational constraints led to a significant overestimation. Despite this, the relative errors for the first three simulations remain within an acceptable range—approximately ±5% in absolute terms—suggesting reasonable agreement between the FE predictions and the experimental results.

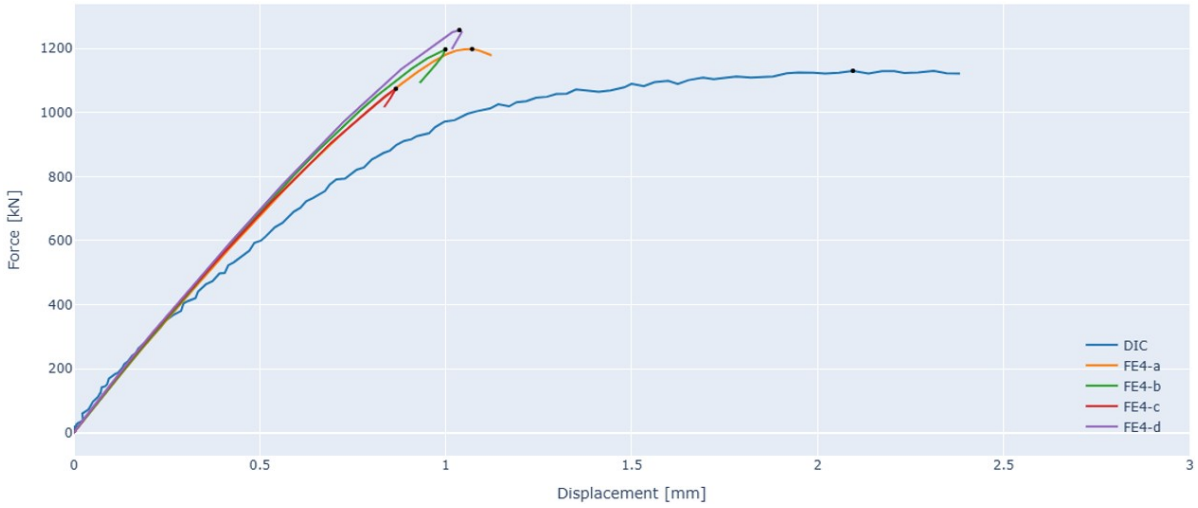

Figure 4.27: Force-displacement graphs of the DIC and FE model results from experiment 4

All FE models exhibit similar force–displacement responses, with each simulation reaching a vertical displacement of approximately $1\ mm$. The FE4-c model is the only case with a slightly lower buckling point, although it follows the same stiffness trend as the other FE models. In all cases, the FE results show stable behavior in which the force increases almost linearly with displacement until the bifurcation point is reached. Beyond this point, the displacement drops abruptly while the applied force decreases,

marking the onset of buckling. In contrast, the DIC results display little to no linear behavior. Instead, the experimental curve reaches a plateau, ultimately attaining a significantly higher maximum force at a vertical displacement exceeding $2\ mm$.

4.2.4.5. Eigenmode-based imperfection analyses

For the eigenmode-based imperfection analyses, only two FE models were created. In principle, the WAAM stiffener tests share the same FE model configuration, including boundary conditions and applied load, with the only difference being the initial plate imperfections. Therefore, a single eigenmode-based FE model is representative for both WAAM tests. The same reasoning applies to the prismatic rectangular stiffener tests. As a result, only two nonlinear FE analyses were required in total, one for each stiffener type (WAAM and rectangular).

Experiments with WAAM stiffener

The first GMNIA analysis discussed here corresponds to the two WAAM stiffener tests. As described in the Methodology chapter, the initial imperfection field was derived from the first linear buckling mode and scaled to the prescribed magnitude. From a validation perspective, it is not essential to match the exact out-of-plane displacement amplitudes at the maximum load, since the true imperfection magnitudes are generally unknown for design applications. Instead, the critical aspect is whether the analysis captures the correct buckling pattern. The first contour plot in Table 4.9 illustrates the out-of-plane displacement field of the plates with WAAM stiffeners at maximum load, which represents the characteristic buckling mode observed in the analysis. The remaining two images in the figure illustrate the out-of-plane displacements measured through DIC for both the first and second experiments, facilitating a comparative analysis.

Similar to the FE models based on the 3D scan-derived imperfections, several notable discrepancies were found between the eigenmode-based FE analyses and the DIC measurement results of the first experiment. When focusing only on the buckling pattern, it can be observed that the predicted deformation from the FE model does not correspond well to the measured response. Some resemblance can be seen on the left side of the plate, particularly in the localized negative out-of-plane displacement region, but overall the numerical prediction does not accurately reproduce the experimental buckling pattern. From a validation point of view, this implies that the eigenmode-based FE model is not fully representative for the first test.

In contrast, the results of the second experiment show much better agreement. The FE model captures the overall buckling pattern more convincingly, with the negative out-of-plane displacement regions appearing in roughly the same locations as in the DIC measurements. As discussed previously, the assumed imperfection shape was derived from the Eurocode provisions and therefore does not necessarily represent the actual imperfection field of the tested specimen. For this reason, the absolute displacement magnitudes should not be interpreted as realistic values. Instead, the comparison is made on the basis of the general buckling pattern. In this second case, both the DIC and FE results consistently show local buckling occurring on either side of the plate at comparable locations, which provides a higher level of confidence in the eigenmode-based approach for this test.

Table 4.9: Comparison of out-of-plane displacements between DIC and eigenmode-based FE model results at the buckling mode for experiment 1 and 2

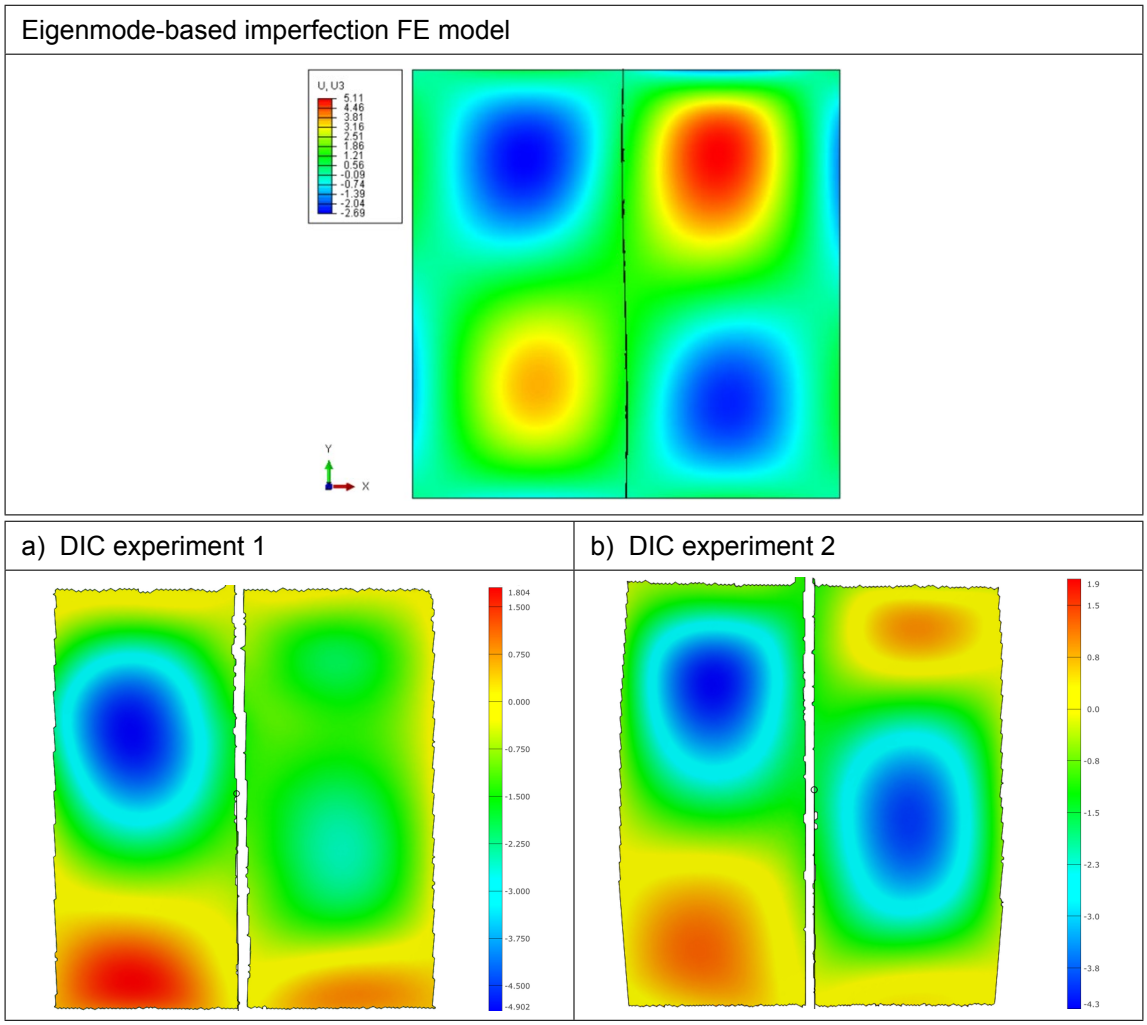

Experiments with rectangular stiffener

The second analysis corresponds to the tests with the prismatic rectangular stiffeners. Similar to the WAAM stiffener case, the FE model configuration is identical for both tests, with the only theoretical variation being the plate imperfections. The initial imperfection field was again based on the first linear buckling mode and scaled to the Eurocode-defined amplitude. Table 4.10 presents the out-of-plane displacement field at the maximum load level for the plates with rectangular stiffeners, clearly showing the characteristic buckling shape captured by the eigenmode-based imperfection approach in the first image. The remaining two images in the figure illustrate the out-of-plane displacements measured through DIC for both the third and fourth experiments.

The out-of-plane displacements at maximum load predicted by the eigenmode-based FE model exhibit a buckling pattern comparable to that of the model with the WAAM stiffener. The response is primarily governed by local buckling, with two distinct localized buckling regions forming on either side of the plate, separated by the stiffener. In contrast, the DIC measurements reveal an additional localized buckling region on each side of the plate, resulting in poor agreement with the FE predictions. Overall, the buckling patterns obtained from the eigenmode-based FE model show limited correspondence with the DIC results, similar to the observations made for the FE models incorporating 3D scan-based imperfections.

It is worth noting that the eigenmode-based FE model exhibits certain similarities with some of the 3D scan-based FE models at maximum load. Specifically, both approaches predict negative out-of-plane displacements at the top left and bottom right corners of the plate, accompanied by positive displace-

ments extending diagonally from the bottom left to the top right region. Nevertheless, the eigenmode-based imperfection implementation does not enhance the overall validation of the FE model.

Table 4.10: Comparison of out-of-plane displacements between DIC and eigenmode-based FE model results at the buckling mode for experiment 3 and 4

Eigenmode-based imperfection FE model	
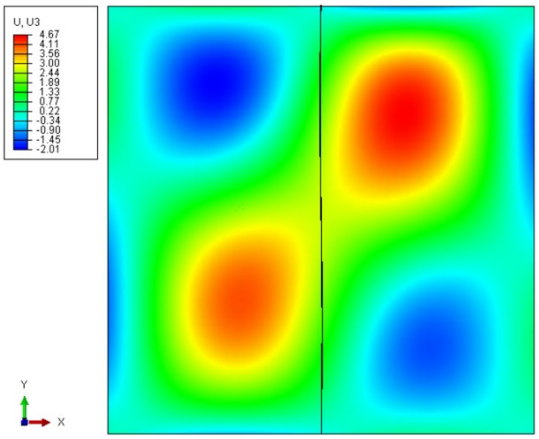	
a) DIC experiment 3	b) DIC experiment 4
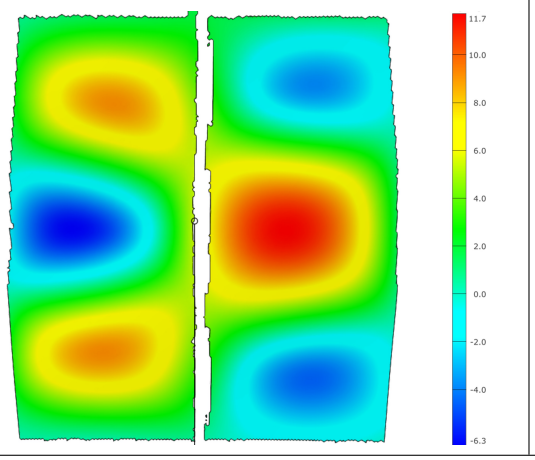	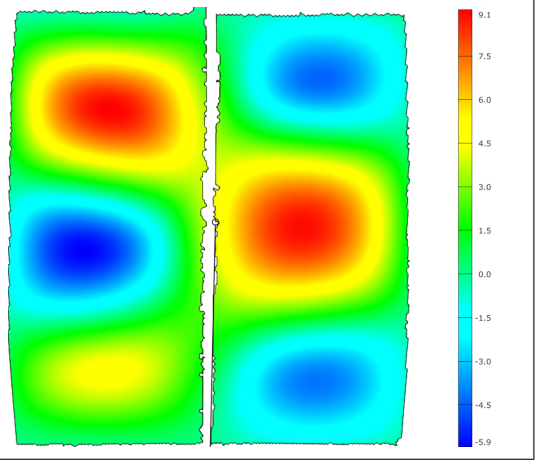

4.2.4.6. Digital image correlation-based imperfection analyses

Since the third and fourth FE models still failed to reproduce the experimental behavior satisfactorily, a final investigation was carried out to identify the underlying cause. In this approach, the deformation field of the third experiment measured by DIC at maximum load was introduced into the FE plate model (at a reduced amplitude) as an initial geometric imperfection. The purpose was to assess whether the experimentally observed deformation pattern acts as a starting point for the plate's buckling response. If the FE model amplifies this imposed pattern and reproduces the experimental buckling behavior, it would suggest that the experimental imperfection field explains the discrepancy between numerical and experimental results. On the other hand, if the FE model develops a different buckling mode or response, the mismatch is more likely attributable to modeling assumptions or boundary conditions for instance. Figure 4.28 illustrates the buckling modes observed at the maximum load for both the DIC measurements (a) and the FE model incorporating the DIC-based imperfections (b).

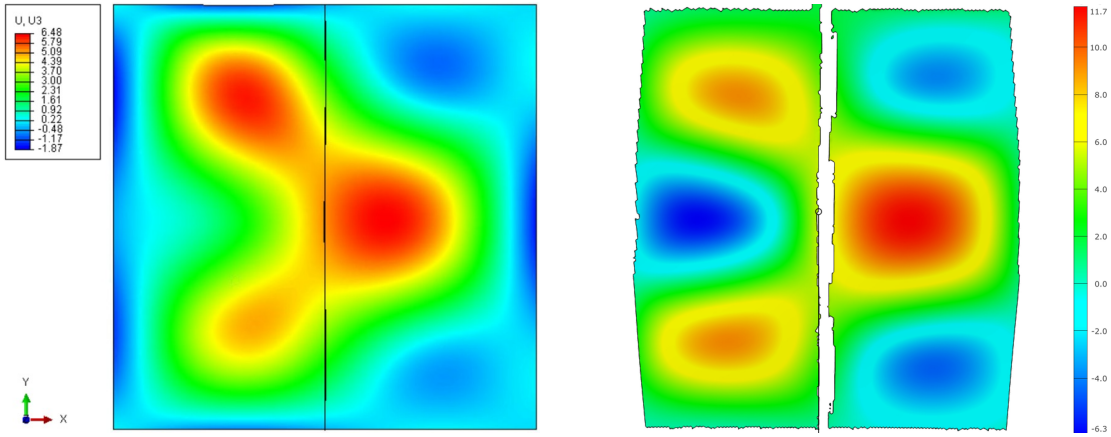

(a) Out-of-plane displacement field from DIC-based imperfection FE model at maximum load

(b) Out-of-plane displacement field measured by DIC at maximum load

Figure 4.28: Comparison of buckling modes between DIC measurements and FE model implementing the DIC-based imperfections of experiment 3

When the experimentally measured DIC buckling shape was applied as an initial imperfection in the FE model, the resulting numerical simulations produced buckling patterns similar to those observed in the experiment. This indicates that the experiment and model exhibit the same underlying instability mechanism once the actual imperfection field is included. The earlier discrepancies between numerical and experimental results are therefore most likely explained by unmodeled imperfections in the experimental setup or specimen, rather than deficiencies in the numerical approach.

4.3. Optimized stiffener performance

With the validation of the stability behavior of the topologically optimized stiffened slender plates completed, further investigations can now be conducted to explore the potential of WAAM-produced topologically optimized stiffeners. This section presents the stability analysis of such a newly developed TO stiffener. As described in the Methodology chapter, three different TO stiffener geometries were identified. By applying the efficiency formulas introduced earlier, the most efficient TO stiffener variant can be determined. Following the analysis of the stability behavior of the TO-stiffened plate, the corresponding stiffener efficiencies will be evaluated and compared against those of conventionally manufactured stiffeners with a simple rectangular prismatic shape, designed to follow the same curvature and thickness as the TO stiffeners.

4.3.1. Structural performance

Similar to the numerical validation process described in the previous sections, the new stiffeners are evaluated with respect to its stability behavior. This assessment includes the identification of buckling mode patterns, analysis of force–displacement behavior, and determination of buckling resistance.

As was carried out for the plates in earlier sections, a nonlinear buckling analysis is performed, incorporating both geometric and material nonlinearities as well as initial imperfections (GMNIA). The imperfections are modeled as a bow imperfection field with an amplitude of 5 mm applied to the 10 mm thick plate. The resulting buckling modes for the TO stiffened plates is presented in Figure 4.29.

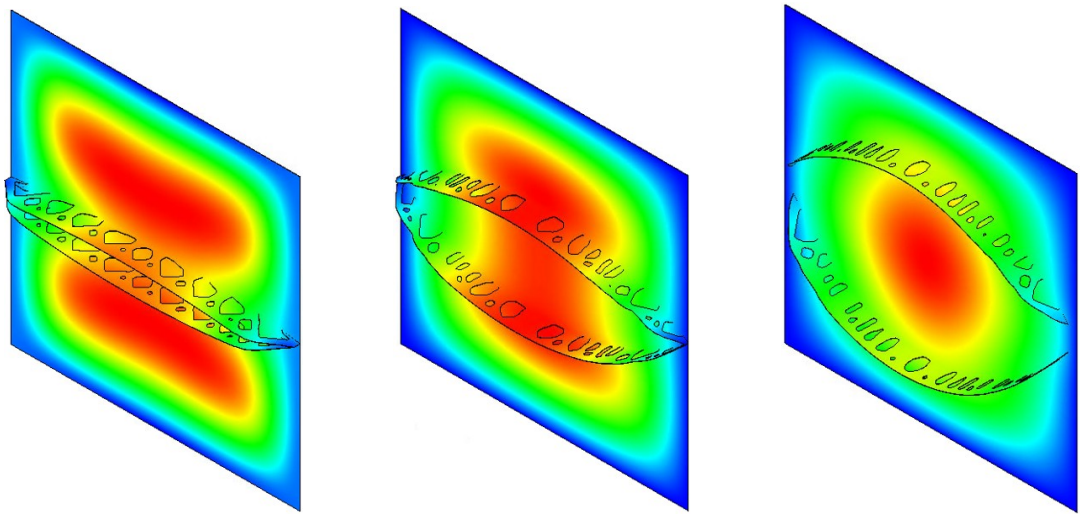

(a) Small variant **(b)** Medium variant **(c)** Large variant

Figure 4.29: Out-of-plane displacements of the plates with the TO stiffener variants

The figure illustrates the out-of-plane displacement field of the plate at the ultimate buckling load. For the small curvature variant, the first buckling mode is characterized mainly by localized buckling in the plate, with only small indications of global buckling. As the stiffener curvature increases (medium and large variants), the buckling response gradually shifts towards a more global character. In the large curvature variant, the response is dominated entirely by global buckling. From a stability perspective, localized buckling is more favorable, as it limits the maximum out-of-plane displacements significantly. In this regard, the small curvature variant provides the most promising behavior. It can also be anticipated that a further reduction in stiffener curvature would enhance this localized buckling response even more. Alternatively, increasing the stiffener thickness could be another effective means of achieving localized buckling.

To gain additional insight into the stability performance of the plates with topology-optimized stiffeners, the load–displacement response is examined (see Figure 4.30). For all variants, the curves remain nearly linear throughout most of the loading phase, before a sudden loss of stiffness occurs, corresponding to a snap-through point where the maximum load is reached. Consistent with the displacement field observations, the small curvature variant again outperforms the others. It demonstrates a higher stiffness and, consequently, a higher buckling resistance compared to the medium and large curvature variants.

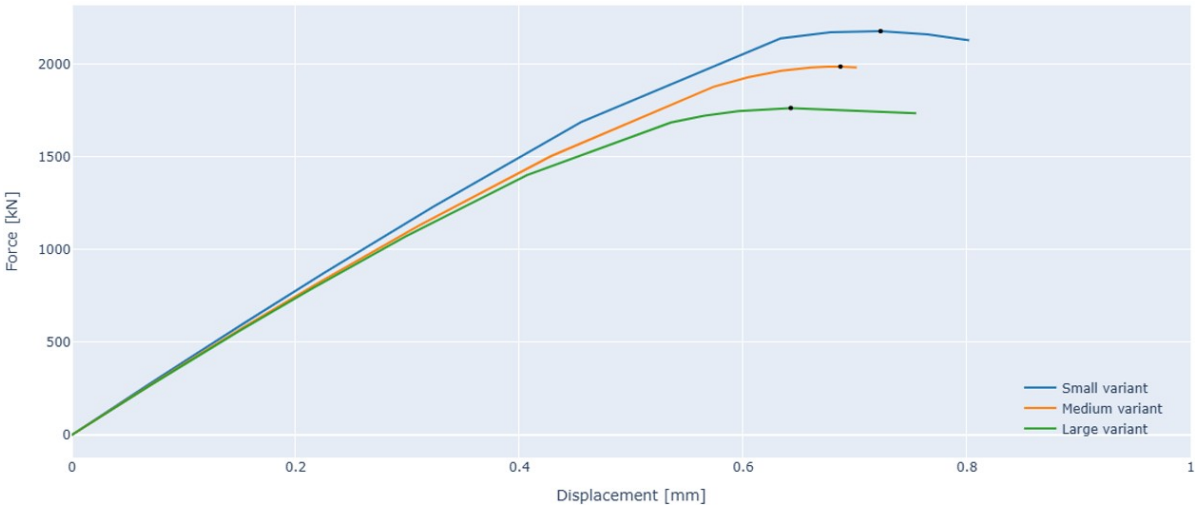

Figure 4.30: Load-displacement graph of the plate with the TO stiffener

It should be noted that an increase in stiffener curvature also requires a greater amount of material. Nevertheless, despite utilizing less material, the small curvature variant demonstrates superior performance compared to the medium and large TO variants.

4.3.2. Efficiency comparison

In this subsection, the efficiency of the TO stiffeners is evaluated. The TO stiffeners are compared with its curved prismatic rectangular cross section counterparts on two key performance indicators: the stiffener weight ratio (W_r) and the resistance ratio (R_r). A series of prismatic stiffeners with the same varying curvatures and thicknesses are considered. For each prismatic stiffener, the buckling resistance and stiffener weight are determined. These values are then used to calculate the efficiency (E_s) of the TO stiffener according to Equations 3.1 and 3.2, as introduced in the Methodology chapter. The results of these calculations are presented in Table 4.11.

Table 4.11: TO stiffener efficiencies calculated for each curved prismatic stiffener variation

	TO		*Prismatic*		
	V [mm³]	**R_b [kN]**	**V [mm³]**	**R_b [kN]**	**E_s [-]**
Small	1197908	2179.56	2010365	2243.5	1.63
Medium	1311330	1985.696	2144002	2175.68	1.49
Large	1461481	1762.252	2405426	1952.128	1.49

It should be noted that, in the table, the stiffener weights are replaced by their respective volumes. As explained in the Methodology chapter, all stiffeners are manufactured from materials with the same density, meaning that volume is directly proportional to weight. Consequently, using volume in place of weight yields identical efficiency ratios in the calculations.

Overall, all three topology-optimized stiffener variants exhibit high positive efficiency values. Among them, the small curvature variant demonstrates the most favorable efficiency, with a value of 1.63. This indicates that the TO stiffener significantly outperforms its non-optimized counterpart. Notably, the volume of the stiffener is reduced by nearly 50%, while the maximum buckling load decreases only marginally, resulting in the high efficiency value. The medium and large curvature variants achieve the same stiffener efficiency, which suggests that, in terms of weight reduction relative to stability performance, both perform at a comparable level.

Considering both the structural performance and the stiffener efficiency criteria, it can be concluded that the small TO stiffener variant achieves superior performance across all measures. Figure 4.31 presents the final geometry of this small variant.

Figure 4.31: 3D model of the final stiffener geometry, including plate and stiffener thickness

Although the small variant of the TO stiffener demonstrates superior performance compared to the other TO variants across all evaluation criteria, it is crucial to benchmark its behavior against conventional stiffening concepts. Specifically, validation against traditional prismatic plate stiffeners under uniaxial compression is necessary to assess whether the new TO design provides any practical advantages. If the TO stiffener performs worse overall than a conventional stiffener, its implementation would not be justified.

To facilitate this comparison, a traditional prismatic rectangular stiffener with an equivalent volume to the TO stiffener was considered. The stiffener was positioned along the centerline of the plate, with the same thickness as the TO design (10 mm), allowing only the stiffener depth to vary. Based on the volume of the TO stiffener, the corresponding depth of the traditional stiffener was determined to be 120 mm. A structural stability analysis was then conducted, yielding a maximum buckling load of 2218 kN for the conventional stiffener under uniaxial compression. This indicates that, for an equal volume, the conventional stiffener performs only marginally better than the small TO variant. Overall, their performance is comparable, suggesting that the introduction of a TO stiffener does not provide a clear advantage over the conventional design under the investigated loading conditions. Nevertheless, the TO stiffener may present benefits in specific scenarios where conventional stiffeners cannot be applied. For example, in cases where the use of a central stiffener is restricted, the TO stiffener could offer a viable alternative. Additional potential applications include situations with non-uniform uniaxial compression, where altered load distribution paths may occur. In such cases, the TO stiffener could positively influence the buckling resistance. These possibilities, however, require further investigation.

4.3.3. Extended evaluation of the stiffener topology optimization

Geometry post-processing

The final geometry of the TO stiffener contained several small gaps, which posed challenges for manufacturing. During the AM process, such narrow gaps are difficult to reproduce reliably, as they are prone to being filled with molten material. This phenomenon has been observed in practice, where small holes in the TO geometry tend to close unintentionally during fabrication. For this reason, post-processing of the geometry was carried out to enhance manufacturability. In this step, the smaller gaps were removed, resulting in the final post-processed stiffener shown in Figure 4.32.

Figure 4.32: 3D model of the final stiffener geometry after post-processing, including plate and stiffener thickness

As a consequence of this modification, the overall volume and weight of the stiffener increased slightly. The added material also led to a marginal rise in the plate's buckling resistance, yielding a revised stiffener efficiency of **1.58**. Although this value is somewhat lower than the original efficiency, it remains a strong result and reflects a reasonable trade-off between structural performance and manufacturing feasibility.

Another critical feasibility consideration concerns the overhang angle of the stiffener. As discussed in the Methodology chapter, a maximum allowable overhang of 60° was imposed. Post-optimization verification was therefore necessary to ensure this requirement was satisfied. A visual inspection revealed that the triangular gaps in the stiffener exhibited overhang angles of approximately 45°, well within the 60° limit. In contrast, the smaller gaps that were eliminated during post-processing presented critical points with more horizontal configurations, exceeding the 60° threshold. Their removal was therefore justified not only from a manufacturability standpoint but also in terms of geometric robustness.

Effect of initial plate imperfections

As described earlier, an initial bow-shaped imperfection with an amplitude of 5 mm was introduced into the plate model prior to the topology optimization process. This imperfection was applied consistently throughout the analysis. However, the chosen value of 5 mm was based on an assumption and could potentially influence the optimization outcome. To investigate the sensitivity of the results to the assumed imperfection magnitude, an additional study was carried out using a reduced imperfection amplitude.

Since the small TO variant was previously identified as the most promising configuration, this geometry was selected for further testing. A new topology optimization was performed with an initial imperfection amplitude of 1 mm, while maintaining the same FE model characteristics used in the original analysis. The resulting material density distributions of both cases, the small TO variant with a 5 mm bow imperfection and the corresponding variant with a 1 mm imperfection, are compared in Figure 4.33.

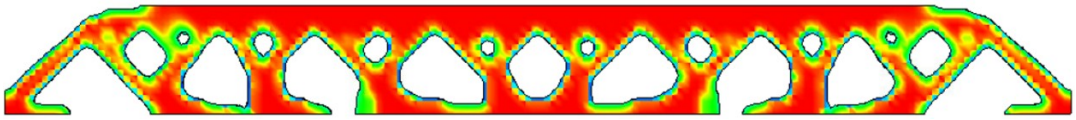

(a) Material density distribution of the 5 mm imperfection variant

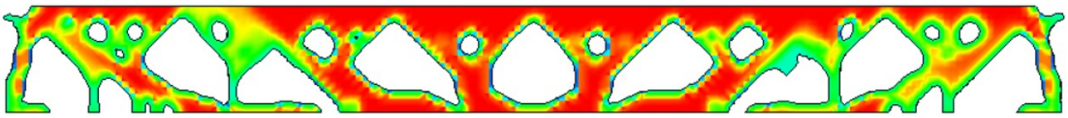

(b) Material density distribution of the 1 mm imperfection variant

Figure 4.33: Material density distributions of the small TO variant with a 5 mm and 1 mm bow imperfection

The comparison between the stiffeners obtained with 5 mm and 1 mm bow imperfections reveals notable differences, particularly towards the ends of the stiffener. In the central region, the characteristic triangular gaps, where the material density is zero, appear in both cases with small deviations. However, progressing towards the edges of the stiffener, the resulting topologies diverge more substantially, with the geometry of the stiffener ends being strongly affected by the imposed imperfection amplitude. For plates with larger initial imperfections, the optimization algorithm tends to concentrate more material near the center of the stiffener, whereas for plates with smaller imperfections, more material is allocated along the boundary edges of the plate.

5

Conclusions and Recommendations

5.1. Conclusions

5.1.1. Numerical validation

The numerical validation process was carried out separately for the WAAM-produced stiffeners and the prismatic stiffeners, as the results for each configuration differed considerably. Treating them individually ensures that conclusions are drawn on an engineeringly objective basis.

For the **WAAM-produced stiffeners**, the following conclusions were reached:

- **First experiment** – Both the buckling resistance and the load–displacement response showed discrepancies too large to be considered a valid match. The FE models and the experimental results differed significantly in buckling resistance and plate stiffness, as indicated by the load–displacement curves. These deviations suggest that an error likely occurred during the experiment, leading to unreliable validation results. This discrepancy may be connected to the excessive out-of-plane displacements observed at the boundary edges of the plate. Such behavior could result from insufficient or uneven clamping of the plate within the experimental setup.
- **Second experiment** – The experimental results and FE validation show good agreement. The FE models predict similar buckling patterns to those observed in the DIC measurements, including comparable out-of-plane displacement magnitudes. Buckling resistance predictions were highly accurate, with relative errors below 5%, and the load–displacement curves showed good agreement in stiffness. The best match was obtained with the boundary condition configuration using half rotational constraints at the top and bottom edges of the right side of the plates, although this choice was based on trial and error rather than a clear physical rationale.

For the **rectangular prismatic stiffeners**, the following conclusions were reached:

- **Third experiment** – Significant discrepancies were found between the buckling modes from the DIC data and the FE predictions. Only the FE model with half rotational constraints at the top and bottom edges of the right side of the plates produced a somewhat comparable buckling pattern, although the displacement magnitudes remained much lower than those measured experimentally. Displacement variations up to 7 mm were recorded. Nevertheless, the buckling resistance errors were below 5%, indicating that the maximum resistance point could still be predicted with high accuracy. The load–displacement curves, however, differed greatly: the experiment reached a plateau, while the FE models exhibited an almost immediate snap-through.
- **Fourth experiment** – The results closely mirrored those of the third experiment, with buckling resistance errors around 5% and similar buckling patterns only for the half rotational constraint model. Large stiffness discrepancies between FE and experimental results were again observed. Up to 400 kN, the stiffness of both the FE models and the experimental results remained consistent; however, beyond that point, the experimental data began to plateau in the load-displacement graph, diverging from the FE models.

- **Residual stress implementation** – Including residual stresses altered the behavior of both the third and fourth experiments slightly, but without clear improvement in model validation. It is important to note that the residual stresses are assumed, derived from the application of displacements to the plate due to its insertion into the experimental setup. The most notable change was a reduction in ultimate buckling load for models without rotational constraints at the top and bottom edges of the right side of the plates. In contrast, models with half rotational constraints experienced an increase in buckling resistance.
- The numerical validation showed that the initial FE models did not reproduce the experimental results accurately for the third and fourth experiment. However, when the experimentally measured buckling shape was introduced as an imperfection field, the FE simulations produced buckling patterns consistent with those observed in the experiments. This finding suggests that the discrepancies are primarily caused by imperfections present in the experimental specimens and setup.

5.1.2. Stiffener topology optimization

The second part of this research focused on the topology optimization of a stiffener for a slender plate. With the validation of the WAAM-produced stiffeners completed, the stability behavior of alternative WAAM-fabricated stiffener geometries could be assessed. The main conclusions from the topology optimization study are as follows:

- Three different topology-optimized stiffeners were obtained, ranging in curvature from small to large. The curvature variables represent the curvatures of the initial stiffener shapes, which adhere to an elliptical form. Among these, the small curvature variant demonstrated the highest stiffener efficiency compared to its prismatic counterpart following the same curve.
- Despite this, the small curvature TO variant behaves similarly to a prismatic rectangular stiffener placed along the plate centerline, with equivalent total stiffener volume. In terms of buckling resistance, the TO design offers no clear advantage over a conventional stiffener.
- Post-processing of the TO stiffener was necessary to ensure manufacturability. The small gaps present in the original design were removed, which led to a slight increase in material usage. However, this modification improved the overall feasibility of producing the stiffener.
- The magnitude of the initial plate imperfection was found to significantly influence the TO process. Reducing the imperfection amplitude from 5 mm to 1 mm (bow imperfection field) resulted in a visibly higher concentration of material along the stiffener edges. This trend highlights the sensitivity of the optimization results to the assumed imperfection amplitude, although the exact increase in edge material could not be quantified within the scope of this study.

5.2. Recommendations for practice

From a manufacturing perspective, it has become clear that imperfections introduced during the welding process can reach significant magnitudes if not properly controlled. During the WAAM stiffener manufacturing process, heavy weights were applied to constrain the entire plate, effectively minimizing large distortions. In contrast, the plates with conventionally welded stiffeners were subjected to much lighter and less constraints, which resulted in substantially larger and more unfavorable plate imperfections, in some cases up to four times higher than those observed in the WAAM specimens. It is therefore recommended that initial imperfections be reduced as much as possible during the manufacturing stage, as they have a pronounced negative impact on the stability behavior of the plate.

In the context of experimental validation, particular care should be given to the clamping of specimens. The inconsistent results of the first experiment may be attributed to insufficient clamping, which effectively compromised the intended boundary condition. Poorly applied boundary conditions or misalignment can introduce setup-induced displacements that reduce comparability with numerical predictions. Similarly, the discrepancies observed in experiments 3 and 4 may be explained by unaccounted interactions between the specimen and the setup. Such effects highlight the importance of carefully considering setup–specimen interactions during experimental design.

Poorly applied boundary conditions or misalignment can introduce setup-induced displacements that reduce comparability with numerical predictions.
From a modeling standpoint, accurate representation of initial plate imperfections is crucial. While the use of DIC reference stages provides a reasonably accurate estimate of displacements, it may not fully capture the true imperfection profile of the plate. Incorporating 3D scanning technology can further enhance the accuracy of imperfection measurements, thereby improving the accuracy of FE model predictions. This once again underlines the strong influence of initial imperfections on structural stability.

Finally, in stiffener topology optimization, printing feasibility must be considered alongside performance. Practical manufacturing limitations, such as maximum allowable overhangs and the presence of small holes or gaps in the optimized geometry, should be taken into account. Excessive overhangs can cause the intended geometry to change during the WAAM process, while very narrow gaps may inadvertently become filled with material during printing, resulting in undesired stiffener geometries. Ensuring printability therefore forms an essential step in translating optimized designs into manufacturable and structurally reliable components.

5.3. Future research

Future studies could expand upon the present work by investigating the stability behavior of WAAM-stiffened plates under different loading conditions. While this study considered uniaxial compression, alternative load cases such as biaxial compression or shear forces could be applied to provide a broader understanding and validation of the plates' stability performance. In addition, extending the research to other slender structures, such as shells, may offer further insights into the applicability of WAAM stiffeners in diverse structural configurations.

With respect to stiffener design, this research employed an intuitive approach to defining the initial stiffener geometry. A promising direction for future work would be to explore the use of optimization algorithms to systematically determine the initial stiffener location, shape, and thickness. Such an approach would enable the identification of optimal configurations tailored to specific loading conditions. These optimized base geometries could then serve as input for a later topology optimization step, allowing for further refinement of the design and additional material savings.

6

Discussion

6.1. Key findings

The findings of this study highlight the critical role of initial imperfections in stability analysis. Capturing plate imperfections accurately is essential for predicting the stability behavior of stiffened plates under uniaxial compression. From the experimental campaign, the test conducted with a WAAM stiffener provided valuable validation, demonstrating that the stability behavior of plates reinforced with WAAM stiffeners can fairly well be predicted, although the absence of repeated tests on nominally identical specimens limits the confirmation of this conclusion. In the second WAAM stiffener test, aspects such as buckling patterns and load–displacement responses were predicted with good accuracy, provided that the measured imperfections were incorporated into the finite element model. These findings lend partial support to the hypothesis that the stability behavior of WAAM-stiffened slender plates can be predicted using FEM. However, the limited number of WAAM test specimens prevents a definitive confirmation of this conclusion.

From the perspective of stiffener topology optimization, the results indicate that the choice of stiffener geometry and topology has a substantial influence on structural performance under uniaxial compression. Variations in stiffener shape and thickness strongly affect key stability aspects, including local and global buckling behavior. The optimization study showed, however, that the specific TO-derived stiffener geometry investigated did not present clear advantages over conventional prismatic stiffeners. Based on these findings, it appears most effective to adopt a prismatic rectangular stiffener as the initial geometry prior to applying topology optimization. Nevertheless, the possibility remains that alternative initial geometries could offer advantages in other contexts and should not be dismissed outright.

6.2. Implications for structural design

From a structural design perspective, a key implication of this research is the critical importance of accurately capturing initial plate imperfections when predicting the stability behavior of WAAM-stiffened plates. Current code-based approaches, such as those outlined in NEN-EN 1993-1-5, typically rely on simplified representations of initial imperfections. While these models may provide an approximate prediction of stability behavior, they are not sufficiently accurate. In particular, they fail to capture the distinct imperfection characteristics of WAAM-stiffened plates compared to conventional stiffeners. The differences in imperfection patterns between WAAM and conventional stiffeners are significant and must be accounted for in design considerations.

For practicing engineers, this finding underscores the need to place greater emphasis on imperfection measurement. By doing so, the stability performance of WAAM-stiffened plates can be predicted more reliably, enabling their safe and efficient use. Looking ahead, it is likely that design standards, such as the Eurocode, will need to adapt by introducing specific foundations for additively manufactured structural elements, thereby ensuring that the effects of imperfections are properly addressed.

6.3. Limitations and uncertainties

As with any research, several limitations and uncertainties must be acknowledged in this study. The results are based on a specific configuration of a plate with a stiffener, which means that the findings cannot be generalized without caution. Other structural elements, such as stiffened member profiles or shell structures, may exhibit different stability behavior under similar conditions.

From an experimental perspective, the most significant limitation is the small number of test specimens. Only two WAAM stiffeners were manufactured, which restricted the number of experiments. This inherently reduces the confidence level of the findings, as one test alone is insufficient to confirm a hypothesis, and the results of the second test cannot be validated independently.

Measurement accuracy is another source of uncertainty. Displacements and initial imperfections were recorded using DIC. Although DIC is generally regarded as a precise method, its accuracy was not independently verified in this study. Since the measured imperfections were used as input for the FE models, any inaccuracy in DIC measurements directly propagates into the numerical predictions. Given the strong influence of initial imperfections on plate stability, this introduces a notable source of uncertainty.

Material modeling also presented limitations. For the S355 steel plates, tensile tests provided material properties that were directly implemented in the FE models. In contrast, no tensile tests were available for the WAAM-deposited ER70s material. Instead, a bilinear material model was assumed to approximate its plastic behavior. While this simplification is not expected to dominate the results, it still represents an uncertainty that should be recognized.

The experimental program focused exclusively on uniaxial compression. Other loading scenarios, such as biaxial compression, shear, or combined loading, were not considered. Under such conditions, WAAM stiffeners and the corresponding plates may exhibit different stability behavior, limiting the generality of the present findings.

Finally, uncertainties are also present in the topology optimization part of the study. It remains unclear how the optimized stiffener geometries perform at different scales, since nonlinear stability behavior does not scale proportionally with plate size. Manufacturing constraints associated with WAAM also impose limitations. Challenges such as gaps, holes, overhangs, and machine-specific constraints affect the feasibility of certain topologies. Although some WAAM systems can address these challenges more effectively than others, complexity should ideally be reduced to improve manufacturability. Each optimized topology therefore comes with its own set of limitations that must be evaluated individually.

References

[1] Trayana Tankova and Milan Veljkovic. “Stiffening of slender plates using Wire Arc Additive Manufacturing”. In: *ce/papers* 6.3-4 (2023), pp. 788–791. DOI: https://doi.org/10.1002/cepa.2655. eprint: https://onlinelibrary.wiley.com/doi/pdf/10.1002/cepa.2655. URL: https://onlinelibrary.wiley.com/doi/abs/10.1002/cepa.2655.

[2] A. Gheitasi and M.M. Alinia. “Slenderness classification of unstiffened metal plates under shear loading”. In: *Thin-Walled Structures* 48.7 (2010), pp. 508–518. ISSN: 0263-8231. DOI: https://doi.org/10.1016/j.tws.2010.02.004. URL: https://www.sciencedirect.com/science/article/pii/S0263823110000418.

[3] Tadeh Zirakian and Jian Zhang. “Buckling and yielding behavior of unstiffened slender, moderate, and stocky low yield point steel plates”. In: *Thin-Walled Structures* 88 (2015), pp. 105–118. ISSN: 0263-8231. DOI: https://doi.org/10.1016/j.tws.2014.11.022. URL: https://www.sciencedirect.com/science/article/pii/S026382311400353X.

[4] CEN. *Eurocode 3 - Design of steel structures - Part 1-14: Design assisted by finite element analysis*. Brussels, Belgium: European Committee for Standardization (CEN), 2023.

[5] CEN. *Eurocode 3 - Design of steel structures - Part 1-5: Plated structural elements*. Brussels, Belgium: European Committee for Standardization (CEN), 2005.

[6] Nick McCormick and Jerry Lord. “Digital Image Correlation”. In: *Materials Today* 13.12 (2010), pp. 52–54. ISSN: 1369-7021. DOI: https://doi.org/10.1016/S1369-7021(10)70235-2. URL: https://www.sciencedirect.com/science/article/pii/S1369702110702352.

[7] Wikipedia contributors. *Strain gauge*. 2025. URL: https://en.wikipedia.org/w/index.php?title=Strain_gauge&oldid=1268540542 (visited on 03/10/2025).

[8] Sze Wei Khoo, Saravanan Karuppanan, and Cs Tan. “A Review of Surface Deformation and Strain Measurement Using Two-Dimensional Digital Image Correlation”. In: *Metrology and Measurement Systems* 23 (Sept. 2016). DOI: 10.1515/mms-2016-0028. URL: https://doi.org/10.1515/mms-2016-0028.

[9] Ted Nachazel. *What is a Strain Gauge and How Does it Work?* Aug. 2020. URL: https://www.michsci.com/what-is-a-strain-gauge/?cn-reloaded=1&cn-reloaded=1 (visited on 03/11/2025).

[10] Kai Treutler and Volker Wesling. “The Current State of Research of Wire Arc Additive Manufacturing (WAAM): A Review”. In: *Applied Sciences* 11.18 (2021). ISSN: 2076-3417. DOI: 10.3390/app11188619. URL: https://www.mdpi.com/2076-3417/11/18/8619.

[11] TWI. *What is Directed Energy Deposition (DED)?* URL: https://www.twi-global.com/technical-knowledge/faqs/directed-energy-deposition#:~:text=Directed%20Energy%20Deposition%20(DED)%20is,simultaneously%20deposited%20by%20a%20nozzle. (visited on 03/11/2025).

[12] Kun Li et al. “Additive manufacturing of ultra-high strength steels: A review”. In: *Journal of Alloys and Compounds* 965 (2023), p. 171390. ISSN: 0925-8388. DOI: https://doi.org/10.1016/j.jallcom.2023.171390. URL: https://www.sciencedirect.com/science/article/pii/S0925838823026932.

[13] Abid Shah et al. “A Review of the Recent Developments and Challenges in Wire Arc Additive Manufacturing (WAAM) Process”. In: *Journal of Manufacturing and Materials Processing* 7 (May 2023), p. 97. DOI: 10.3390/jmmp7030097. URL: https://doi.org/10.3390/jmmp7030097.

[14] Emanuel B. F. Dos Santos et al. “On the Visualization of Gas Metal Arc Welding Plasma and the Relationship Between Arc Length and Voltage”. In: *Applied Sciences* 7.5 (2017). ISSN: 2076-3417. DOI: 10.3390/app7050503. URL: https://www.mdpi.com/2076-3417/7/5/503.

[15] L. Gardner et al. “I-section steel columns strengthened by wire arc additive manufacturing - concept and experiments”. In: *Engineering Structures* 306 (2024), p. 117763. ISSN: 0141-0296. DOI: https://doi.org/10.1016/j.engstruct.2024.117763. URL: https://www.sciencedirect.com/science/article/pii/S0141029624003250.

[16] H. Abusalma et al. “Parametric study of residual stress formation in Wire and Arc Additive Manufacturing”. In: *Journal of Manufacturing Processes* 75 (2022), pp. 863–876. ISSN: 1526-6125. DOI: https://doi.org/10.1016/j.jmapro.2022.01.043. URL: https://www.sciencedirect.com/science/article/pii/S1526612522000603.

[17] Iulia Tarus et al. “Evaluation of material properties of 3D printed carbon steel for material modelling”. In: *ce/papers* 4.2-4 (2021), pp. 1650–1656. DOI: https://doi.org/10.1002/cepa.1469. eprint: https://onlinelibrary.wiley.com/doi/pdf/10.1002/cepa.1469. URL: https://onlinelibrary.wiley.com/doi/abs/10.1002/cepa.1469.

[18] Ole Sigmund and Kurt Maute. “Topology optimization approaches”. In: *Structural and Multidisciplinary Optimization* 48.6 (Aug. 2013), pp. 1031–1055. DOI: 10.1007/s00158-013-0978-6. URL: https://doi.org/10.1007/s00158-013-0978-6.

[19] Dassault Systèmes. *SIMP Method for Topology Optimization*. 2019. URL: https://help.solidworks.com/2019/english/solidworks/cworks/c_simp_method_topology.htm (visited on 09/01/2025).

[20] Dassault Systèmes. *Material Interpolation*. 2024. URL: https://docs.software.vt.edu/abaqusv2024/English/TsoUserMap/tso-c-user-TopOpt-Sett-Sensi-MatInt.htm (visited on 09/01/2025).

[21] Robin Larsson. “Methodology for topology and shape optimization: Application to a rear lower control arm”. MSc thesis. Chalmers University of Technology, 2016. URL: https://publications.lib.chalmers.se/records/fulltext/238778/238778.pdf.

[22] Krister Svanberg. “The method of moving asymptotes—a new method for structural optimization”. In: *International Journal for Numerical Methods in Engineering* 24.2 (Feb. 1987), pp. 359–373. DOI: 10.1002/nme.1620240207. URL: https://doi.org/10.1002/nme.1620240207.

[23] Sian I. Evans et al. “A review of WAAM for steel construction – Manufacturing, material and geometric properties, design, and future directions”. In: *Structures* 44 (2022), pp. 1506–1522. ISSN: 2352-0124. DOI: https://doi.org/10.1016/j.istruc.2022.08.084. URL: https://www.sciencedirect.com/science/article/pii/S2352012422007378.

A

Additional Finite Element Models

A.1. Additional residual stress implementation models

As outlined earlier, two different approaches were employed to implement the residual stresses in the plates for experiments 3 and 4. In the first approach, the FE model incorporated plate imperfections introduced by imposing out-of-plane displacements at the boundary conditions. In the second approach, the residual stresses were combined with initial plate imperfections obtained from the DIC measurements. Since both approaches produced nearly identical results, the latter method is included in Appendix A as supplementary material.

Furthermore, the results demonstrated that introducing the half rotational constraint did not lead to any notable improvements. Consequently, the FE models presented in this appendix are based solely on the original boundary condition configuration, without the half rotational constraints.

Experiment 3 - rectangular stiffener

Residual stresses were now also implemented together with the DIC-based plate imperfections to allow for a more detailed and realistic representation of the physical setup. The analysis for the third experiment resulted in a maximum LPF of 1.3758, corresponding to a buckling resistance of:

$$R_b = 750 \cdot 1.3758 = 1031.87 \text{ kN}$$

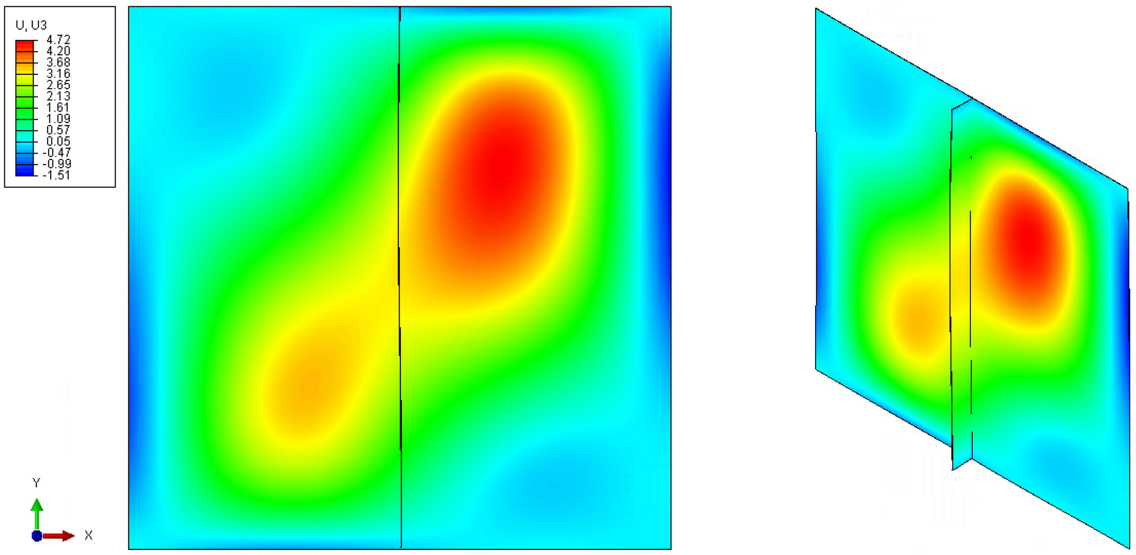

Figure A.1: FE model of experiment 3 illustrating the buckling mode with residual stresses applied, using DIC-based initial plate imperfections

Experiment 4 - rectangular stiffener
Residual stresses were now also implemented together with the DIC-based plate imperfections to allow for a more detailed and realistic representation of the physical setup. The analysis for the third experiment resulted in a maximum LPF of 1.4231, corresponding to a buckling resistance of:

$$R_b = 750 \cdot 1.4231 = 1067.35 \text{ kN}$$

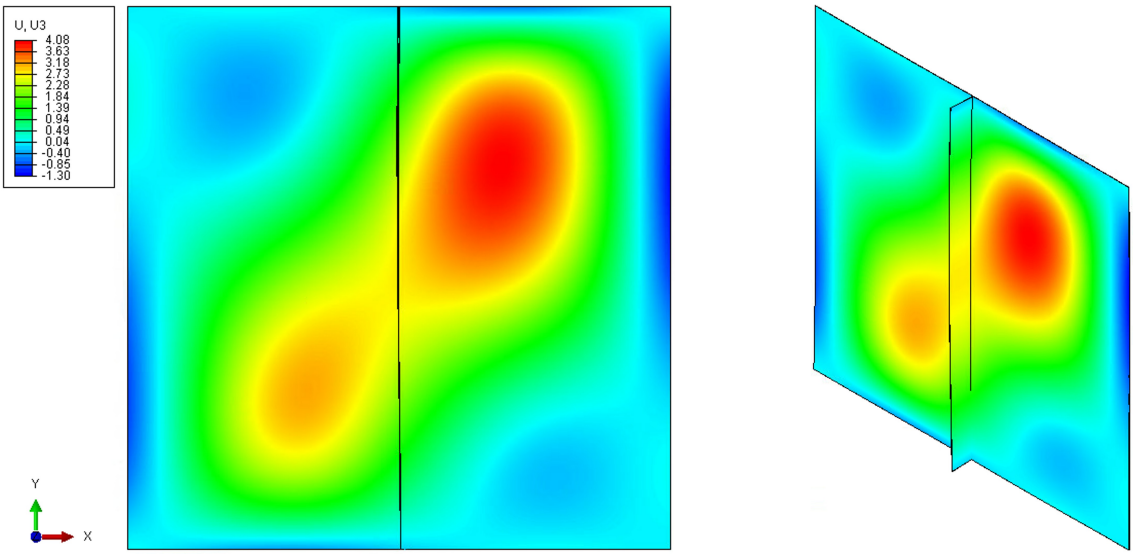

Figure A.2: FE model of experiment 4 illustrating the buckling mode with residual stresses applied, using DIC-based initial plate imperfections

A.2. Finite element model with reduced line constraint

This section presents the FE model corresponding to the observed deviation at the vertical out-of-plane line constraint on the left side of the plate. The experimental results indicated that insufficient clamping at this location likely reduced or eliminated the intended constraint. To replicate this behavior numerically, an FE model was generated with a reduced left-side line constraint. The resulting model is shown below.

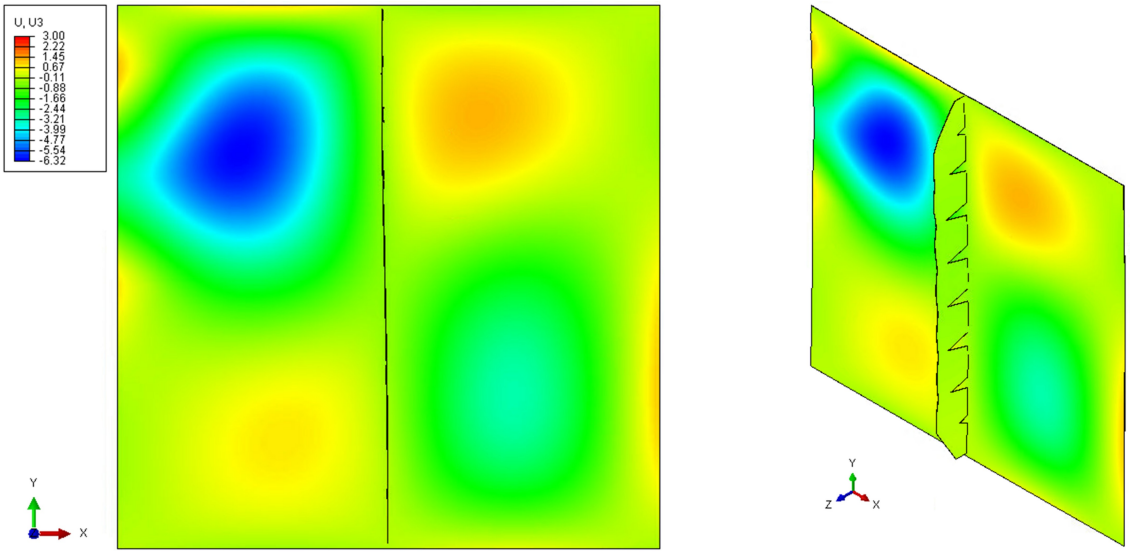

Figure A.3: FE model of experiment 1 illustrating the buckling mode as a result of the out-of-plane BC displacements at the left edge of the plate

B

Python Scripts

B.1. 3D scan downsampling

The first main Python script developed for this study performs downsampling of the point clouds obtained from the 3D scans. A grid-based downsampling approach is applied, which reduces the total number of points in the dataset by dividing the space into a regular grid of cubes (voxels). All points within each voxel are then represented by a single point, taken here as the first point within the voxel.

```python
import numpy as np

def downsample_grid(input_file, output_file, grid_size=5.0):
    """
    Reduces the number of points in a point cloud using grid-based (voxel) downsampling.

    Parameters:
    - input_file: str -> Path to the input point cloud file.
    - output_file: str -> Path to save the downsampled point cloud.
    - grid_size: float -> Size of the grid cells in which to group points.
    """
    # Load the point cloud (handling inconsistent spaces)
    points = []
    with open(input_file, 'r') as f:
        for line in f:
            points.append([float(value) for value in line.split()])

    points = np.array(points)  # Convert to NumPy array

    # Compute voxel grid indices for each point
    voxel_indices = np.floor(points / grid_size).astype(int)

    # Create a dictionary to store unique voxels (one representative point per voxel)
    voxel_dict = {}
    for i, voxel in enumerate(map(tuple, voxel_indices)):
        if voxel not in voxel_dict:
            voxel_dict[voxel] = points[i]  # Store the first point found in the voxel

    # Extract downsampled points
    downsampled_points = np.array(list(voxel_dict.values()))

    # Save to new file
    np.savetxt(output_file, downsampled_points, fmt='%.6f', delimiter=' ')

```

```
    print(f"Downsampled from {len(points)} to {len(downsampled_points)} points. Saved to
    ↪ {output_file}.")
```

B.2. Grid-based imperfection interpolation

Another key Python script used in this study performs the interpolation of measured surface imperfections from the 3D scan onto the FE mesh nodes. The script first loads the scan point cloud and the FE mesh grid. After optional manual alignment, a linear interpolation is applied to estimate the out-of-plane displacement (z-coordinate) of each mesh node based on the scanned surface. For nodes lying outside the convex hull of the scan data, a nearest-neighbor interpolation is used as a fallback to ensure full coverage of the mesh.

```
import numpy as np
from scipy.interpolate import griddata

def imperfection_interpolation(scan_file, mesh_file, output_file):
    """
    Calculates the imperfection at each mesh node, based on the 3D scan, using
    ↪ interpolation.

    Parameters:
    - scan_file: str -> Path to the input point cloud file of the 3D scan.
    - mesh_file: str -> Path to the input mesh node grid of the FE model.
    - output_file: str -> Path to save the interpolated mesh grid.
    """
    # 1. Load scan point cloud
    scan_points = np.loadtxt(scan_file)
    scan_xyz = scan_points[:, :3]

    # 2. Load mesh nodes
    # Mesh file has: index, x, y, z
    mesh_data = []
    with open(mesh_file, "r") as f:
        for line in f:
            parts = line.strip().split(",")
            index = int(parts[0])
            coords = [float(p) for p in parts[1:]]
            mesh_data.append([index] + coords)

    mesh_data = np.array(mesh_data)
    mesh_indices = mesh_data[:,0].astype(int)
    mesh_xyz = mesh_data[:,1:4]

    # 3. Apply manual translation if desired
    # (optional adjustments in case you need fine alignment)
    manual_dx = 0.0
    manual_dy = 0.0
    manual_dz = 0.0

    aligned_scan_xy = scan_xyz[:,:2] + np.array([manual_dx, manual_dy])
    aligned_scan_z = scan_xyz[:,2] + manual_dz

    # 4. Interpolation (Linear)
    mesh_xy = mesh_xyz[:,:2]
    z_interp = griddata(
        points=aligned_scan_xy,
        values=aligned_scan_z,
        xi=mesh_xy,
```

```
        method="linear"
    )

    # 5. Fallback to nearest neighbor ONLY for any NaNs at edges
    nan_mask = np.isnan(z_interp)
    if np.any(nan_mask):
        print(f"Note: {nan_mask.sum()} nodes fell outside convex hull, using nearest
        ↩  neighbor fallback.")
        z_interp[nan_mask] = griddata(
            points=aligned_scan_xy,
            values=aligned_scan_z,
            xi=mesh_xy[nan_mask],
            method="nearest"
        )

    # 6. Compute imperfection relative to original mesh z
    z_mesh = mesh_xyz[:,2]
    z_difference = z_interp - z_mesh
    z_imperfect = z_mesh + z_difference

    # 7. Write output file
    with open(output_file, "w") as f:
        for i, index in enumerate(mesh_indices):
            x = mesh_xyz[i,0]
            y = mesh_xyz[i,1]
            z = z_imperfect[i]
            f.write(f"{index:7d}, {x:12}, {y:12}, {z:12.6f}\n")

    print(f"Imperfect mesh saved to {output_file}")
```

C

Additive Stiffener Details

Appendix C shows a more clear and detailed representation of the WAAM stiffener. This includes the geometry dimension on the left, but also the mesh configuration of the complex WAAM geometry on the right.

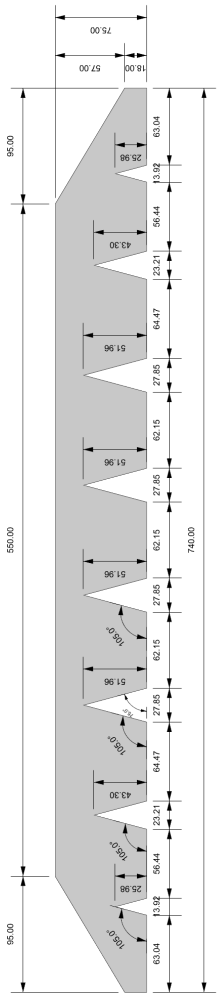

Figure C.1: WAAM stiffener geometry dimensions before printing

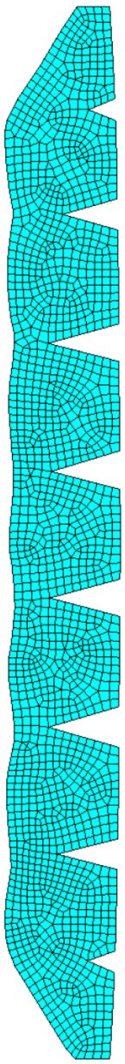

Figure C.2: FE mesh configuration of the WAAM stiffener